Nanoscale

ROYAL SOCIETY OF CHEMISTRY

MINIREVIEW

View Article Online
View Journal | View Issue

Cite this: *Nanoscale*, 2025, **17**, 21423

Phage–nanomaterial platforms for precision antimicrobial therapy: from design to therapeutic application

Manlin Qi[a,b,c] and Andy Tay *[a,c,d]

The rapid increase in multidrug-resistant (MDR) bacteria and biofilm-associated infections has intensified the global need for innovative antimicrobial strategies. Phage therapy offers promising precision against MDR pathogens by utilizing the natural ability of phages to specifically infect and lyse bacteria. However, their clinical application is hampered by challenges such as narrow host range, immune clearance and limited efficacy within biofilms. Nanotechnology has emerged as a powerful complementary approach, offering broad-spectrum antimicrobial properties, tunable physical properties and responsive functionality. Despite these advantages, most nanomaterials lack precise bacterial targeting and may pose biosafety risks. The combination of phages and nanomaterials opens new avenues for synergistic antibacterial therapy. Nanomaterials not only enhance phage stability, delivery and penetration, but also enable multimodal therapy, including photothermal and photodynamic therapy. At the same time, phages endow nanomaterials with highly specific bacterial recognition and lysis activities, improving therapeutic selectivity and reducing microbiota destruction. In this paper, we review the structural features of phages, strategies to construct phage–nanomaterial platforms, the antimicrobial mechanisms of nanomaterials and their applications in different infection models. We also highlight current limitations and future directions. Together, these insights provide a foundation for the rational design of next-generation antimicrobial platforms for precision therapy.

Received 28th May 2025,
Accepted 2nd September 2025

DOI: 10.1039/d5nr02249e

rsc.li/nanoscale

1 Introduction

The increasing number of multidrug-resistant (MDR) bacterial pathogens and the recalcitrance of biofilm-associated infections collectively constitute one of the most daunting challenges in modern medicine and economic burdens. In 2021, an estimated 4.71 million deaths were associated with bacterial antimicrobial resistance (AMR), including 1.14 million directly attributable to it. Without effective intervention, AMR is forecasted to cause up to 8.22 million deaths by 2050.[1] In addition, AMR will exacerbate global economic inequality, and the long-term effects could reshape the global economic landscape, with far-reaching impacts on human capital and healthcare systems.[2] Microbial biofilms *i.e.*, surface-attached communities of cells encased in an extracellular polymeric substance (EPS), account for chronic infections, including chronic wound infection or chronic lung infection in patients with cystic fibrosis.[3] Within these biofilms, bacteria can be up to 1 000-fold more resistant to antibiotic treatment compared to their planktonic counterparts, attributing to impeded drug penetration, metabolic dormancy of persister cells, and enhanced horizontal gene transfer (HGT).[4,5] As the development of new antibiotics continues to stagnate, the need to explore and advance alternative antibacterial strategies has become increasingly urgent.

Phage therapy, once overshadowed by the advent of small-molecule antibiotics, has re-emerged as a precise tool for fighting bacterial infections. Phages are viruses that specifically infect bacteria, and they have several unique advantages to fight against AMR: they self-amplify at the site of infection, exhibit narrow host specificity, allow for the retention of commensal microbiota, and can evolve in concert with their bacterial hosts.[6] Recent phage therapy cases on a compassionate basis have shown successful clearance of MDR *Pseudomonas aeruginosa* (*P. aeruginosa*) and *Acinetobacter baumannii* (*A. baumannii*) in critically ill patients, hence highlighting the clinical

[a]*Institute of Health Innovation & Technology, National University of Singapore, Singapore, 117599, Singapore. E-mail: bietkpa@nus.edu.sg*
[b]*Department of Oral Implantology, Jilin Provincial Key Laboratory of Sciences and Technology for Stomatology Nanoengineering, School and Hospital of Stomatology, Jilin University, Changchun, 130021, China*
[c]*Department of Biomedical Engineering, National University of Singapore, Singapore, 117583, Singapore*
[d]*NUS Tissue Engineering Program, National University of Singapore, Singapore, 117510, Singapore*

potential of phage therapy.[7,8] Nonetheless, the clinical application of phages faces several major challenges, including their narrow host range, rapid immune clearance that contributes to a limited circulation half-life, and the emergence of phage-resistant bacterial strains.[9] Additionally, the dense EPS that characterizes biofilms can sequester phages and restrict their diffusion, reducing infectivity against sessile bacterial populations.[10]

Nanotechnology is another powerful tool for antimicrobial therapy. Various types of nanomaterials, such as metal- and metal oxide-based, carbon-based materials, polymer nanoparticles (NPs), nanozymes and metal–organic framework materials, have been widely used for antimicrobial interventions.[11–17] These nanomaterials can exhibit broad-spectrum and highly effective antibacterial properties by physically disrupting the bacterial membrane structure, chemically inducing oxidative stress, or acting as drug delivery carriers to enhance the stability and penetration of antimicrobial drugs. Nanomaterials also possess tunable particle size, surface structure and responsive functionality, which can improve tissue penetration, targeted delivery and controlled release.[18,19] However, nanomaterials generally lack active recognition of specific bacteria and have limited targeting capabilities, which can easily interfere with the host microbiota.[20] Combining phage and nanotechnology offers a synergistic platform that compensates for their respective limitations.[21] Nanomaterials introduce multimodal antimicrobial strategies, such as photothermal therapy (PTT), photodynamic therapy (PDT), and chemodynamic therapy, which work synergistically with phage-induced bacterial lysis to improve the clearance efficiency of both planktonic and biofilm, while enabling precise bactericidal activity.[22–28]

In this review, we first introduce the classification and structural characteristics of phages and outline the major limitations that currently hinder their therapeutic application. We then focus on the construction strategies used to fabricate phage–nanomaterial platforms, with a systematic

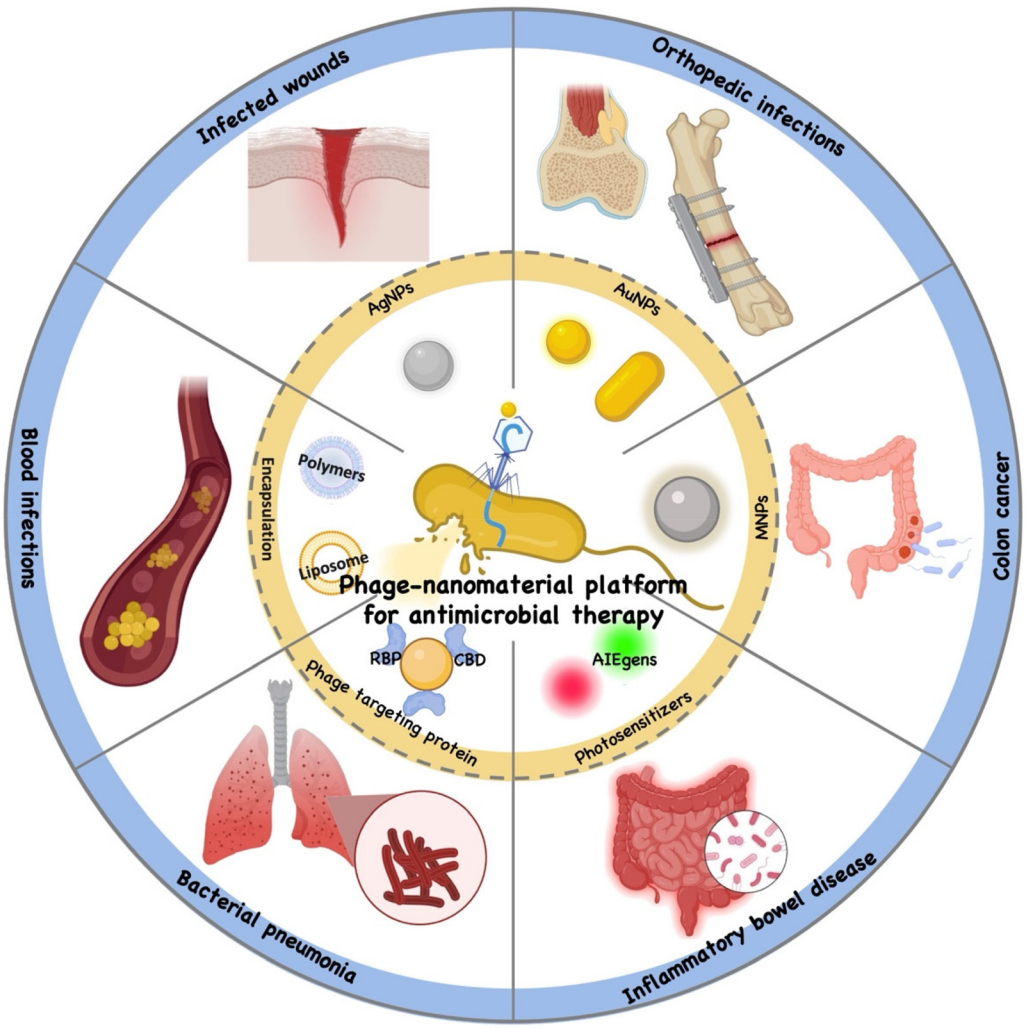

Fig. 1 Schematic diagram of phage–nanomaterial platforms applied in antimicrobial therapy.

summary of the functional groups present on phage and nanomaterial surfaces. We then examine the construction strategies for phage–nanomaterial platforms, including the functional groups on phage and nanomaterial surfaces, the commonly used coupling methods, and the spatial design principles that guide their assembly. We further categorize the antimicrobial mechanisms of widely studied nanomaterials and discuss how these mechanisms integrate synergistically with phages to build multifunctional antibacterial platforms. We also review representative applications of such platforms across various infection models, including wounds, implants, lungs, bloodstream infections, and bacteria-related tumors. Finally, we provide insight into the challenges and future directions for phage–nanomaterial platforms (Fig. 1). Collectively, these advances provide a comprehensive foundation for the continued development of clinically relevant phage–nanomaterial platforms designed to precisely treat bacterial infections.

2. Overview of phages and limitations of phage therapy

Phage therapy has attracted renewed interest in recent decades as a targeted, evolution-compatible approach to combat MDR bacterial infections. As natural predators of bacteria, phages possess a diverse array of mechanisms for host recognition, invasion, replication, and lysis. However, whilst the specificity and self-amplification characteristics of phages offer compelling advantages, their clinical translation remains hindered by several biological and practical constraints. A clear understanding of phage biology, lytic mechanisms, and the inherent limitations of standalone phage therapy is essential for the rational development of improved phage-based interventions, including those involving nanoengineering.

2.1 Classification of phages

Phages can be classified based on their morphology or genome type. Traditionally, morphologically distinct tailed phages were divided into three families: long-tailed (*Siphoviridae*), contractile-tailed (*Myoviridae*), and short-tailed (*Podoviridae*), all of which possess double-stranded DNA (dsDNA) genomes. In addition, filamentous phages (*Inoviridae*, *e.g.*, M13) and icosahedral phages without tails (*Microviridae*) form separate morphological groups. However, in 2022, the International Committee on Taxonomy of Viruses (ICTV) abolished these morphology-based families and reclassified all tailed dsDNA phages under the class *Caudoviricetes*.[29]

By genome type, phages can carry either DNA or RNA genomes, which may be single- or double-stranded. Over 90% of known phages are dsDNA phages. Single-stranded DNA (ssDNA) phages include filamentous types such as M13 and icosahedral members of the Microviridae family. RNA phages are less common and include both double-stranded RNA (dsRNA) phages like φ6 (*Cystoviridae*) and single-stranded RNA (ssRNA) phages such as MS2 (*Leviviridae*).[30]

2.2 Structure of phages

2.2.1 Head (Capsid). The head of a phage is a highly organized protein shell, or capsid, that encases and protects the viral genome. It typically adopts an icosahedral geometry (*e.g.*, the elongated icosahedron of phage T4) or a filamentous form (*e.g.*, M13), depending on the phage family.[31,32] In most icosahedral phages, a portal complex is present at the apex of the head, serving as the gateway through which DNA is packaged into the capsid during assembly and released during infection. To withstand the high internal pressure generated by densely packed DNA, the capsid shell is reinforced through a combination of inter-subunit interactions and accessory decoration proteins such as Hoc and Soc.[33] These outer proteins enhance structural stability under stress conditions such as elevated temperature or extreme pH, and their absence can significantly compromise capsid integrity.[34] In contrast, filamentous phages like M13 do not possess a portal complex or Hoc/Soc-like decoration proteins. Instead, their capsids are composed of thousands of copies of the major coat protein pVIII, which helically assemble around the single-stranded DNA genome to form a flexible, rod-like particle. This structure enables M13 to extrude from the host cell without lysis, contributing to its unique infection cycle and engineering potential.

2.2.2 Tail. Extensive tail structures present in many dsDNA phages are required for host recognition, attachment, and genome transfer. The complexity and architecture of these tails vary per phage species, although they often feature a modular design that is tailored to the efficacy of infection. The T4 phage is a well-studied example with a tail of roughly 925 Å and consisting of six long tail fibers, a hexagonal baseplate, a central tail tube, and a contractile sheath.[35] Long tail fibers promote the first reversible contact with specific bacterial surface receptors such as lipopolysaccharides (LPS), outer membrane proteins, and teichoic acids.[36] Following proper alignment and binding, a sequence of conformational changes occurs as the baseplate and short-tail fibers become more tightly linked to the host cell envelope. When the rigid core is driven through the bacterial membrane, the sheath encircling the tail tube constricts, allowing DNA to be injected into the cytoplasm.[36,37] Damage or alteration to critical tail components such as the baseplate, sheath, or tail fibers can destroy the phage's ability to adhere or inject its genome. This can interfere with receptor identification and sheath contraction. Therefore, for infection and replication to be successful, the tail structure's coordination and integrity are crucial. In contrast, filamentous phages such as M13 lack contractile tails entirely. Instead, they rely on specialized minor coat proteins at one end of the filament (*e.g.*, pIII) to mediate attachment to the host's F pilus and facilitate genome entry without mechanical penetration. This structural simplicity supports persistent, non-lytic infections that distinguish them from the lytic life cycles of many tailed dsDNA phages. Fig. 2 illustrates the basic structure of the T4 and M13 phages.

2.2.3 Phage targeting protein. Receptor Binding Proteins (RBPs) are located at the distal end of the phage tail and play a crucial role in initiating infection. RBPs recognize and bind to

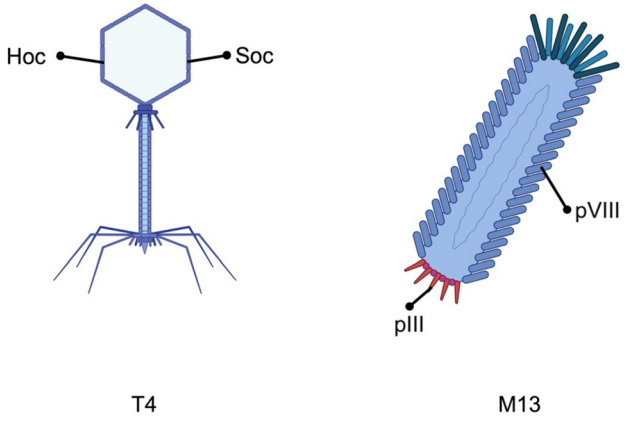

Fig. 2 The structure of two common phages (T4 and M13 phage) in phage nanoengineering.

specific receptor molecules on the bacterial surface, such as LPS, capsules, polysaccharides, or outer membrane proteins, enabling the phage to firmly attach to the target cell and initiate genome injection. RBPs exhibit diverse structural types, commonly including tail fibrin (TFP) and tailspike protein (TSP), and some even possess enzymatic activity that facilitates penetration through host surface barriers.[36,38] In contrast, Cell Wall Binding Domains (CBDs) are frequently found in lysins from phages targeting Gram-positive bacteria. As modular protein components, CBDs mediate precise localization to the bacterial cell wall by specifically and non-covalently binding to structures such as peptidoglycan or teichoic acids.[39] Between the fact that both RBP and CBD have a great deal of specificity and affinity for their bacterial hosts, as well as the natural abundance of host-specific phages, researchers tend to combine them with NPs for targeted antibacterial therapy and bacterial detection.[40–45]

2.3 Phage therapy and its limitation

Phage therapy, which employs lytic phages as antibacterial agents, offers a promising strategy to combat AMR and enable targeted bacterial eradication. Lytic phages specifically infect susceptible bacteria, replicate within them, and ultimately induce bacterial lysis, releasing progeny phages that amplify the therapeutic effect as self-replicating agents.[7] Phages have been investigated for targeted antibacterial therapy, vaccine development, nanodrug delivery, and other biomedical uses due to their great host specificity and intrinsic immunogenicity.[46–49] The clinical effectiveness and translational potential of independent phage therapies are hampered by significant obstacles, despite their distinct biological advantages. To enhance treatment results, these constraints, in particular limited host range, low biofilm penetration, and quick immune clearance, need to be carefully considered and innovatively approached.[24,50–52]

A significant drawback of phages is their highly limited host range, which is usually limited to a single bacterial species or even certain strains. In contrast to broad-spectrum antibiotics, which can affect a variety of bacteria, phages need to be precisely identified and matched to the pathogen. Although this specificity helps to minimize disruption of commensal microbiota, it poses logistical issues in acute clinical settings when prompt treatment decisions are required prior to the completion of precise pathogen typing.[53] Moreover, phage resistance often arises spontaneously due to receptor masking or loss caused by the continuous development of bacterial surface receptors, which are the main phage attachment sites.[54] To address these challenges, researchers have proposed several strategies, including phage cocktails, and phage engineering to expand the effective host range of phages. Phage cocktails typically consist of a selection of several phages assembled based on complementary host ranges, different receptor targets and synergistic bactericidal activity.[55] Although phage–phage interference can occur, especially in complex mixtures, carefully optimized combinations can reduce the likelihood of bacterial escape through resistance mutations, especially when the constituent phages utilize different routes of infection.[56,57] Currently, cocktail therapies are in clinical trials for burn wounds,[58] urinary tract infections,[59] cystic fibrosis,[60] and diabetic foot,[61] and most of these cases are safe, well-tolerated and clinically improved. Phage engineering encompasses targeted genomic and homologous recombination to enhance phage efficacy, safety, and versatility.[62,63] A primary focus is broadening the host range by altering RBPs, while biofilm degradation is achieved through the incorporation of depolymerase or quorum-quenching enzyme genes.[64] Resistance is countered *via* preadapted mutant selection and deletion of lysogeny-related genes to produce fully lytic phages, as demonstrated in pan-drug resistant *K. pneumoniae* and *Mycobacterium abscessus* clinical cases.[65,66] Moreover, engineered phages serve as delivery vehicles for CRISPR–Cas payloads to enhance the potency of the phage, expanding the host range,[67] to edit bacterial antibiotic-resistance,[68] or carry reporter genes for sensitive pathogen detection.[69] Recently, a phase 2 ELIMINATE trial demonstrated that a genetically engineered six-phage cocktail, LBP-EC01, in combination with TMP–SMX, achieved rapid and sustained clearance of *Escherichia coli* (*E. coli*) in patients with uncomplicated UTIs, showing good tolerability and promising therapeutic potential for antibiotic-resistant infections. Further randomized controlled evaluation is ongoing.[70]

Another major limitation is the poor penetrability of bacterial biofilms, which are a predominant mode of bacterial growth in chronic infections. Phage diffusion and access to embedded bacteria are hindered by the physical and chemical barrier provided by the EPS matrix of biofilms.[3,71] The metabolically inactive bacterial subpopulations that develop from biofilms' sharp pH, oxygen, and nutrition gradients are also naturally resistant to phage-mediated lysis, which necessitates active bacterial machinery.[72] Although some studies support the use of phage cocktail therapy against multispecies bacterial biofilms, most of the studies have been confined to animal models, and the therapeutic efficacy of phage therapy for infections on disease-infected biofilms such as chronic wounds or respiratory infections is still limited.[73–77]

Finally, rapid immune clearance and *in vivo* instability are also significant barriers to phage efficacy. Following systemic administration, phages are rapidly recognized and removed by components of the host immune system in 24 h, in particular the mononuclear phagocyte system.[78] In addition, pre-existing antibodies from environmental exposure to natural phages or previous therapeutic doses can neutralize phages, reducing their bioavailability before they reach sites of infection.[79] Inflammatory responses can also be exacerbated by the immunogenicity of phage capsid proteins or by bacterial lysis, releasing endotoxins.[80,81] Systemic phage therapy is made more difficult by these pharmacokinetic and immunological restrictions, which frequently necessitate high-dose or repeated administration as well as novel delivery techniques such as phage encapsulation to increase circulation time and lower immunogenicity.[70,82]

3 Strategies for nanoengineered phages

To address the inherent limitations of conventional phage therapy, recent research has focused on integrating nanotechnology with phage platforms to enhance their therapeutic applicability. This integration aims to compensate for the shortcomings of native phages and to achieve functional diversification through rational material design and structural engineering. This section summarizes current strategies for the construction of nanoengineered phages. First, we introduce the commonly used surface functional groups and coupling chemistries that enable stable conjugation between phages and nanomaterials. We then discuss the spatial organization and design principles of structured phage–nanomaterial assemblies. Finally, we review representative classes of nanomaterials used in antibacterial phage platforms, focusing on their antimicrobial mechanisms, design considerations, and therapeutic performance.

3.1 Surface functional groups on phages and modified coupling agents

Establishing covalent chemical bonds is a key step toward achieving stable conjugation between nanomaterials and phages. A thorough understanding of the functional groups present on the phage surface facilitates the rational design of phage–nanomaterial composites. The capsid of phages is composed of various amino acids that carry a wide range of reactive functional groups, including amine, carboxyl, and phenol groups. The amine group is the most common chemical modification site on phages, as it is present at the N-terminus of all proteins and on lysine side chains. Typical coupling agents include 1-ethyl-3-(3-dimethylaminopropyl)carbodiimide (EDC) and *N*-hydroxysuccinimide (NHS) esters, with materials often functionalized with carboxyl groups. Conversely, carboxyl groups located at protein C-termini or on aspartic and glutamic acid side chains can also be targeted using EDC and NHS esters, where materials are usually modified with amine groups. Phenolic hydroxyls on tyrosine residues can be modified with alkynes *via* diazonium coupling, enabling subsequent conjugation of azide-functionalized ligands through click chemistry.[83] Moreover, some studies converted amine groups on the phage surface into thiols to enable coordinate covalent binding with gold nanoparticles (AuNPs). These moieties serve as multifunctional reactive sites for both conventional bioconjugation and bioorthogonal chemical reactions. Their utilization enables site-specific and stable integration of nanomaterials under physiological conditions, without interfering with native biological processes. Table 1 provides an overview of functional group compatibilities between phages and photosensitizers (PSs) or nanomaterials, along with the corresponding chemical conjugation.

3.2 The spatial location and design principles of nanomaterials and phages

To translate the functional advantages of phage–nanomaterial platforms into practical applications, it is necessary to dissect the properties and design principles of the relevant core nanomaterials. The main role of these nanomaterials is that of antimicrobial agents, which can act synergistically with the antimicrobial activity of phages. There are also nanomaterials with sensing properties that can be used in conjunction with phages to target bacteria. There are also polymer-based nanomaterials that can encapsulate phages to enhance bacterial bactericidal viability and titer. Depending on the relative size, surface charge, and morphology of the components, several types of spatial arrangements have been observed, including head-adsorption, side-adsorption, and full encapsulation (Fig. 3A–H). These interactions are governed by electrostatic attraction, covalent bonding, or van der Waals forces.[22,100–102] However, configurations that interfere with the phage tail, such as direct modification of the tail sheath or baseplate, are generally discouraged. Such arrangements are likely to impair the contraction of tail fibers or hinder DNA injection, ultimately reducing infectivity. Regardless of that form of distribution, it is important to ensure that the phage head and tail are not damaged by NPs during assembly. In addition to the combined application of phage and NPs, some researchers have extracted phage-targeting proteins and modified the surface of the particles, which can also play a role in targeting antimicrobial activity (Fig. 3G). In addition, to avoid destructive external factors such as temperature, pH, and mechanical forces, it is often necessary to encapsulate polymers on the outside of the phage to prevent microenvironmental effects on phage titer and viability (Fig. 3H).[103]

3.3 Representative phage–nanomaterial antibacterial platforms

The integration of phage with antimicrobial nanomaterials forms the basis of a nanoengineered phage platform in which the nanomaterials are used as functional building blocks to enhance the therapeutic efficacy, stability and environmental responsiveness of the phage. These hybridized structures endow the phage with novel physicochemical properties such

Table 1 Representative examples of surface functional groups on phages and modified coupling agents

Original or modified groups on phage surface	Conjugation	PSs or nanomaterials	Ref.
Original groups			
Amine ($-NH_2$)	NHS ester		
	Ce6-NHS	—	84
	EDC/NHS	RB (–COOH)	22
	EDC/NHS	Co_3O_4 (–COOH)	85
	EDC/NHS	MnO_2 (–COOH)	86
	EDC/NHS	MNPs (–COOH)	87
	EDC/NHS; 11-MUA	Au electrode	88
	Sulfo-LC-SPDP	Au electrode	88
Carboxyl (–COOH)	EDC/NHS	NB ($-NH_2$)	89
	EDC/NHS	Fe_3O_4 ($-NH_2$)	90
Thiol (–SH)		DSPE-PEG2000-MAL modified PNP	91
Modified groups			
Thiol (–SH)	SATP	AuNPs/AuNRs	92 and 93
	EDC/NHS; cysteamine	HCOOH-PEG-SH modified AuNPs	94
	EDC/NHS; HCOOH-PEG-SH	Au@AgNR@DTTC	95
	SPDP; TCEP-HCl	AuNPs	96
	SATA; NH_2OH·HCl/EDTA	Au	97
Azide group	Azide-NHS	DBCO-modified irinotecan-loaded DNPs	98
Alkynyl group	prp	Azide-coated MNPs	99

Abbreviations: AgNRs, silver nanorods; AuNRs, gold nanorods; DBCO, azodibenzocyclooctyne; DNPs, dextran nanoparticles; DTTC, 3,3′-diethylthiocarbocyanine iodide; EDC, 1-ethyl-3-(3-dimethylaminopropyl)carbodiimide; MNPs, magnetic nanoparticles; MUA, 11-mercaptoundecanoic acid (11-MUA); NB, Nile blue; NHS, *N*-hydroxysuccinimide; PNP, prodrug nanoparticle; Prp, propargylglyoxy phenylalanine; RB, Rose Bengal; SATA, *N*-succinimidyl *S*-acetylthioacetate; SATP, *N*-succinimidyl-*S*-acetylthiopropionate; SPDP, *N*-succinimidyl 3-(2-pyridyldithio)propionate; Sulfo-LC-SPDP, sulfosuccinimidyl 6-(3′-(2-pyridyldithio)propionamido)hexanoate; TCEP, tris(2-carboxyethyl) phosphine.

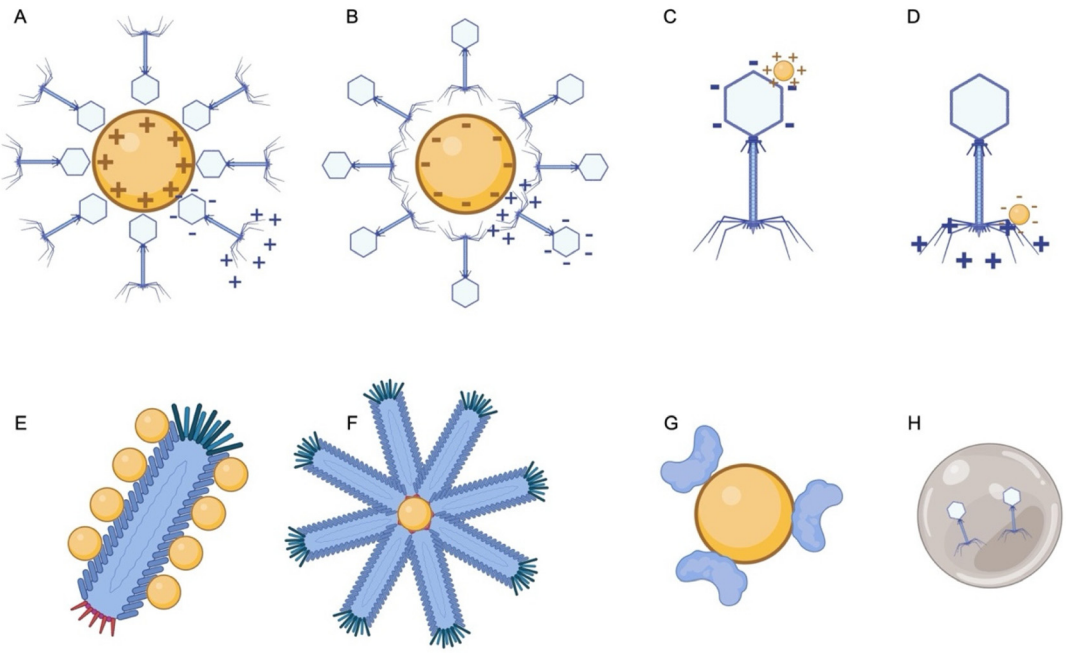

Fig. 3 Possible distribution forms of the combination of phage and nanomaterials. Phages adsorb to large NPs with (A) positive or (B) negative surface charges through electrostatic interactions. Small NPs adsorb onto the phage (C) capsid or (D) tail fibers, *via* electrostatic interactions. (E) NPs adsorb along filamentous phage bodies *via* electrostatic interactions. (F) Self-assembly of filamentous phages around a central NP core *via* covalent conjugation. (G) Surface modification of NPs using phage-derived targeting proteins. (H) Encapsulation of intact phages for environmental protection. (A), (C), and (E) may also involve covalent conjugation depending on surface modifications.

as ion release, photoresponsiveness, magnetic responsiveness, and sensing properties. In this section, the most representative nanomaterials currently incorporated into phage antimicrobial platforms are classified and discussed. These materials include inorganic NPs such as silver (AgNPs) and AuNPs, MNPs, PSs and aggregation-induced emission luminogens

(AIEgens), and organic/polymer carriers for phage protection and sustained release. Each of these materials has unique synergistic or complementary properties when combined with phages, and the rational design of these hybrid materials should consider not only their antimicrobial efficacy, but also their selectivity, biocompatibility and impact on phage infectivity.

3.3.1 Silver nanoparticles. AgNPs exhibit broad-spectrum antimicrobial activity against Gram-positive and Gram-negative bacteria, MDR pathogens, fungi, and viruses, positioning them among the most extensively studied inorganic nanomaterials.[104–106] These properties have supported their incorporation into the US Food and Drug Administration (FDA)-approved clinical formulations and various commercial products such as wound dressings and medical coatings[107] AgNPs exert antimicrobial effects *via* multiple mechanisms, including direct membrane disruption, intracellular metabolic interference, and oxidative damage, often accompanied by sustained release of bioactive Ag^+ ions.[108–111]

AgNPs initiate antibacterial activity by binding to bacterial surfaces, causing structural damage and metabolic disruption. Upon adhesion, AgNPs have been observed to cause significant membrane depolarisation, disrupt membrane potential, increase permeability, and ultimately induce lysis.[112] Direct evidence from transmission electron microscopy (TEM) and atomic force microscopy imaging reveals morphological changes such as membrane wrinkling, detachment, and electron-dense pit formation.[113,114] AgNPs disrupt membrane packing, increase rigidity, reduce fluidity, and promote leakage of intracellular ions, metabolites, and enzymes upon insertion into the lipid bilayer.[115,116] These disturbances lead to metabolic collapse and cell death by impairing bacterial respiration, nutrient transport, and energy homeostasis.[117]

Concurrently, AgNPs induce strong oxidative stress, primarily by generating reactive oxygen species (ROS). Catalytic reactions on AgNP surfaces with dissolved oxygen, and Fenton-like reactions driven by released Ag^+, generate ROS.[118,119] Oxidative damage occurs when ROS levels exceed bacterial antioxidant defenses. In response, bacteria upregulate thiol-based antioxidants and oxidative defense enzymes such as alkyl hydroperoxide reductase (AhpC).[120] However, severe oxidative imbalance may trigger apoptosis-like responses, accelerating bacterial clearance.

Another antimicrobial mechanism of AgNPs is the sustained release of Ag^+, which contributes independently and synergistically to bacterial killing. Ag^+ has a strong affinity for electron-donating groups such as thiols, phosphates, imidazoles, and carboxylates.[121] This allows irreversible binding to critical biomolecules. Interaction with thiol groups in membrane proteins and intracellular enzymes induces conformational changes and inactivates key processes such as respiration, ATP synthesis, and DNA replication. Furthermore, Ag^+ also interacts with nucleic acids, resulting DNA denaturation, strand breakage, and transcriptional arrest.[122] It also disrupts proton-coupled energy metabolism and potassium ion gradients, further impairing bacterial viability. The continuous release of Ag^+ ensures durable antimicrobial effects, combining oxidative stress generation, biochemical interference, and physical membrane disruption.

Despite their broad-spectrum mechanisms, AgNPs pose risks related to resistance and limited application specificity. Some bacteria can activate adaptive responses such as efflux pump upregulation, secretion of extracellular polymers chelating Ag^+, and enhanced antioxidant defences.[123,124] Although slower and less efficient than antibiotic resistance, these strategies still pose challenges under prolonged or sub-lethal AgNP exposure.[125] In addition, the lack of intrinsic selectivity of AgNPs for pathogenic bacteria limits their therapeutic specificity. This is particularly problematic in complex environments such as the oral cavity, intestines, and infected wounds, where preserving beneficial microbes and avoiding host damage are essential. Higher doses of AgNPs are often required when used alone, raising concerns over cytotoxicity and thrombosis.[126,127] Therefore, combining phages with AgNPs offers a promising strategy to enhance antimicrobial efficacy while addressing resistance and specificity limitations.

Currently, AgNPs represent the most extensively studied component in phage-NP antibacterial system development. Combination strategies range from simple mixing to incorporating AgNPs into phage particles before antibacterial testing. For instance, a combined application of AgNPs and phage ϕ44AHJD demonstrated potent efficacy against pre-formed *S. aureus* Rumba biofilms.[128] Unlike monotherapies that showed limited effect, the combination reduced biofilm biomass by 75% in first hour and nearly 95% after 18 hours. Abdelsattar *et al.* reported a similar synergistic effect using AgNPs in combination with phage ZCSE2 against MDR *Salmonella enterica*.[129] Although phage monotherapy initially inhibited bacterial growth, resistant populations emerged within 6 hours, leading to regrowth. In contrast, the combined treatment prevented resistance and maintained antibacterial activity over time. The minimum inhibitory concentration (MIC) and minimum bactericidal concentration (MBC) of AgNPs were both determined to be 23 μg mL^{-1} against MDR *Salmonella enterica* at 10^7 Colony Forming Unit (CFU) mL^{-1}. Notably, even a sublethal AgNP dose at 0.4× MIC, when combined with phage at a multiplicity of infection (MOI) of 0.1, retained significant inhibitory capacity, underscoring the synergistic effect.

To enhance the stability and targeted delivery of AgNPs, Szymczak *et al.* engineered a T7 phage (T7Ag-XII) displaying an AgNP-binding peptide on the gp10B capsid protein, enabling direct and stable conjugation.[130] This self-assembling phage–nanomaterial hybrid demonstrated sustained antibiofilm activity against *E. coli*, reducing biofilm biomass by about 50% at both 24 and 48 hours. This sustained efficacy contrasts with the limited durability of single-agent therapies, which often succumb to bacterial regrowth over extended incubation periods. Importantly, the engineered platform retained strong antibacterial activity at AgNP concentrations as low as 0.002 mg mL^{-1}, reducing potential cytotoxicity while preserving efficacy. Additionally, variations in AgNP synthesis

methods and phage strain selection influence the antibacterial outcomes of these combination strategies. Table 2 summarizes the experimental conditions and outcomes of various phage–AgNP hybrid systems. While most studies have demonstrated their antibiofilm activity, the enhancement of biofilm penetration remains largely indirect. By increasing bacterial membrane permeability and inducing localized ROS generation, AgNPs may reduce the EPS production, thereby facilitating phage access in a supportive rather than active manner.[131] However, they lack active or targeted biofilm-penetrating capabilities.

To elucidate the mechanisms underpinning their synergistic antibacterial efficacy, Zhang *et al.* investigated how phage-AgNP platforms exert coordinated antimicrobial effects.[132] AgNPs enhance phage infectivity by increasing outer membrane permeability and inducing oxidative stress, which facilitates more efficient phage entry. Conversely, specific phage recognition promotes AgNP adhesion to bacterial surfaces, intensifying oxidative stress and membrane disruption, and enhancing antibacterial activity. However, the authors cautioned that such interactions might accelerate the dissemination of resistance genes within bacterial populations, potentially worsening AMR. In addition, Gilcrease *et al.* identified potential antagonistic interactions between AgNPs and phages.[133] They reported that uncoated AgNPs inhibit phage infectivity by binding electrostatically to positively charged residues at the C-terminus of capsid proteins. In contrast, polyvinylpyrrolidone-coated AgNPs interact differently with phages, either enhancing or diminishing infectivity depending on the phage type. Notably, such inhibitory effects were observed only in specific phage types, suggesting a structurally selective mechanism. Moreover, AgNP impact on phage viability depends on nanoparticle concentration, Ag^{+} release, and exposure time. These findings support the rational design of phage–AgNP platforms.

3.3.2 Gold nanoparticles. AuNPs have garnered considerable interest in biomedical research owing to their distinctive physicochemical properties. The term "AuNPs" encompasses a broad range of nanostructures, including spherical AuNPs, gold nanorods (AuNRs), gold nanostars (AuNSs), core–shell particles, and flower-like or triangular sheet-like morphologies.[138] Key features of AuNPs include surface plasmon resonance (SPR), particularly localized SPR (LSPR), a high surface-area-to-volume ratio, excellent biocompatibility, and low cytotoxicity.[138] These attributes render AuNPs highly suitable for diverse applications, including drug delivery, imaging, therapy, and biosensing.[139] In recent years, increasing attention has been directed towards the application of AuNPs in antibacterial therapy. Their antibacterial mechanisms are multifaceted, encompassing physical disruption of bacterial membranes, interference with metabolic pathways, and PTT-induced bacterial eradication.[140–143] Additionally, AuNPs have demonstrated exceptional performance in rapid pathogen diagnostics, particularly through platforms such as LSPR sensing, colorimetric assays, electrochemical detection, and surface-enhanced Raman spectroscopy (SERS).[144–147]

Table 2 Phage–AgNP conjugate for antibacterial therapy

AgNP synthesis source	AgNP size/ morphology	Phage type	Conjugation strategy	AgNP concentration phage MOI	Bacteria species	Antibacterial efficacy	Infection model	Ref.
Allium sativum extract	7.1 ± 0.9 nm (spherical)	ϕ44AHJD phage	Simple mixing	AgNPs: 1 mM 1×10^{8} PFU mL^{-1}	*S. aureus* Rumba	95% biomass reduction at 18 h	*In vitro* (biofilm)	128
Propolis	2–41 nm (oval)	ZCSE2 phage	Co-incubation	AgNPs: 10 μg mL^{-1}; MOI 0.1	MDR *S. enterica*	Inhibit growth after 930 min	*In vitro* (planktonic)	129
Commercial AgNPs	10 nm	T7 wild-type, engineered T7Ag-XII phage	Co-incubation	AgNPs: 0.02 mg mL^{-1}; 1×10^{10} PFU mL^{-1}	*E. coli*	50% biomass reduction at 24 h and 48 h	*In vitro* (biofilm)	130
Commercial AgNPs	<100 nm	T7 wild-type, engineered T7Ag-XII phage	AgNPs-binding peptide Co-incubation	AgNPs: 0.01 mg mL^{-1}; 1×10^{9} PFU mL^{-1}	*E. coli*	67% biomass reduction	*In vitro* (biofilm)	134
O. basilicum L. or *H. sabdariffa* L. extracts	10–15 nm, 5–10 nm (spherical)	ZCSE6 phage	Co-incubation	AgNPs: 3 μg mL^{-1}, 10^{6} PFU mL^{-1}, MOI 1	*S. enterica*	99.9%	*In vitro* (planktonic)	135
Commercial AgNPs	N/A	Podoviridae (LMP3) phage	Co-incubation	AgNPs: 10 μg mL^{-1}; Phage MOI 0.1/1/10	*L. monocytogenes* (MDR strain)	Completely inhibitory effect for 24 h	*In vitro* (planktonic)	136
Silver nitrate/NaOH	26 nm (spherical)	M13 phage	Co-incubation	AgNPs: 86.4 μg mL^{-1} —	*B. subtilis* *E. coli* *P. aeruginosa* *S. aureus*	100% killing rate	*In vitro* (planktonic)	137

Abbreviations: *B. subtilis*, *Bacillus subtilis*; *E. coli*; *Escherichia coli*; *H. sabdariffa* L., *Hibiscus sabdariffa* L.; *L. monocytogenes*, *Listeria monocytogenes*; LMP, *L. monocytogenes phage*; *O. basilicum* L., *Ocimum basilicum* L.; *P. aeruginosa*, *Pseudomonas aeruginosa*; *S. aureus*, *Staphylococcus aureus*; *S. enterica*, *Salmonella enterica*.

AuNPs can interact with bacterial surfaces *via* electrostatic attraction, resulting in their accumulation on the bacterial membrane.[148] This interaction induces structural disruption, including increased membrane permeability and the formation of pores or fissures, as visualized through TEM.[140] These structural alterations may lead to electrolyte leakage, dissipation of the proton gradient, and ultimately, bacterial cell death. AuNPs may also interfere with peptidoglycan biosynthesis by targeting key enzymes, such as transpeptidases, or by compromising the structural integrity of lipopolysaccharides, thereby impairing cell wall synthesis and stability.[149] However, contrasting this mechanism, Lee *et al.* proposed that the antibacterial action of AuNPs does not compromise membrane integrity.[142] Instead, they suggested that AuNPs induce a calcium ion influx, triggered by membrane potential depolarization, which subsequently leads to bacterial apoptosis, DNA damage, cell filamentation, and caspase-like protein activation.

Once internalized by bacteria, AuNPs can selectively interact with key biomolecules, thereby significantly disrupting bacterial physiological processes. Their surfaces are rich in reactive functional groups, enabling coordination with thiol (–SH) or amino ($-NH_2$) groups in proteins, which inhibits enzymatic activity.[150,151] This effect is particularly pronounced in key metabolic enzymes, such as those involved in the respiratory chain.[152] This leads to impaired energy production and disrupted nucleic acid metabolism. Smaller-sized AuNPs exhibit greater surface curvature and area, which enhance their noncovalent interactions with enzymes, such as electrostatic and hydrophobic forces.[153] These interactions may disrupt the enzyme active site, thereby markedly inhibiting its catalytic activity. Additionally, AuNPs can intercalate into double-stranded DNA, obstructing replication and transcription, and thereby suppressing bacterial protein synthesis and proliferation.[154] AuNPs have also been reported to inhibit ATP synthase, thereby substantially reducing ATP production and further depleting bacterial energy reserves.[141,155]

The LSPR effect of AuNPs imparts to them excellent photothermal conversion capabilities.[156] Upon irradiation, AuNPs rapidly convert light into localized heat, sharply increasing the temperature of the surrounding microenvironment. This rapid thermal surge disrupts bacterial membrane lipids and alters protein conformations, resulting in increased membrane permeability, ion leakage, metabolic imbalance, and eventual cell lysis.[157,158] However, such localized high temperatures may also inflict collateral tissue damage. Moreover, PTT may trigger bacterial heat stress responses, potentially leading to thermotolerance and reduced therapeutic efficacy.[159] Consequently, PTT is often combined with other modalities to enhance antibacterial efficacy while minimizing adverse effects.[160]

Recent advances in phage–AuNP platforms have primarily exploited the photothermal bactericidal and sensing properties of AuNPs. Among these, two plasmonic bactericidal nanoplatforms based on M13 phage morphological polymorphs (Au/i-form and Au/s-form) have been designed for the targeted photothermal ablation of F^+ *E. coli* (Fig. 4A).[161] The pIII minor coat protein confers specific recognition of F-pili-expressing *E. coli*, while the pVIII major coat protein displays gold-binding peptides to facilitate efficient AuNP nucleation. Under 532 nm laser irradiation, photothermal assays showed that the Au/i-form reduced bacterial viability to 79% ± 4% after 20 minutes at 300 mW cm^{-2}, while the Au/s-form achieved stronger bactericidal activity, reducing viability to 36% ± 5%, outperforming gold colloid controls. The superior efficacy of Au/s-form was attributed to its closer interaction with bacterial membranes (Fig. 4B). This study illustrates the synergistic antibacterial potential of genetically programmable phage scaffolds combined with plasmonic photothermal effects. In another approach, biomimetic nanostructures termed phage nanosomes (ΦNSAu), mimicking liposomes and based on M13 phage components, were developed by Yadav *et al.* and further functionalized with AuNPs and the antimicrobial chemotherapeutic mitoxantrone to generate a multimodal nanoplatform (ΦNSAuM) (Fig. 4C).[162] In antibacterial assays, treatment of *E. coli* with ΦNSAuM followed by 690 nm laser irradiation for 10 minutes led to a significant reduction in colony-forming units compared with untreated and gold colloid controls (Fig. 4D). In antifungal studies, *Candida albicans* stained with Calcofluor White exhibited markedly suppressed spore formation and hyphal growth after ΦNSAuM treatment (Fig. 4E), confirming that its antimicrobial efficacy stemmed from photothermally induced structural disruption.

Building upon these phage–AuNP conjugates, Zn^{2+} was incorporated to construct a hybrid platform termed Phanorod-Zn.[93] This system leveraged the combined bactericidal effects of photothermal heating and Zn^{2+} release to accelerate wound healing (Fig. 4F). *In vitro* experiments showed bactericidal rates of 97.5% ± 1.5% against planktonic *P. aeruginosa* and 86.5% ± 3.6% against biofilms, with Zn^{2+} contributing by disrupting bacterial membrane integrity to enhance photothermal killing (Fig. 4G). *In vivo*, the treatment group exhibited bacterial loads over tenfold lower than those treated with antibiotics, and wounds were completely healed within seven days —a threefold acceleration. This photothermal-responsive design not only improved antimicrobial efficacy but also promoted tissue regeneration *via* controlled release of therapeutic metal ions. Furthermore, recent work by Zeng *et al.* identified deoxyinosine triphosphate (dITP) as an antiviral immune signal in bacteria, with Zn^{2+} playing a crucial role in regulating this pathway.[163] In the Kongming antiphage defense system, phage DNA and KomA cooperate with host nucleoside diphosphate kinase (NDK) to convert dAMP into dITP, which acts as a signaling molecule (Fig. 4H). dITP then activates the KomBC complex, resulting in NAD^+ depletion and programmed cell death. Zn^{2+} significantly enhances the NAD^+-cleaving activity of KomBC, suggesting a potential synergistic mechanism between phage-derived signaling and Zn^{2+}-mediated toxicity (Fig. 4I and J).

Interestingly, some researchers have taken an opposite approach by employing AuNRs to inactivate phages rather than target bacteria, with the goal of preventing phage-induced fail-

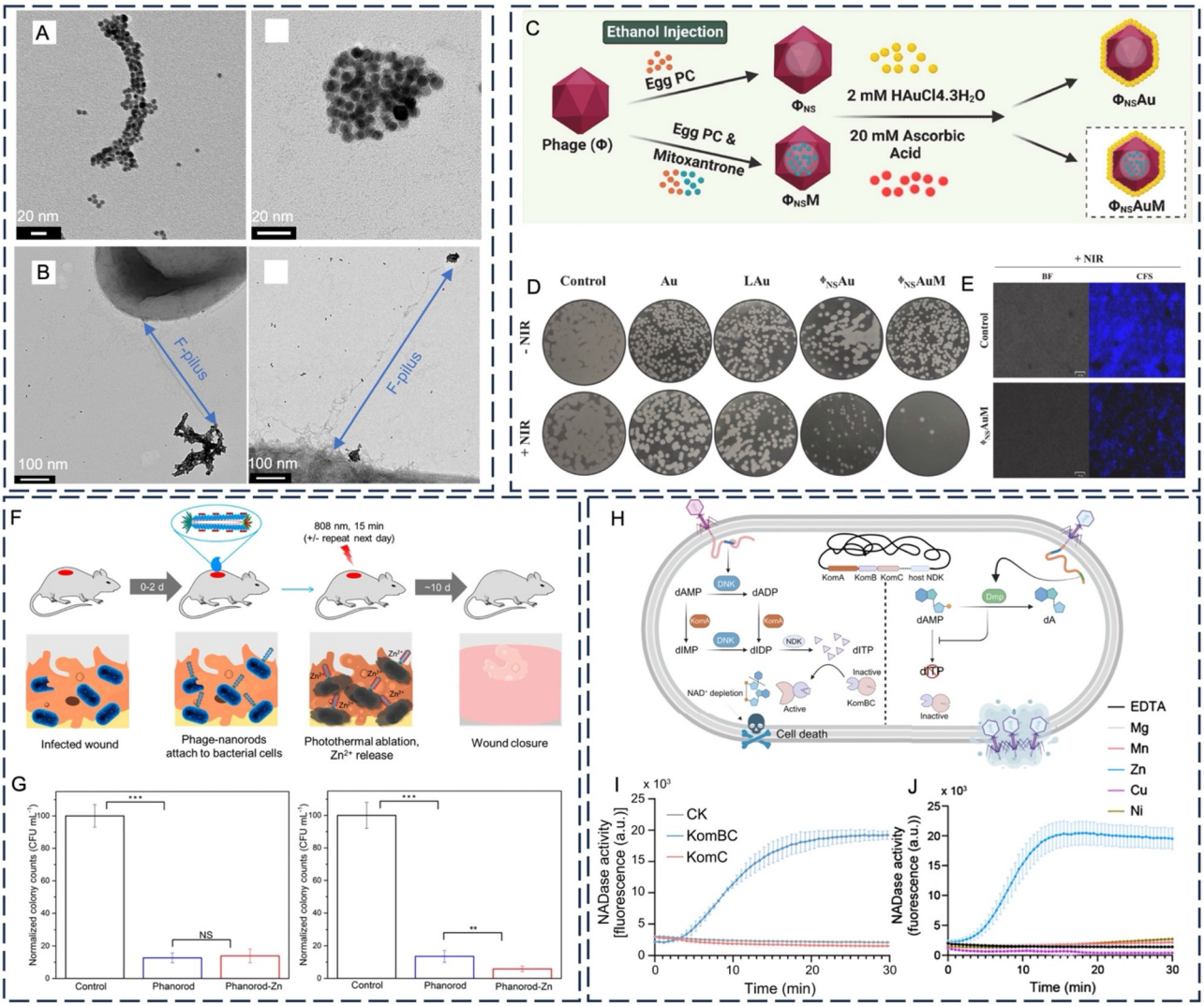

Fig. 4 Phage-AuNP conjugates for antimicrobial therapy and detection. (A) Gold-binding M13 phage displayed in i-form and s-form, each decorated with 5 nm AuNPs. A few unbound NPs are also visible. (B) i-form and s-form phage/AuNP complexes bound to F-pili through pIII-mediated interactions. (C) Diagram illustrating the synthesis process and potential applications of gold-coated MTX-phage nanosomes (ΦNSAuM). (D) CFU formation assay showing the PTT effect mediated by ΦNSAuM on *E. coli* growth. (E) Calcofluor white staining of biofilm (scale bar: 100 μm). (F) Schematic illustration of treatment of a *P. aeruginosa*-infected wound by phanorod-Zn. (G) Antibacterial activity of phanorod-Zn with planktonic *P. aeruginosa in vitro* and the bacterial viability within the treated *P. aeruginosa* biofilm *in vitro*. (H) The mechanism of T5 5′-deoxynucleotidase inhibits Kongming by degrading dAMP. (I) NADase activity assay of purified KomC and KomBC proteins (0.8 μM) using ε-NAD as the substrate. The control (CK) contained no enzyme. (J) NADase activity of KomBC in the presence of EDTA or indicated divalent metal ions. (A) and (B) Reproduced with permission from ref. 161, Copyright 2019, American Chemical Society. (C) to (E) Reproduced with permission from ref. 162, Copyright 2023, Elsevier B.V. (F) and (G) Reproduced with permission from ref. 93, Copyright 2022, American Chemical Society. (H) to (J) Reproduced with permission from ref. 163 Copyright 2025. AAAS.

ures in industrial fermentation.[164] Negatively charged AuNRs, coated with a mixture of 11-mercapto-1-undecanesulfonic acid and hydrophobic 1-octanethiol, initially bound to the necks and heads of phages *via* electrostatic interactions. Subsequent irreversible local distortions, driven by hydrophobic effects, resulted in phage inactivation. These NPs reduced phage titers by 2 and 5 logs following 6 and 24 hours of incubation at 50 °C, respectively. This outcome may be attributed to the low initial concentration of phages (200 pfu mL^{-1}) and the relatively high concentration of AuNRs (100 μg mL^{-1}). Additionally, the negatively charged NPs may be electrostatically repelled by bacterial surfaces, thereby limiting their antibacterial efficacy.

3.3.3 Magnetic nanoparticles. MNPs, particularly iron oxide variants such as Fe_3O_4, have attracted considerable attention for antibacterial and antibiofilm applications owing to their excellent biocompatibility, tunable magnetic responsiveness, and capacity for surface functionalization.[165] MNPs can be driven magnetically,[166] electromagnetically,[167] and ultrasonically,[168] exhibiting multiple antibacterial mechanisms.

Firstly, their positively charged surfaces can interact electrostatically with bacterial membranes or catalyze Fenton-like reactions to generate ROS, thereby compromising membrane integrity, inducing oxidative stress, and ultimately leading to bacterial cell death.[169–171] Some researchers also propose that ROS generation by MNPs may result from electron release by zero-valent Fe and proton accumulation associated with Fe vacancies, with elevated e^-/h^+ concentrations and separation efficiency significantly enhancing ROS production.[167] Secondly, when exposed to an alternating magnetic field, MNPs can produce localized heat (magnetic hyperthermia), enabling thermal bactericidal effects independent of antibiotics.[171] More importantly, MNPs can be actuated by rotating or oscillating magnetic fields to produce microscale shear forces and mechanical agitation, effectively disrupting bacterial EPS, reducing surface adhesion, and promoting the disassembly and clearance of mature biofilms.[172,173]

Building upon their multifaceted antibacterial mechanisms, the integration of MNPs with phages into composite antimicrobial platforms has emerged as a promising strategy for addressing biofilm-associated infections. When conjugated with phages, MNPs can generate mechanical forces or magnetic hyperthermia under an external magnetic field, allowing them to penetrate deeply into the biofilm matrix. Phages may act as "passive riders" during this process, gaining access to embedded bacteria that are otherwise inaccessible. This magnetically guided motion, combined with the infectivity of phages, contributes to enhanced biofilm penetration and synergistic bacterial elimination through physical disruption and targeted lysis. Meanwhile, phages serve as biological targeting agents that selectively infect bacteria. For example, a study developed a ternary antibacterial formulation comprising T4 phages, surface-functionalized Fe_3O_4 nanoparticles, and the antimicrobial peptide Nisin (Fe_3O_4 Phage T4 plus Nisin).[174] This composite exhibited potent antibiofilm activity against MDR *P. aeruginosa* strains. Achieving a biofilm inhibition rate of approximately 85%, the composite significantly outperformed its individual components—Nisin (*c.* 20%), T4 phage (*c.* 50%), and Fe_3O_4 (*c.* 30%). Similarly, its biofilm removal efficiency reached approximately 75%, markedly surpassing the removal rates of 20%, 40%, and 15% achieved by the respective monotherapies. Mechanistically, Fe_3O_4 nanoparticles enhanced phage penetration into biofilms and facilitated bacterial cell wall disruption *via* magnetically induced mechanical forces, whilst Nisin broadened the antibacterial spectrum to cover both Gram-positive and Gram-negative species. To address the challenge of antimicrobial instability under complex environmental conditions, the composite maintained robust antibacterial activity across a pH range of 5 to 8, with peak efficacy observed at pH 7.

In another study, a phage-loaded magnetic NP cluster (PNC)-based platform was developed to enhance biofilm eradication.[175] The researchers systematically assessed magnetic colloidal nanoparticle clusters (CNCs) of three diameters (150 nm, 250 nm, and 500 nm), covalently conjugated with polyvalent phages PEB1 (54 nm) and PEB2 (86 nm). Results demonstrated that smaller PNCs with higher surface amino group densities exhibited significantly improved biofilm penetration and clearance. Compared to larger clusters, the smaller PNCs achieved more uniform phage distribution at the biofilm base, promoting enhanced lateral diffusion and basal layer disruption. Consequently, they removed up to 98.3% of dual-species biofilms and over 90% of multi-species biofilms. In contrast, larger PNCs, which primarily relied on vertical penetration, showed reduced efficacy, with removal efficiencies of 80.2 ± 3.4% and 67.6 ± 3.8% for dual- and multi-species biofilms, respectively. A semi-empirical computational model further supported that PNC size influences the dominant phage propagation pathway: smaller clusters favored lateral spread and basal clearance, whereas larger ones induced vertical disruption but were less effective in complete biofilm elimination.

Despite the approval of AgNPs, AuNPs, MNPs, and some of their associated products by the FDA, there is still a need for a comprehensive understanding of their toxicity. NPs exposure differentially triggers apoptosis, autophagy necrosis, and cell cycle arrest in a dose-dependent manner.[176–178] Table 3 summarizes representative toxicity studies in animal models and human cell lines that report multi-organ lesions and mortality. Toxicity is influenced by exposure duration and accumulation, dose, particle size, surface ligands and other physicochemical properties.[179,180] Optimization of these parameters may mitigate NP associated toxicity.

3.3.4 Photosensitizers or aggregation-induced emission luminogens. PSs are light-activated molecules widely applied in antimicrobial PDT (aPDT), where they generate ROS upon irradiation to inactivate pathogens. Among them, aggregation-induced emission luminogens (AIEgens) have gained increasing interest due to their strong fluorescence and efficient ROS generation in aggregated states, overcoming the aggregation-caused quenching (ACQ) typical of conventional PSs. AIE-active PSs also exhibit tunable photophysical properties, high photostability, and potential for real-time imaging. However, when used alone, both traditional PSs and AIEgens may suffer from limited microbial specificity, poor penetration into dense biofilms, and rapid systemic clearance, leading to suboptimal antimicrobial efficacy and possible collateral damage to healthy tissues due to non-specific ROS activity.

To address these limitations, combining PSs or AIEgens with phages has emerged as a promising strategy. Phages offer natural bacterial specificity, enabling precise delivery of PSs to infection sites and enhancing localized ROS-mediated killing while minimizing off-target effects. In one study, Nile Blue (NB), a red-light-excited PS, was structurally modified and conjugated to an *A. baumannii*-specific phage to form an antimicrobial platform (APNB).[89] The introduction of sulphur atoms increased the trilinear state quantum yield, allowing efficient ROS generation under 660 nm light. The ROS output of APNB was comparable to that of free NB, and it achieved 89.3% eradication of MDR *A. baumannii* biofilms at 0.5 μM, inhibiting biofilm formation in a concentration-dependent manner. Furthermore, engineering phages can broaden the antibacterial spectrum of such platforms. For instance, Rose

Table 3 Representative toxicity studies of NPs in animal models and human cells

NPs	Lesions or deaths	Animal model	Dose	Ref.
AgNPs				
Animal	Weight loss	Mice	5 mg per kg bw per day	181
	Alterations in liver enzymes	Mice	1 mg per kg bw per day	182
	Blood value changes	Rats	300 mg per kg bw per day	183
	Cardiac enlargement	Turkeys	110 mg per kg bw per day	184
	Kidney injury	Rats	1 or 2 mg per kg bw per day	185
	Neurotoxicity	Rats	2.25 mg per kg bw per day	186
	Immunotoxicity	Mice	0.25 mg per kg bw per day	182
	Death	Rats	280 mg per kg bw per day	187
		Rabbits	800 mg per kg bw per day	
Human	Cell toxicity	T lymphocytes	>50 ppm	188
		Monocytes	30 ppm	
		Human mesenchymal stem cells	50 ppm	
	Cell toxicity	Human mesenchymal stem cells	10 μg mL^{-1}	189
	DNA damage	Human lung cells	10 μg mL^{-1}	190
AuNPs				
Animal	Blood value changes	Mice	1 mg per kg bw dose	191
	Cardiac enlargement	Mice	400 μg per kg bw per day	192
	Liver injury	Rats	21.7 μg per kg bw per day	193
	Death	Mice	8 mg per kg bw per week	194
Human	Cell death and neurotoxity	Embryonic stem cells and neural derivatives	0.1 μg mL^{-1}	195
	Destroy integrity of the Epithelial monolayers	Intestinal epithelial cells	10 μg mL^{-1}	196
	Cell apoptosis	Kidney cells	20 μM	197
MNPs				
Animal	Cardiac tissue necrosis	Mice	LD_{50} 147.58–181.37 mg per kg bw	198
	Liver swollen	Mice	5 mg Fe per kg	199
	Lung and liver tissue inflammation	Rats	20 mg kg^{-1} dose	200
	Circulating erythrocyte apoptosis	Rats	12 mg kg^{-1}	201
Human	Cell toxicity	Human fibroblasts	0.05 mg mL^{-1}	202
	Cell toxicity	Human macrophages	0.1 mg mL^{-1}	203
	Cell toxicity	BeWo b30 placental cell	15 and 75 mg cm^{-2}	204
	Cell toxicity	Human heart, brain, and Kidney cells	36 mM	205

Bengal (RB) was conjugated to engineered M13 phages targeting Gram-negative bacteria.[22] This modification resulted in a red-shifted, broadened absorption peak at 560 nm, enhancing light absorption and ROS generation. Compared to free RB, the conjugated formulation exhibited a fourfold increase in singlet oxygen ($^1O_2$) yield and an eightfold increase in peroxide production, attributed to greater surface binding density and optimized energy transfer. To overcome the instability and poor solubility of organic near-infrared (NIR) dyes, phage-based nanocarriers have been explored as delivery vehicles. In the case of IR780 and ICG, for example, phage nanosome loading resulted in a significant enhancement of UV-vis absorption and a better photothermal conversion efficiency than that of conventional liposomes.[206] Under NIR light, the temperature of IR780-loaded phage nanocarriers increased to 46 °C within one minute, while the ICG-loaded version reached 58 °C in two minutes. Pushing the boundaries of targeted aPDT, a smart eye drop was developed by co-assembling the type I PS ACR-DMT with a phage specific to MDR *P. aeruginosa* (Fig. 5A).[207] Under white light, ACR-DMT generated hydroxyl radicals ($^{\bullet}OH$) *via* a type I pathway, with ROS production maintained even under hypoxic conditions. The combined platform enabled targeted and image-guided therapy, achieving 98.68% eradication of MDR-PA biofilm biomass and an 88.68% reduction in biofilm thickness, thereby effectively suppressing ocular surface infections.

Recent advances have explored the integration of AIEgens with phages to improve the targeting specificity and photodynamic efficacy of aPDT, while also enabling theranostic applications. One such example is a phage (PAP) conjugated with the AIE-active PSs TVP-S, forming TVP-PAP *via* amino–carboxyl coupling, with approximately 8200 TVP-S molecules bound per phage (Fig. 5B).[208] The modified phage retained its ability to bind lipopolysaccharides on Gram-negative bacterial surfaces, resulting in specific accumulation of AIEgens and strong local fluorescence. This platform allowed rapid staining of *P. aeruginos*a within 30 minutes and enabled real-time imaging of Gram-negative infections. This team also designed a DNA-functionalized MS2 phage that was conjugated with the AIEgen TVP-T to create a fluorescent bioconjugate for diabetic wound therapy (Fig. 5C).[209] TVP-T exhibited a fluorescence quantum yield of 35.4% in chloroform and achieved a $^1O_2$ quantum yield of 72.5% under white light. *In vitro*, the bioconjugate selectively eradicated *E. coli*, reducing bacterial viability to 0.52% after 30 minutes of irradiation. Additionally, a phage-based antimicrobial platform engineered with an AIE-active PS (TBTCP-PMB) was developed (Fig. 5D).[210] TBTCP-PMB demonstrated typical AIE characteristics, with fluorescence intensity increasing 172-fold in 98% toluene compared to pure DMSO, and a quantum yield of 17.9%. Its ROS generation efficiency was 6.27-fold higher than that of RB, with a markedly enhanced $^1O_2$ yield.

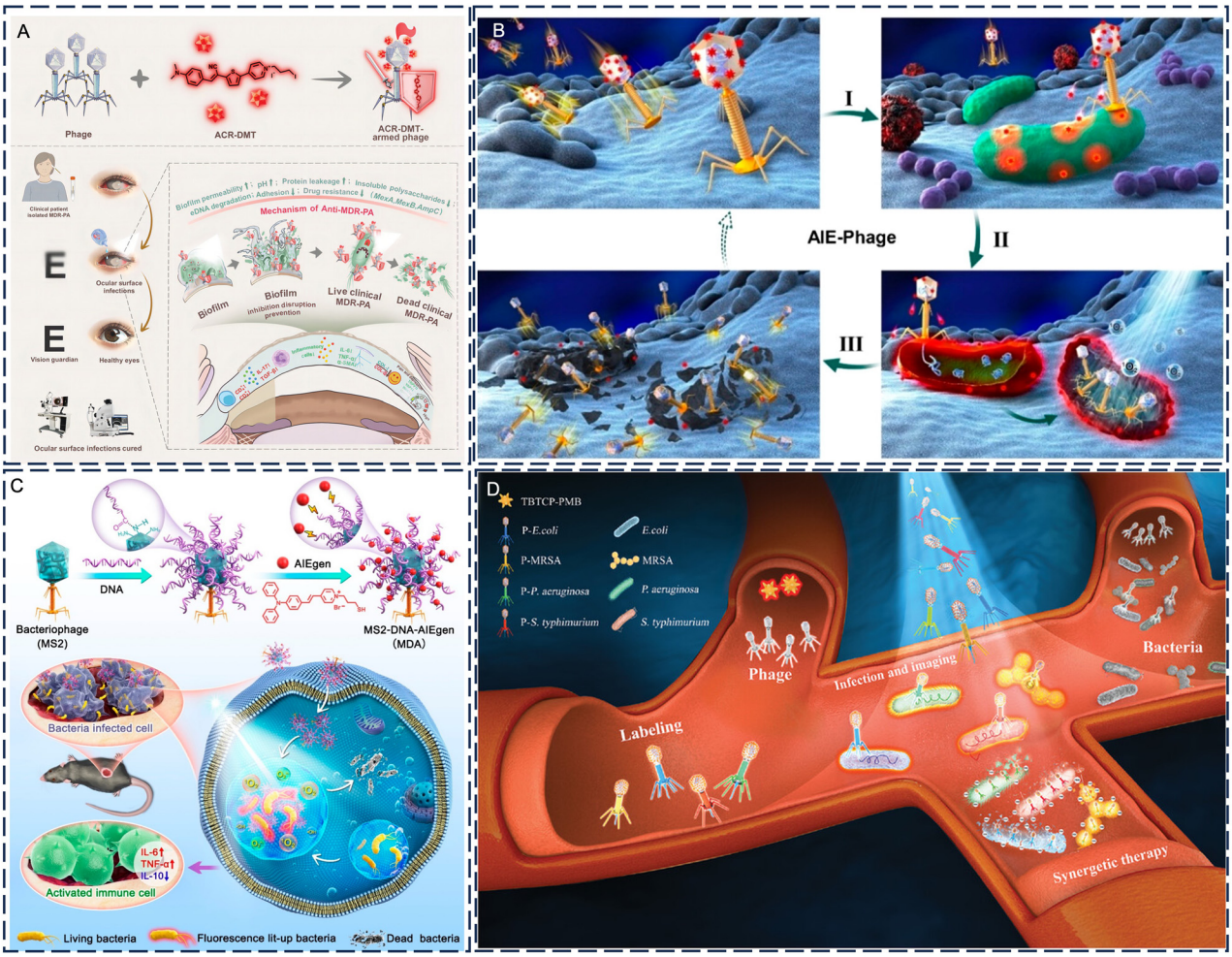

Fig. 5 Schematic illustrations of AIEgens-armed phage for anti-infection therapy. (A) ACR-DMT-armed phage eyedrops for treating clinical MDR-PA BK. (B) Phage-guided targeting, discriminative imaging, and synergistic killing of bacteria by TVP-S equipping phage bioconjugates. (C) The delicately designed MS2-DNA-AIEgen nanobioconjugate for specific targeting and synergistic elimination of intracellular bacteria. (D) The cocktail therapy of sepsis with TBTCP-PMB engineered phage. (A) Reproduced with permission from ref. 207, Copyright 2024, Wiley-VCH GmbH. (B) Reproduced with permission from ref. 208, Copyright 2020, American Chemical Society. (C) Reproduced with permission from ref. 209, Copyright 2024, American Chemical Society. (D) Reproduced with permission from ref. 210, Copyright 2022, Wiley-VCH GmbH.

Collectively, these studies demonstrate that phage-AIEgen platforms combine three key functions: precise bacterial targeting, potent photodynamic killing, and real-time fluorescence imaging, making them promising candidates for next-generation antimicrobial nanotherapeutics.

3.3.5 Phage ligand-nanoparticles. An RBP-based targeted antimicrobial nanodelivery system has been developed to target *S. aureus* infections. Rifampicin (RIF)-loaded poly(lactic-*co*-glycollic acid) NP (RIF-NP) were fabricated using a nanoprecipitation technique.[43] Phage K-derived recombinant RBP (rGp144) was further modified to the surface of the NPs by coupling to construct the targeted nanosystem (RIF144-NP). Notably, both RIF-NP and RIF144-NP exhibited the ability to reduce the MIC to $\leq$0.005 μg mL^{-1} for all *S. aureus* strains, including *S. aureus*, MRSA, oxacillin-susceptible *S. aureus*, and methicillin-oxacillin-resistant *S. aureus*. In contrast, little to no antibacterial activity was observed against *E. coli*, confirming the specificity of the RBP-based targeting system. This targeted platform offers a precise and efficient approach to combatting drug-resistant bacterial infections by enhancing local drug concentrations at the infection site. Similarly, Zhao *et al.* developed two phage ligand-functionalized nanoplatforms for the targeted treatment of drug-resistant infections (Fig. 6A and B).[42] The RIF-loaded lipid-coated urchin-like porous silica NPs conjugated with RBP (RIF@LUN@RBP) achieved a 90% survival rate in carbapenem-resistant *Klebsiella pneumoniae*-infected mice, representing a 16-fold improvement in therapeutic efficacy compared to the free drug. Likewise, CBD-modified UPSN (UPSN@CBD) conferred 100% survival in MRSA-infected mice with a 27-fold enhancement. Across various drug-resistant models, these systems consistently reduced effective doses by 16–32 times whilst maintaining therapeutic outcomes. These platforms not only significantly reduced the required antibiotic dosage but also demonstrated excellent bacterial

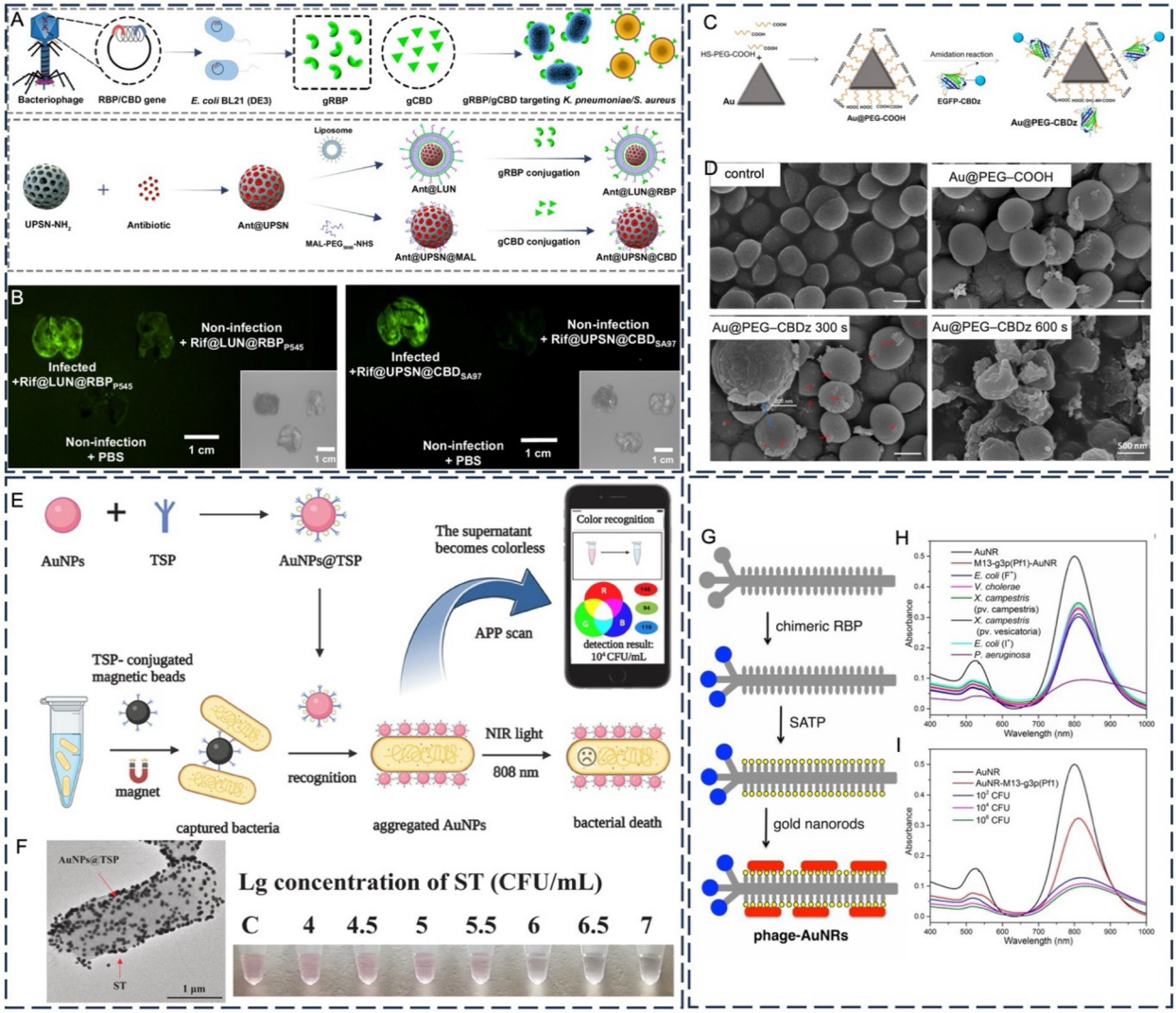

Fig. 6 Phage ligand-NPs conjugates for antimicrobial therapy and detection. (A) Schematic illustrations of the construction of two targeting devices: lipid-coated UPSNs (LUN) bearing RBPs (LUN@RBP) and CBDs modified UPSNs (UPSN@CBD). (B) Time-gated fluorescence imaging confirmed infection-targeted lung accumulation of phage-derived RBP/CBD-modified nanocarriers in CRKP- and MRSA-induced pneumonia models. (C) Synthesis flow chart of Au@PEG–CBDz. (D) SEM images of MRSA strains after irradiation with different conditions. (E) Schematic diagram of *S. typhimurium* detection and photothermal inactivation. (F) TEM image of ST after incubation with AuNPs@TSP. (G) Schematic of M13 phage-AuNR conjugates prepared by *N*-succinimidyl-*S*-acetylthiopropionate (SATP)-mediated thiol–gold coupling and RBP display for specific bacterial targeting. (H) Specific detection of *P. aeruginosa* following incubation with various bacterial species (10^6 CFU). (I) Sensitivity assessment of *P. aeruginosa* detection within a complex bacterial mixture consisting of *E. coli* (F^+), *V. cholerae*, *X. campestris* pv. *vesicatoria*, *X. campestris* pv. *campestris*, and *E. coli* (I^+). (A) and (B) Reproduced with permission from ref. 42, Copyright 2024, Springer Nature. (C) and (D) Reproduced with permission from ref. 44, Copyright 2023, American Chemical Society. (E) and (F) Reproduced with permission from ref. 211, Copyright 2024, Elsevier B. V. (G) to (I) Reproduced with permission from ref. 92, Copyright 2020, *PNAS*.

specificity, biocompatibility, and consistent therapeutic performance upon repeated administration, highlighting their strong potential in addressing antibiotic resistance.

Researchers have also combined phage-targeting proteins with gold nanomaterials to construct precise platforms for PTT and bacterial detection. Yan *et al.* synthesized photothermal gold nanosheets functionalized with the CBD protein from MRSA phage Z (Au@PEG-CBDz) (Fig. 6C).[44] Au@PEG-CBDz binds specifically to the MRSA cell wall *via* CBDz, exhibiting significantly higher bactericidal efficiency than non-targeted Au nanosheets (Au@PEG-COOH) under NIR irradiation. Upon 420 seconds of irradiation, the Log_{10} CFU in the Au@PEG-COOH group decreased from 4.00 to 2.98, whereas a more pronounced reduction to 0.85 was observed in the Au@PEG-CBDz group. SEM imaging revealed membrane wrinkling and rupture in the targeted group, whereas the non-targeted group exhibited no significant structural damage (Fig. 6D). An integrated detection-treatment biosensor based on phage tail spike protein (TSP)-modified AuNPs (AuNPs@TSP) was developed for the rapid detection and

photothermal sterilization of S*almonella typhimurium* (Fig. 6E).[211] The TSP from phage P22 was electrostatically adsorbed onto AuNPs and combined with magnetic beads (TSP-MBs) to enable bacterial separation and enrichment. After six minutes of 808 nm NIR irradiation at 2 W cm^{-2}, the local temperature rose from 27.9 °C to 66.2 °C, achieving complete (100%) bactericidal efficiency. During detection, specific binding of TSP to bacterial LPS induces AuNP aggregation, changing the solution color from violet-red to colorless. The RGB value is analyzed using a smartphone app, with a detection limit of 2.53×10^3 CFU mL^{-1}. The entire assay is completed within 50 minutes (Fig. 6F). Additionally, Peng *et al.* proposed a colorimetric biosensing strategy using RBP-modified phage–AuNP conjugates, enabling rapid, sensitive, and low-cost detection of multiple bacterial pathogens.[212] In this method, thiolated phages bind to AuNRs, which aggregate on the phage surface and serve as signal amplifiers, producing a visible color change due to LSPR property alterations. This strategy facilitated rapid and specific detection of two *E. coli* strains, *P. aeruginosa*, *Vibrio cholerae*, and two strains of *Xanthomonas campestris*, with a detection limit of approximately 100 CFU. They further achieved precise control of species-selective bacterial ablation and phage therapy activation by engineering phage platforms functionalized with AuNRs and RBP modifications for targeted recognition (Fig. 6G).[92] Host specificity evaluation of six phage–AuNR constructs revealed LSPR shifts exclusively in the presence of their respective target strains. After 10 minutes of NIR irradiation, each conjugate effectively eradicated its target bacterial host, whilst non-target strains remained unaffected. For F^+ *E. coli*, CFU levels dropped to undetectable within 10 minutes, whereas F^- *E. coli* exhibited no significant change, confirming selective targeting (Fig. 6H and I). Moreover, the platform enabled effective photothermal ablation of *P. aeruginosa* biofilms formed on mammalian epithelial cells, achieving approximately 98% bacterial eradication with minimal host cell damage. To facilitate a comparative understanding, Table 4 outlines representative examples of phage–nanomaterial conjugates and their respective efficacy against bacteria.

3.3.6 Nanocarrier-based encapsulation and delivery systems for phage. Phages are highly susceptible to environmental influences, and their structural integrity is easily com-

Table 4 Representative phage–nanomaterial platforms and their antimicrobial performance

Platform type	Phage type	Target pathogens	Antimicrobial efficacy	Combined therapy	Toxicity	Ref.
AuNPs						
Au/i-form Au/s-form	M13 phages	F^+ *E. coli*	79% ± 4% bacteria 36% ± 5% bacteria	PTT	Not reported	161
ΦNSAuM	Phage nanosome	*E. coli C600*	Reduced CFUs in agar	PTT	100 μg mL^{-1} with minimal/no toxicity	162
Phanorod-Zn	M13 phages	*P. aeruginosa*	97.5% (planktonic) 86.5% (biofilm)	PTT/Zn^{2+}	No toxicity	93
MNPs						
Fe_3O_4 Phage T4 + Nisin complex	T4 phages	MDR *P. aeruginosa*	~85% biofilm inhibition	Magnetic therapy/Nisin	Not reported	174
PNCs	*Podoviridae* phages	*E. coli* & *P. aeruginosa*	98.3 ± 1.4% dual species biofilm	Magnetic therapy	Not reported	175
		E. coli, *P. aeruginosa*, *B. subtilis*, *S. oneidensis*	92.2 ± 3.1% multi-species biofilm			
PSs						
APNB	—	MDR	89.3% biofilm eradication	PACT	0.5 μM exceeds 83%	89
		A. baumannii	70% death	PDT	Not reported	22
RB-engineered M13 phage	Engineered M13 phages	*A. baumannii*				
AIEgens						
ACR-DMT	/	MDR *P. aeruginosa*	98.68% biofilm biomass 88.68% biofilm thickness	PDT	25 μm 83%	207
TVP-PAP	Lambda phage	*P. aeruginosa*	99.5% bacteria eradication	PDI	8.45×10^{10} PFU mL^{-1} 83%	208
MS2-DNA-TVP-T	MS2 phage	*E. coli*	99.48% bacteria eradication	PDI	2.4×10^{10} PFU mL^{-1} 90%	209
TBTCP-PMB	Corresponding phage	*E. coli* *P. aeruginosa* *S. typhimurium* MRSA	No bacterial CFU	PDT	2 μm 80%	210

Abbreviations. *A. baumannii*, Acinetobacter *baumannii*; ACR-DMT, type I PS with a phage; APNB, *A. baumannii*-specific phage with Nile Blue; *B. subtilis*, *Bacillus subtilis*; CFU, Colony Forming Unit; *E. coli*, *Escherichia coli*; MNPs, magnetic nanoparticles; MRSA, methicillin-resistant *Staphylococcus aureus*; *P. aeruginosa*, *Pseudomonas aeruginosa*; PACT, photodynamic antibacterial chemotherapy; PDI, photodynamic inactivation; PDT, photodynamic therapy; PNCs, phage-loaded magnetic NP cluster; PTT, photothermal therapy; RB, Rose Bengal; TBTCP-PMB, a phage conjugated with an AIE-active PS; TVP-PAP, a phage conjugated with AIE-active PSs; *S. typhimurium*, *Salmonella typhimurium*; ΦNSAuM, M13 phage nanosome functionalized with AuNPs.

promised upon release from host bacterial cells. This leads to denaturation or degradation of the protein capsid and ultimately results in reduced or complete loss of infectivity. To address this limitation, researchers have developed several approaches, such as PEGylated phage and encapsulation. PEGylated proteins have been shown to retain their native structure and biological activity, typically exhibiting better stability and reduced immunogenicity.[213] Phage PEGylation is achieved by binding PEG to amino acid residues of phages protein. Kim *et al.* reported for the first time that PEGylation can increase the survival rate of infectious phages by delaying immune response, and indicated that this method can improve the efficacy of phage therapy.[214] They used monomethoxy PEG (molecular weight ~5000 Da) to bind to arginine and lysine residues of Felix-O1 (infects *Salmonella*) and A511 (infects *Listeria*) phages, phages were PEGylated at a 1 : 50 ratio. PEGylation significantly enhanced phage stability in circulation and serum. For A511, PEGylation increased infective particles from 0.016% to 20.9% at 6 hours post-injection, with >3-log improvement. PEGylated Felix-O1 also showed slower clearance, retaining 0.7% at 6 hours *versus* 0.03% for the wild type. In pre-immune serum, A511-PEG remained fully viable for 4 hours, while unmodified A511 dropped to 63.3%. In contrast, PEGylated Felix-O1 showed limited protection, with only 5.8% infectivity at 4 hours, similar to native Felix-O1 (2.7%). In both naive and immunized mice, PEGylated phages elicited significantly lower levels of pro-inflammatory cytokines (IFN-γ and IL-6), suggesting attenuated T-helper 1-type immune responses. More and more encapsulation strategies using organic and polymeric carriers to enhance phage stability, prolong persistence, and improve therapeutic efficacy. One such approach involves a pH-responsive polymer nanocoating (Eudragit L100-55, ~20 nm thick) applied directly onto phage-infected bacteria to retain phages intracellularly, referred to as "In-phages" (Fig. 7A).[103] In-phages showed higher resistance in different media environments and at different temperatures. In contrast, phage without the nanocoating (Ex-phages) showed a significant decrease in phage titre over time. In addition to superior viability, in-phages showed significantly higher efficiency in binding and killing host bacteria and eradicating bacterial biofilms compared to ex-phages. At an MOI of 0.1, the binding percentage of In-phages was 1.25 times higher than that of Ex-phages. The difference further increased to ~3.00-fold when the MOI was reduced to 0.01 or 0.001. Cryo-electron microscopy and proteomic analyses indicated that the superior viability of In-phages was due to the maintenance of the structural integrity of their tails. *In vivo*, orally delivered In-phages were more bioavailable under neutral pH conditions and led to improved outcomes in mice with enteritis and arthritis compared to uncoated counterparts. Beyond pH-responsive systems, various biocompatible polymers have also been explored for phage encapsulation. For instance, chitosan NPs encapsulating phage HK6 enhanced thermal and pH stability and improved bactericidal activity against *Enterobacter Cloacae* (Fig. 7B).[215] In addition, studies have shown that poly (lactic-*co*-glycolic acid) (PLGA) encapsulated phages retain their immunogenic properties in addition to stability (Fig. 7C).[216] To further broaden antibacterial coverage and

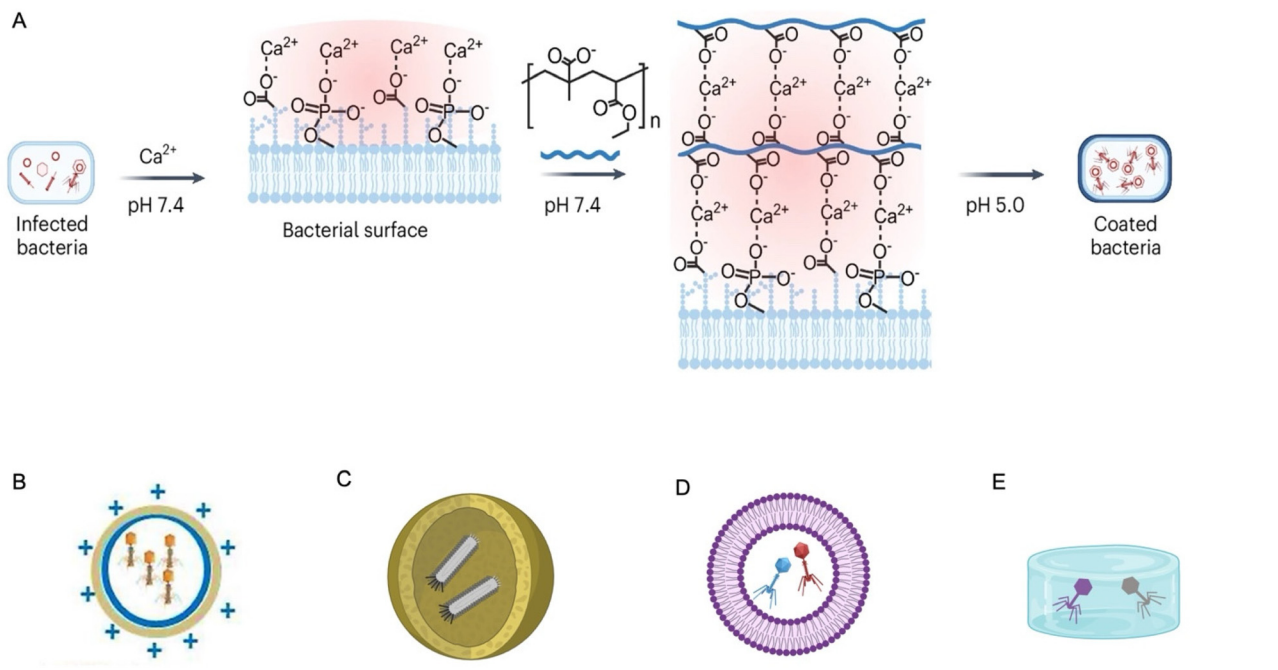

Fig. 7 Organic/polymeric carriers encapsulating phages. (A) Eudragit L100-55 polymer crosslinked *via* Ca^{2+} bridges at pH 7.4 and store at pH 5.5. (B) Cationic chitosan NPs. (C) PLGA microparticles. (D) Liposome and (E) physically or chemically cross-linked phage hydrogels. (A) Reproduced with permission from ref. 103, Copyright 2025, Springer Nature. (B) Reproduced with permission from ref. 215, Copyright 2025, Springer Nature.

delay resistance development, phage cocktails, which combinations of multiple phages, have also been encapsulated in nanocarriers. In one study, two lytic *S. aureus*-specific phages (MR-5 and MR-10) were used either individually, in combination as a phage cocktail, or encapsulated within liposomes (Fig. 7D).[217] Whilst the free phage cocktail significantly reduced bacterial burden and enhanced wound healing compared to monophage therapy, liposome-encapsulated phages further improved phage persistence at the wound site, resulting in a 2-log increase in local phage titers. This enhanced retention correlated with faster infection clearance and improved wound contraction. These findings highlight liposomal delivery as a promising strategy to overcome the limitations of rapid phage clearance *in situ* and to potentiate phage therapy against antibiotic-resistant infections. Hydrogels represent another promising class of organic carriers for localized phage delivery, and their construction methods, advantages and antimicrobial mechanisms, and antimicrobial applications are reviewed in detail by Bai *et al.* and will not be repeated here (Fig. 7E).[218] Notably, the stiffness of phage-loaded hydrogels plays a pivotal role in modulating their antibacterial activity.[219] For both T4 and φX174 phages, the antimicrobial effect against *E. coli* adhered to the hydrogel surface follows a bell-shaped trend with increasing hydrogel stiffness, peaking at approximately 50–100 kPa. At low stiffness, enhanced polycation mobility leads to phage-polymer interactions that mask capsid receptors and impair host recognition. Conversely, high stiffness restricts polymer chain mobility, limiting bacterial membrane disruption and making cells less susceptible to phage infection. Notably, φX174-loaded hydrogels exhibit consistently higher antibacterial efficiency (~70–80%) across the stiffness range, attributed to their shorter replication cycle and stronger intrinsic lytic activity. These findings highlight the critical interplay between hydrogel mechanics, polycation dynamics, and phage infectivity in designing optimized antimicrobial biomaterials. Given that conventional antibacterial implant strategies may cause systemic toxicity, adverse immune effects, manufacturing defects, and bacterial resistance, immunomodulatory coatings offer an alternative means to harness the host's innate defenses for early infection control. A representative example is the chitosan-based bioactive coating ChitoAntibac, designed to address implant-associated infections without relying on conventional antibiotics.[220] This coating can be tailored to exert two complementary actions: immune stimulation and phage-mediated bacterial clearance. By incorporating macrophage migration inhibitory factor, ChitoAntibac actively reprograms local macrophages from a quiescent M0 state to a pro-inflammatory M1 phenotype, thereby enhancing phagocytic capacity and the secretion of bactericidal cytokines. This targeted activation aims to accelerate early bacterial clearance and prevent biofilm establishment in the critical *peri*-implant period. In parallel, the coating can be loaded with Staphylococcal phage K, which provides highly specific lysis of *S. aureus* including drug-resistant strains. The dual-action design achieved >99.99% bacterial eradication within 8 h in preclinical models, while maintaining biocompatibility with neural and bone cells. This dual functionality of timely immune mediation and bacteria elimination highlights the potential of the coating for clinical application in controlling early-stage implant-associated infections which typically emerge within the first 24 hours post-surgery. Fig. 7 summarizes the representative organic or polymeric carriers used for phage delivery.

4. Antimicrobial therapeutic applications of phage–nanomaterial platforms

The practical use of phage–nanomaterial platforms to fight clinically relevant infections has drawn more attention, building on the design concepts and material methods covered in the previous section. These nanoengineered platforms allowed for broaden bacterial targeting, enhancing biofilm penetration, and improving stability in a variety of pathogenic settings. The convergence of phage biology and nanotechnology has thus opened new therapeutic avenues beyond conventional phage therapy. This section reviewed representative applications of phage-nanoplatforms in major infectious disease models, including infected wounds, implant-associated infections, bloodstream infections, pneumonia and bacteria-associated tumors. For each indication, we highlight the design, functional performance and therapeutic outcomes of phage–nanomaterial platforms.

4.1 Infected wounds

Infected wounds persist as a significant global health concern, often resulting in protracted healing, increased hospitalization, and the potential for systemic complications, including sepsis. The increasing prevalence of MDR bacteria has led to a significant challenge to the efficacy of conventional antibiotic treatments, underscoring the urgent need for the development of novel antimicrobial methodologies. During wound healing, phage therapy can specifically eliminate bacteria whilst minimizing disruption to the host microbiota. However, the dense extracellular matrix and hypoxic microenvironment in infected wounds often restrict phage penetration and therapeutic efficacy. To address these challenges, recent studies have focused on integrating phage therapy with advanced nanomaterials to develop multifunctional antibacterial platforms for treating infected wounds. Among these strategies, ROS-generating approaches, such as photodynamic, chemodynamic, or photocatalytic phage–nanomaterial hybrids, have attracted particular attention for their potent bactericidal activity and immune-modulatory potential. In addition to the promotion of bacterial eradication, some phage–nanomaterial platforms have been designed to modulate the wound microenvironment by scavenging excessive ROS, neutralizing bacterial enzymes or toxins, and alleviating inflammatory stimuli, which promote tissue regeneration. Furthermore, the development of hydro-

gel-based platforms as sustained-release carriers for phages has been investigated, with the potential benefits including localized delivery, enhanced retention at the wound site, and protection of phage bioactivity.

Among the ROS-mediated antibacterial tactics, the combination of phages with ROS-generating nanomaterials has drawn interest due to its potential for synergy, combining targeted bacterial lysis with physical disruption. Quantum dots (QDs) are one of the most promising nanomaterials that have been investigated in this regard. QDs, a class of semiconductor nanocrystals, have emerged as effective PSs for photocatalytic therapy (PCT) due to their strong light-harvesting capability, tunable emission, and high quantum yields. In a representative study, Wang *et al.* developed an innovative QD@Phage hybrid nanoplatform that integrates the bacterium-specific targeting ability of phages with the photocatalytic properties of Cd-based QDs (Fig. 8A).[221] Through avidin–biotin coupling, the QDs were effectively anchored onto the surface of phages engineered to specifically recognize green fluorescent protein-labelled *P. aeruginosa* (GFP–*P. aeruginosa*). The TEM results showed that after co-culturing for 30 minutes, most QD@Phage had targeted and aggregated onto host cells and could lyse bacteria after incubating for 90 minutes (Fig. 8B). By applying PA-PCT to bacteria, QD@Phage has achieved powerful *in vitro* antibacterial elimination for both planktonic (over 99.9%) and biofilm (over 99.24%) (Fig. 8C–E). However, due to the limitation of visible light's short tissue penetration depth, QD@Phage may be challenged in treating deep bacterial infections.

With biological, biochemical, and physical elements, the wound microenvironment is extremely complex. A key factor in

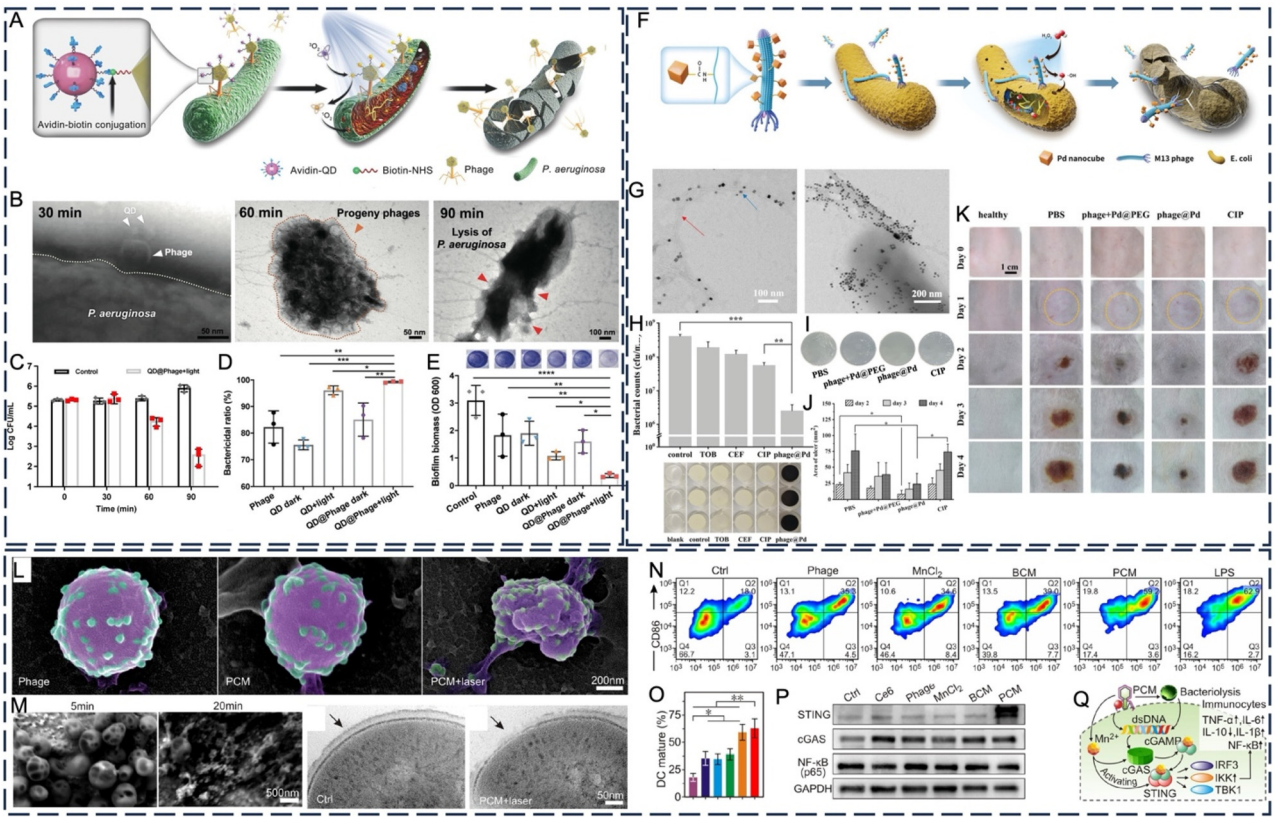

Fig. 8 Phage-NPs for infected wound treatment. (A) Phage-assisted photocatalytic treatment against GFP-*P. aeruginosa* is shown schematically. (B) TEM pictures showing the PA-PCT processes of QD@Phage: bacterial lysis, host bacterial binding, and release of progeny phages. (C) Using the time-killing assay, the CFU counts of planktonic GFP-*P. aeruginosa* treated with QD@Phage (10^6 PFU mL^{-1}) and untreated was measured every 30 minutes for 90 minutes. (D) After 24 hours of incubation, the biofilm bactericidal ratio of phage, QD, and QD@Phage under various circumstances. (E) Quantification of biofilm biomass using crystal violet staining following different treatments. (F) Diagrammatic representation of phage@Pd's structure and antibacterial activity. (G) TEM images of Phage@Pd and phage@Pd with *E. coli*. (H) The antibacterial properties of antibiotics and phage@Pd in mature *E. coli* biofilm and digital pictures of the biofilm of *E. coli* following various treatments. (I) Typical images of bacterial colonies in mice's diseased skin. (J) The skin's purulent region at various intervals. (K) Typical macroabscess photos taken at various intervals. (L) The distribution of phages on bacterial surfaces was shown by magnified SEM images (pseudocolor; bacterial: purple; phage: green). (M) High-resolution TEM pictures demonstrated the NIR irradiation-induced cell wall and membrane and surface alterations of *S. aureus* treated with PCM and NIR irradiation for varying durations were shown. (N) Flow cytometry analysis of costimulator molecule expression in BMDC treated with PCM. (O) Quantitative assessment of BMDC maturation of $CD80^+$ and $CD86^+$. (P) WB detection of STING expression, cGAS, and NF-κB (p65). (Q) A potential immunological process that speeds up wound healing following PCM use. (A) to (E) Reproduced with permission from ref. 221, Copyright 2022, Wiley-VCH GmbH. (F) to (K) Reproduced with permission from ref. 223, Copyright 2023, Wiley-VCH GmbH. (L) to (Q) Reproduced with permission from ref. 24, Copyright 2023, American Chemical Society.

hastening the healing process of wounds is the precise manipulation of this local microenvironment.[222] Researchers created a phage-palladium (Pd) NP (phage@Pd) in response to the high levels of H_2O_2 and the acidic environment in infected wounds (Fig. 8F and G).[223] This platform used Pd's peroxidase-like activity in conjunction with phage targeting to create a "chemical-biological" dual attack strategy. In *in vitro* experiments, the platform achieved a 99.4% biofilm degradation rate against *E. coli*, compared to other tested antibiotics, including tobramycin, ceftazidime, and ciprofloxacin, which only killed 50.0–90.0% of the bacteria (Fig. 8H). In the diabetic foot ulcer model, the germicidal efficacy of the phage@Pd group reached 96.7%. In contrast, the antibacterial efficiency of the phage + Pd@PEG group was 59.4%, and that of the CIP group was 47.4% (Fig. 8I). Visual inspection and quantification of ulcerated areas revealed that a single-dose treatment could not completely cure skin infections in a short time. However, compared with the subsequent inflammation and suppuration in other groups, the phage@Pd treatment led to a much more significant reduction in lesions, indicating its potential in effectively controlling skin infections and minimizing tissue damage (Fig. 8J and K). Building upon similar infection-site characteristics such as elevated hydrogen peroxide and glutathione levels, Wang *et al.* developed phage-Ce6-manganese dioxide nanocomplexes (PCMs), where MnO_2 degraded and excretes Mn^{2+} under acidic conditions, triggering a Fenton reaction that generates $^{\bullet}OH$ and Ce6-mediated PDT.[24] Magnified SEM images showed dense phage accumulation within intact *S. aureus*, partially extruding from the surface and resembling a sesame ball morphology (Fig. 8L). PCM-PDT treatment induced significant disruption of the bacterial cell wall and membrane, with multiple pore-like lesions and partial absence of peptidoglycan (Fig. 8M and N). Flow cytometry demonstrated that PCMs significantly promoted the maturation of bone marrow-derived dendritic cells (Fig. 8O). Western blot analysis further demonstrated that neither phage nor Mn^{2+} alone could upregulate STING expression, whereas PCM markedly enhanced STING expression by synergistically activating the cGAS–STING pathway, highlighting the importance of component synergy in its immune activation (Fig. 8P and Q). However, excessive generation of ROS during bacterial elimination may lead to oxidative damage in host tissues and exacerbate inflammatory responses. To address this issue, Wang *et al.* designed a polyvalent phage PA3 conjugated with ruthenium dioxide nanozyme (PA3@RuO_2), which integrates bacterial targeting and lysis with ROS scavenging capabilities.[224] The RuO_2 nanozyme effectively degraded superoxide anions (O_2^-) and H_2O_2, thereby protecting host cells and increasing the survival rate of HUVECs from 30% to 108.59%. This phage-based strategy efficiently eradicated *P. aeruginosa* biofilms, achieving a bacterial killing rate of over 99.99%, significantly outperforming conventional antibiotics. In a diabetic wound model, PA3@RuO_2 treatment reduced the bacterial load by three orders of magnitude, decreased IL-6 levels by 60%, and promoted collagen deposition to 72.74% by day 15, approaching levels observed in healthy tissue. The combination of nanozyme and phage enabled simultaneous pathogen clearance and anti-inflammatory tissue repair, overcoming the limitations of traditional monotherapy approaches.

Although environment-responsive phage NP therapy enables precise immunomodulation and infection control, achieving localized and sustained delivery remains a major challenge for clinical translation. One such method involved creating a 3D-printed alginate hydrogel dressing that allowed locally isolated HZJ phages that target DH5α *E. coli* to be released continuously.[225] The phages' lytic activity was maintained by physically embedding them in the alginate fibre matrix in moderate circumstances. According to the experimental findings, the HZJ phage could lyse 57% to 67% of bacterial growth in 2 hours and remained stable at pH 6–9 and below 45 °C ($p < 0.001$). The antibacterial effect of the phage persisted for at least 24 hours post-encapsulation in hydrogel, maintaining a lytic activity between 85% and 90%. In a separate study, scientists employed guanidinium-functionalized poly(oxanorbornene)imide (PONI-Guan) to electrostatically assemble phage K, thereby creating a cationic polymer–phage nanoassembly (PPNs) that demonstrated efficacy against *S. aureus*, including MRSA.[226] This nanoassembly significantly enhanced the phage's capacity to penetrate bacterial biofilms. Compared to the 1-log10 reduction seen with free phages, improved PPNs produced a 3-log10 (~99.9%) reduction in the MRSA biofilm bacterial load *in vitro*. Confocal microscopy confirmed that PPNs penetrated deep into the biofilm matrix and released active phages to lyse the bacteria. In a murine MRSA wound biofilm model, PPNs significantly outperformed hydrogel-encapsulated phage K, which only achieved a 0.5-$\log_{10}$ reduction in bacterial load when applied using a Poloxamer 407 (P407) hydrogel. Mechanistically, the hydrogel matrix allowed for prolonged local phage release, whereas the cationic polymer promoted deeper biofilm penetration. This integrated platform offers a potential solution to the treatment challenges posed by bacterial infections in biofilm-associated wounds. Phage activity may be lost as a result of the laborious and unstable hydrogel fabrication procedure.[227] Sun *et al.* developed a phage encapsulation strategy based on a tannic acid–ferric ion (TA–Fe^{3+}) metal–phenolic network (MPN), which forms a protective coating on T4 phages *via* coordination interactions. This coating effectively protects phages from rapid protease degradation and immune clearance *in vivo*.[228] The MPN showed about 100% encapsulation efficiency with negligible phage activity influence. *In vitro* studies revealed that the MPN coating enhanced phage resistance to proteinase K by 2955-fold ($p < 0.01$), and more than 75% of phage activity was retained after 15 days of storage at 4 °C. T Encapsulated T4 phages released 9.09×10^8 PFU over 24 hours under acidic conditions (pH 5.0), achieving nearly 100% bacterial killing against *E. coli* and significantly outperforming their activity under neutral conditions (pH 7.4). Mice given MPN-encapsulated phages demonstrated nearly total wound closure on day 10 *in vivo*, with healing considerably faster than in the control group. Furthermore, after two days of treatment, the bacterial load in the wound was nearly

undetectable, and the antibacterial efficacy was comparable to that of antibiotic therapy ($p = 0.103$).

4.2 Implant and orthopedic infections

Implant-associated infections represent a significant challenge in the field of orthopedics, characterized by a high rate of disability and a substantial risk of recurrence, which have a considerable impact on patient prognosis.[220,229] The primary challenge is the formation of biofilms following bacterial adhesion to the implant surface, which subsequently leads to immune evasion and augmented drug resistance. Statistics show that implant-related problems account for about 25.6% of hospital-acquired infections worldwide. It has been demonstrated that biofilms produced by pathogens like *S. aureus* through the release of EPS can decrease antibiotic penetration efficiency by 10–1000 times, which can drastically impair therapeutic efficacy and hasten the formation of drug-resistant strains.[230] Due to their high degree of selectivity, capacity for replication, and low toxicity to mammalian cells, phages are increasingly recognized as a promising solution to address the limitations of antibiotics. In recent years, phage-based material techniques have demonstrated significant advancements in the domains of biofilm penetration, local delivery, implant surface modification, and multifunctional synergy. These advancements offer novel strategies for the treatment and prevention of infections.

To address the challenge of poor antibiotic penetration caused by the EPS barrier in mature biofilms, Wang *et al.* designed a phage–liposome nanoconjugate (Lip@Phage) platform. In this strategy, the phage Sb-1 functions as a targeting and guiding agent, facilitating the delivery of liposomes into bacterial biofilms and degrading the EPS matrix to enhance liposome penetration and synergistic therapeutic efficacy (Fig. 9A).[231] In contrast to control groups, Lip-RIF@Phage fully inhibited heat generation (Fig. 9B) and abolished measurable bacterial counts of MRSA (Fig. 9C). The phage–liposome nanoconjugates' EPS-degrading activity, which was mediated by phage tail-encoded depolymerases, allowed for deeper liposome penetration and led to significant biofilm breakup and a dramatic decrease in viable bacteria (Fig. 9D). In a rat model of prosthetic joint infection, Lip@Phage therapy dramatically decreased bioluminescent imaging signals, suggesting a considerable reduction in the bacterial load at the infection site (Fig. 9E). In comparison to the control group, the Lip@Phage group exhibited a decrease in CFU count by more than three orders of magnitude, whilst the Lip-RIF@Phage treatment group demonstrated no signs of bacterial presence.

Beyond biofilm penetration, another critical aspect of implant-associated infections is the need for a sustained and controlled release of therapeutic agents. This has led to the development of a phage-loaded hydrogel platform, which combines antimicrobial activity with bone tissue regeneration. Phage LM99 encapsulated in an alginate-nano hydroxyapatite (Alg-nanoHA) hydrogel enables the sustained release of phage with a pH-regulated release rate of over 95% within 24 hours under pH 7–9 (Fig. 9F and G).[232] *In vitro* results demonstrated that the hydrogel exhibited a substantial antibacterial effect against MDR *Enterococcus faecalis* (*E. faecalis*), with the capacity to inhibit the growth of approximately 99% of planktonic bacteria and 92%–98% of adherent bacteria. In an infected femur model, the bacterial load was reduced by up to 99.9% within 48 hours. These findings substantiate the efficacy of the hydrogel in combating MDR *E. faecalis*. Furthermore, the hydrogel exhibited favorable biocompatibility and notably augmented osteoblast proliferation, collagen deposition, and mineralization levels (Fig. 9H).

In addition to targeting bacterial infections, addressing early-stage bacterial adhesion and thrombus formation is equally crucial. To this end, a polydimethylsiloxane (PDMS) surface functionalized with immobilized phages and nitric oxide (NO) has been developed. This dual-functional surface provides both phage-mediated antibacterial precision and NO-mediated platelet inhibition.[233] Experiments showed that phage densities on PDMS and SNAP-PDMS surfaces were 2.4 ± 0.54 and 2.1 ± 0.33 phages per μm^2, respectively, with strong infectivity. In a 6-hour bactericidal experiment, the SNAP-PDMS-Phage surface had a bacterial killing efficiency of 99.99% with a standard deviation of 0.08% and decreased adherent bacteria by 99.80% with a standard deviation of 0.05%. These findings show that the SNAP-PDMS-Phage surface outperforms the NO-only surface, reducing bacteria by 91.57%. Furthermore, the prolonged release of NO resulted in a 64.65% reduction in platelet adhesion. The surface showed no hemolytic activity and supported fibroblast vitality of more than 97%, showing high biocompatibility.

Lastly, to tackle infection and corrosion issues in chromium-based dental implants, a dual-functional coating composed of AgNP and M13 phage was developed.[137] The substance exhibited strong broad-spectrum antibacterial action, eradicating all tested bacterial strains in 15 minutes at a dosage of 86.4 mg mL^{-1}, with *B. subtilis* exhibiting a 100% decrease in just two minutes (Fig. 9I). In addition to antimicrobial performance, trivalent chromium ions can selectively bind to amino groups on the phage surface, inducing AgNP aggregation through phage-mediated bridging. This aggregation enables a colorimetric detection strategy based on the absorbance ratio at 600 and 405 nm, achieving a detection limit as low as 14 nmol L^{-1} (Fig. 9J and K). This approach integrates infection control with real-time safety assessment through phage-enabled theranostics.

4.3 Blood infections

Sepsis, as a fatal syndrome caused by blood infection, often leads to multiple organ failure due to the rapid spread of pathogenic bacteria in the circulatory system, and has become one of the main causes of death in the global intensive care unit.[234,235] The problem is made worse by the infectious bacteria's rapid spread throughout the circulatory system, which makes effective therapy extremely difficult. Whilst phage therapy has emerged as a promising alternative to antibiotics due to its host-specific bactericidal potential, its clinical application is hindered by limitations such as short blood residence

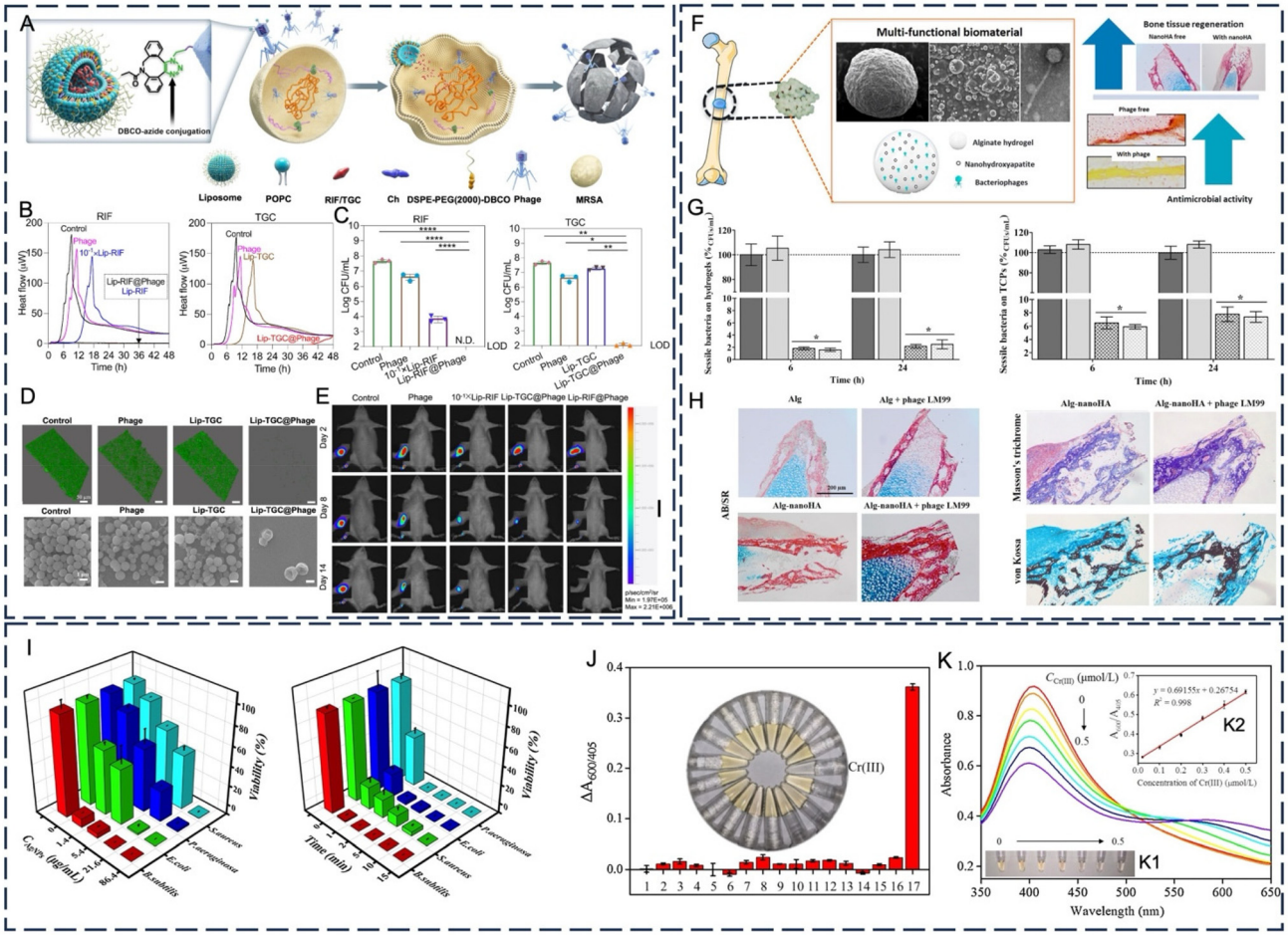

Fig. 9 Phage-NPs for implant and orthopedic infections. (A) Schematic illustration of phage-guided liposome and its interaction with MRSA. (B) Microcalorimetry profiles of MRSA biofilms following treatment with phage (10^8 PFU mL^{-1}), Lip-RIF, Lip-TGC, Lip-RIF@Phage, and Lip-TGC@Phage. Flat curves within the dashed box indicate MBBC-level activity, reflecting complete metabolic suppression. (C) Corresponding cell counts after 24 h; phage–liposome treatments reduced bacteria below the detection limit (100 CFU mL^{-1}). (D) Microcalorimetry shows suppressed metabolic activity in MRSA biofilms after phage–liposome treatments, with flat curves indicating MBBC and corresponding SEM images. (E) Representative *in vivo* bioluminescence imaging on days 2, 8, and 14. (F) Schematic illustration of phage-loaded alginate-nanohydroxyapatite hydrogel. (G) Sessile bacteria on hydrogels, and sessile bacteria on TCPs. (H) Histological analysis of embryonic femurs implanted with hydrogels. (I) Bacterial viability of four species as a function of incubation time and composite concentration after treatment with the AgNPs–M13 phage composite. (J) Selectivity of the AgNPs–M13 phage composite toward Cr(III) against various metal ions. Cr(III) and Al^{3+} were tested at 0.40 μmol L^{-1}; Pb^{2+} at 1.00 μmol L^{-1}; Fe^{3+} at 3.00 μmol L^{-1}; Cr(VI), Cu^{2+}, Zn^{2+}, and Hg^{2+} at 4.00 μmol L^{-1}; all others at 10.00 μmol L^{-1}. Inset shows colorimetric responses of the corresponding solutions. (K) UV-vis absorption spectra of the composite in the presence of increasing Cr(III) concentrations ranging from 0 to 0.50 μmol L^{-1}. Inset K1 shows the corresponding color changes; inset K2 shows the absorbance ratio (A_{600}/A_{405}) as a function of Cr(III) concentration. (A) to (E) Reproduced with permission from ref. 231, Copyright 2024, Elsevier. B.V. (F) to (H) Reproduced with permission from ref. 232, Copyright 2019, Elsevier. Inc. (I) to (K) Reproduced with permission from ref. 137, Copyright 2019, Elsevier. B.V.

time, insufficient targeting efficiency, and the limited bactericidal capacity of monotherapy.

In addressing the challenge of short blood residence time in phage therapy, Jin *et al.* developed a phage–platelet hybrid NP (PPHN) to enhance antibacterial efficacy through a biomimetic strategy (Fig. 10A and B).[236] The study engineered an M13 phage (BCP1-BGL) to display a blood circulation-prolonging peptide (BCP1, containing an RGD motif) and express the bactericidal enzyme Bgl II (Fig. 10C). *In vivo* studies demonstrated that PPHNs extended blood retention by 10–100-fold compared to free phages, maintaining phage titers 100-fold higher than the free phage group at 96 hours (Fig. 10D). Importantly, in a prophylactic model where infection was introduced 18 hours after PPHN administration, the system still achieved near-complete bacterial clearance, surpassing the efficacy of unmodified phages and demonstrating prolonged therapeutic activity (Fig. 10E and F). In addition, compared with mice treated with BCP1-BGL, mice treated with PPHNs showed decreased levels of proinflammatory cytokines, endotoxin, and liver damage markers (Fig. 10G–I). The therapeutic advantage was attributed to the BCP1-RGD-mediated long-circulating effect *via* platelet integrin binding and the

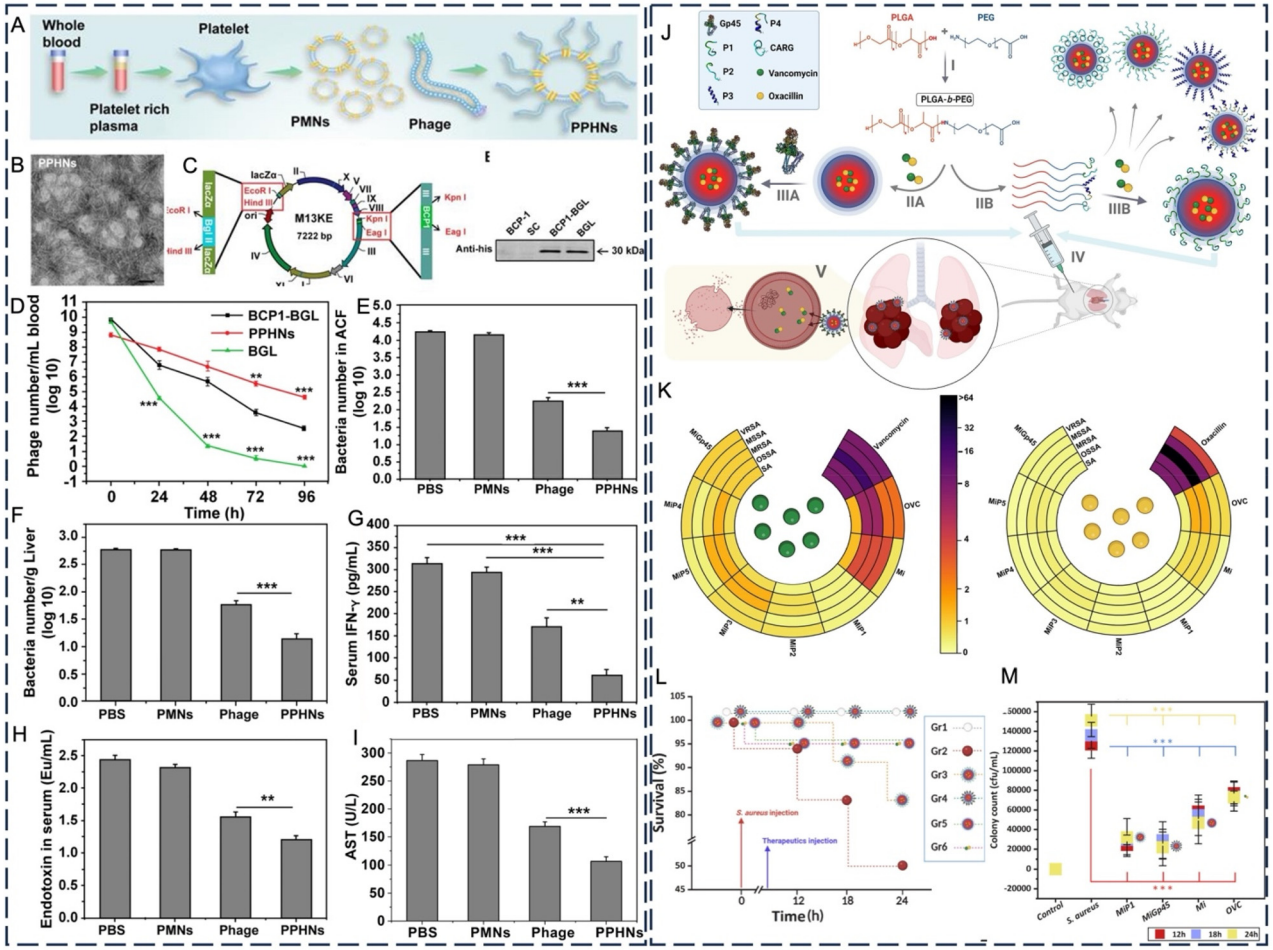

Fig. 10 Phage-NPs for blood infections. (A) Schematic illustration of PPHNs. PLTs extracted from 1 mL of rat blood were used to prepare platelet membrane NPs (PMNs), followed by incubation with 5.2×10^{12} pfu of phages. PPHNs were isolated through centrifugation, followed by several washes with PBS. (B) TEM images of PMNs (left) and PPHNs (right) negatively stained with uranyl acetate. Scale bar, 100 nm. (C) Schematic illustration of long-circulating antimicrobial phage construction. (D) Blood circulation time comparison between the BCP1-BGL phage, PPHNs, and the BGL phage. The same number (1×10^{11} pfu) of individual phages was separately injected into rats with phage titers in the blood determined at various time points. (E) Anti-bacterial efficacy of PPHNs in ACF. (F) Anti-bacterial efficacy of PPHNs in the liver. The number of viable bacteria per gram of liver tissue was determined with colony formation assay. (G) Evaluation of serum IFN-γ. Bac, bacteria. (H) Endotoxin release assay. Endotoxin level in the culture supernatant was determined by ELISA at various time points following phage infection of *E. coli*. (I) Assessment of serum aspartate aminotransferase (AST) levels. (J) Schematic illustration of PLGA-*b*-PEG copolymer synthesis, preparation of dual antibiotic-loaded micelles *via* two targeting strategies, and its *in vivo* evaluation in *S. aureus*-induced sepsis mice. (K) Heatmap of MIC values comparing free antibiotics, OVC mixture, and targeted/non-targeted nanodrugs against various *S. aureus* strains. MICs for formulations were calculated based on vancomycin and oxacillin content. MiP1 exhibited the lowest MIC values across all strains. (L) Survival rates of infected animals over time. (M) Quantification of *S. aureus* in bronchoalveolar lavage and blood samples at 12, 18, and 24 hours post-treatment. (A) to (I) Reproduced with permission from ref. 236, Copyright 2021, Ivyspring International Publisher. (J) to (M) Reproduced with permission from ref. 237, Copyright 2025, Elsevier. B.V.

infection resilience conferred by multi-phage loading, which ensured robust antibacterial activity even when a portion of phages was inactivated.

Building on biomimetic and targeted delivery concepts, Ozbek *et al.* engineered polymeric micelles decorated with phage-derived targeting moieties to combat *S. aureus* sepsis.[237] By conjugating the receptor-binding protein Gp45 from phage ϕ11 or its peptide fragments P1–P5 to PLGA-*b*-PEG micelles loaded with vancomycin and oxacillin, the study created dual antibiotic-loaded nanocarriers with enhanced bacterial specificity (Fig. 10J). Even non-targeted micelles exhibited potent synergistic effects, reducing vancomycin MICs by 2–10 fold and oxacillin MICs by 9–75 fold across clinical strains, including methicillin-resistant strains (Fig. 10K). MiGp45 and MiP1-targeted micelles further reduced the MIC by at least twofold and by up to ninefold in resistant strains, indicating a marked enhancement in antibacterial efficacy (data from Table 2 in ref. 237) In a mouse sepsis model, infection of mice with MiGP45-targeted nanomedicines by intraperitoneal injection resulted in no animal deaths, leading to 100% survival (Fig. 10L). In addition, the average colony size of the treatment group with the targeted nanomedicines (MiGP45 and MiP1)

was significantly reduced, with results very similar to those of the healthy group (Fig. 10M). This approach highlights the potential of phage-mimetic targeting to boost antibiotic efficacy and reduce systemic toxicity.

Besides, Wu *et al.* advanced phage-based PDT by engineering phages with the AIE TBTCP-PMB, achieving potent synergistic antibacterial effects against MDR pathogens.[210] *In vitro*, the phage–nanomaterial platforms exhibited a synergistic bactericidal effect, as the engineered phages, when exposed to light irradiation at 80 mW cm^{-2} for 20 minutes, reduced bacterial viability of MRSA and *E. coli* to below 1%, markedly outperforming either monotherapy, which resulted in 50–70% and 30–50% survival rates, respectively. In addition to this work, which examined sepsis samples from selected human sources, this AIE-PS engineered phage was successfully used to diagnose bacterial species and photodynamically inactivate Gram-positive or Gram-negative bacteria in clinical samples within about 30 minutes.

4.4 Bacterial infections in the tumor microenvironment

A mounting body of research has demonstrated the critical role that dysbiosis of the gut microbiota plays in the onset and spread of colorectal cancer (CRC), with *Fusobacterium nucleatum* (*F. nucleatum*) emerging as a major pro-oncogenic species.[238–240] *F. nucleatum* contributes to tumorigenesis by activating inflammatory signaling pathways, reshaping the immune microenvironment, and inducing chemoresistance through autophagy-related mechanisms.[238,241,242] Notably, *F. nucleatum* promotes protective autophagy in tumor cells, which reduces the deadly efficacy of chemotherapeutics like irinotecan. These results imply that *F. nucleatum* is a functional driver of disease progression and treatment failure in addition to being a microbial biomarker of colorectal cancer.[238]

Targeted elimination of tumor-associated bacteria like *F. nucleatum*, whilst preserving beneficial commensals, represents a novel and promising strategy to enhance anti-cancer therapy. To this end, a study created a phage-guided biotic–abiotic hybrid nanomaterial that improves chemotherapy and restores the balance of gut microbes whilst specifically targeting *F. nucleatum* (Fig. 11A).[98] The phage P2, which is unique to *F. nucleatum*, was initially isolated from human saliva and showed potent lytic activity against *F. nucleatum* whilst having no effect on other symbiotic strains. Bioorthogonal click chemistry was used to chemically modify the phage with azide groups (A-phage) and covalently attach it to dibenzocyclooctyne-functionalized irinotecan-loaded dextran NPs (D-IDNP). With a threefold increase in intratumoral drug enrichment over free IDNPs, this approach allowed the drug-loaded NPs to accumulate selectively at tumor locations, lowering off-target damage in healthy intestinal tissue (Fig. 11B). Functionally, the removal of *F. nucleatum* by phage reduced TLR4–Myd88-driven autophagy, upregulated anti-autophagy genes and downregulated pro-autophagy genes. The combined treatment promoted of the growth of anti-tumoral butyrate-producing bacteria, increased survival, and reduced the number of tumors in the intestine by 59% (Fig. 11C and D). Expanding on phage-enabled antibacterial immunotherapy, another study employed phage display technology to isolate an M13 phage that specifically binds *F. nucleatum*, and subsequently assembled AgNP to construct M13@Ag (Fig. 11E).[243] TEM images revealed the filamentous morphology of M13 phages and demonstrated that both M13 and M13@Ag exhibited strong binding affinity to *F. nucleatum* (Fig. 11F). M13@Ag effectively eliminated *F. nucleatum* at an equivalent Ag^{+} concentration of 1.44 μg mL^{-1}. Moreover, M13@Ag was shown to activate antigen-presenting cells, leading to about a 2-fold increase in dendritic cell maturation and about a 2.5-fold enhancement in M1 macrophage polarization, thereby promoting antitumor immune responses (Fig. 11G). *In vivo*, within an orthotopic CRC model, M13@Ag in combination with either immune checkpoint blockade (anti-PD1) or chemotherapy (FOLFIRI) achieved tumor suppression levels 2.5-fold and 2-fold greater, respectively, than M13@Ag monotherapy. The combination therapy also prolonged mouse survival from 23 days (monotherapy) to 35 days and was capable of reversing the immunosuppressive tumor microenvironment (Fig. 11H).

In addition to *F. nucleatum*, *Streptococcus gallolyticus* (*S. gallolyticus*) has also been implicated in CRC, particularly in the context of chronic inflammation. Sustained colonic inflammation facilitates early adenoma formation and augments *S. gallolyticus* colonization. *S. gallolyticus* has been demonstrated to promote tumorigenesis by activating the pro-inflammatory COX-2 pathway, which is a key factor in cancer development.[244] To counter this, a hybrid nanoplatform (DNPs@P) was designed by conjugating DNA origami nanosheets with *S. gallolyticus*-specific phage (Fig. 11I and J).[245] DNPs@P showed strong ROS-neutralizing capacity up to 45.5% ABTS scavenging, enhanced CT26 cell viability over 70%. The coating improved ROS scavenging in simulated gastric fluid and preserved phage titres. In the colitis model, DNPs@P-L reduced inflammatory cytokines, improved colon length, and restored microbial diversity. DNPs@P-L suppressed tumor formation, indicating that rDNPs@P-L combination therapy can effectively prevent tissue carcinogenesis and the transition from *S. gallolyticus*-induced colitis to cancer (Fig. 11K).

Collectively, these studies highlight the immense potential of phage-guided nanotherapies to reprogram the tumor microbiome, suppress immunosuppressive signaling, and enhance conventional cancer treatments. However, it remains unclear whether such strategies retain efficacy in tumors lacking colonization by target bacteria like *F. nucleatum* or *S. gallolyticus*. Future work should focus on patient stratification, expanded microbiome profiling, and combinatory therapeutic optimization to broaden the clinical applicability of these precision bacteriotherapies.

4.5 Bacterial pneumonia

Bacterial pneumonia remains a significant global health concern, contributing to substantial morbidity, mortality, and economic burden across all age demographics. The emergence of MDR Gram-negative bacteria (MDR-GNB) has introduced

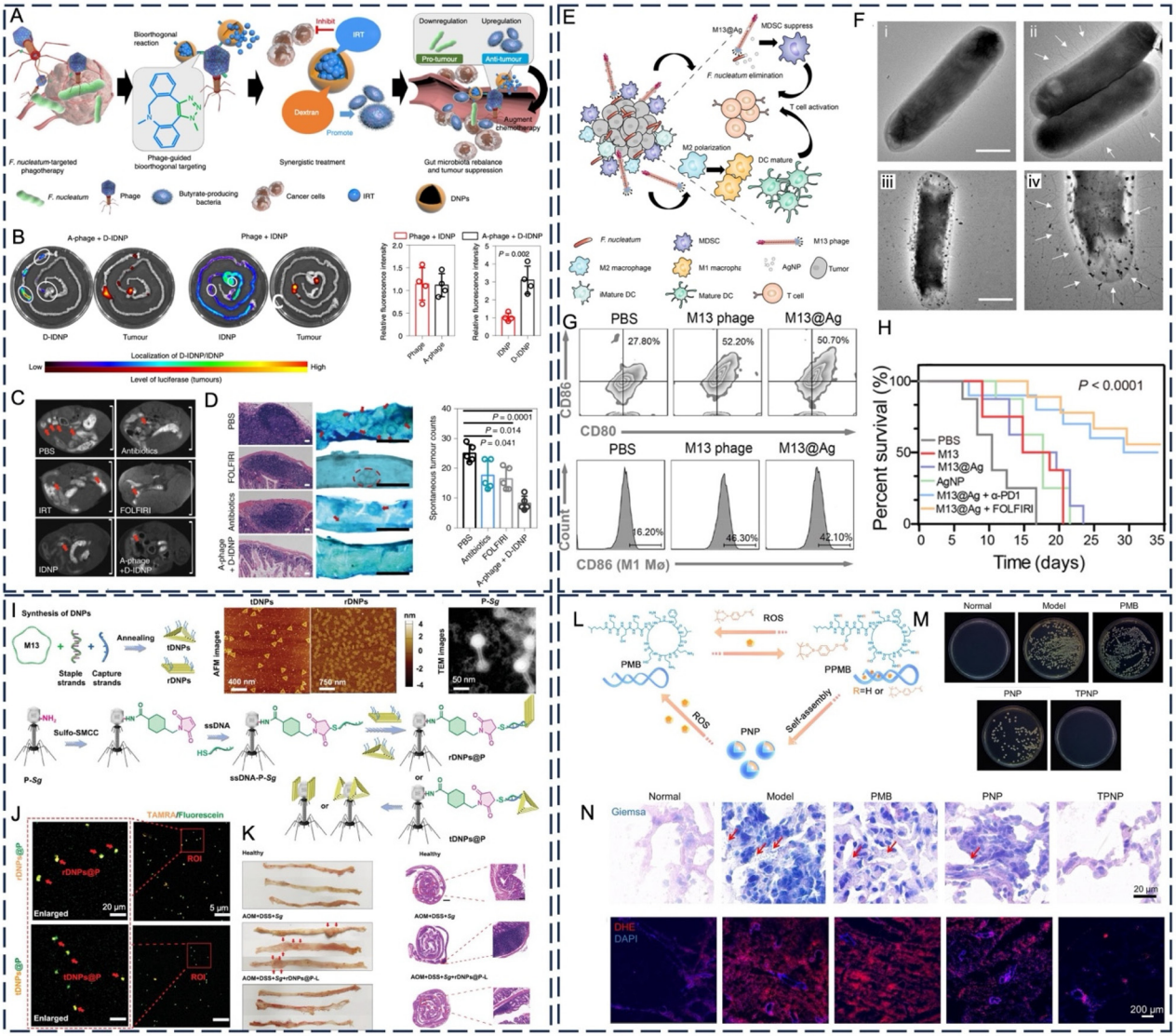

Fig. 11 Phage-NPs for targeting tumor-related bacteria and bacterial pneumonia. (A) A schematic representation of a phage-guided biotic–abiotic hybrid nanoplatform developed for CRC therapy, designed to selectively target tumor-associated *F. nucleatum*. (B) An abdominal imaging window was implanted in mice for real-time, longitudinal monitoring of tumor progression during treatment using stereomicroscopy. (C) *T*1-weighted MRI on day 14 showing orthotopic tumors with high signal intensity along the intestinal wall, indicative of invasive growth. Red arrows indicate suspected tumor nodes. Scale bar: 2 cm. (D) Histological analysis of spontaneous intestinal tumors in $Apc^{Min/+}$ mice after treatment demonstrated reduced tumor burden, as shown by H&E staining. (E) Conceptual illustration of the M13@Ag nanoplatform, designed to modulate gut microbiota and enhance anti-tumor immune responses. (F) TEM images of *F. nucleatum* (F-i), M13 phages targeting *F. nucleatum* (F-ii), and M13@Ag targeting *F. nucleatum* (F-iii and F-iv). (G) Flow cytometry analysis indicated that M13@Ag treatment promoted dendritic cell maturation and repolarization of M2 macrophages toward a pro-inflammatory M1 phenotype. (H) Kaplan–Meier survival curves demonstrated improved survival in mice treated with phage-based hybrid platforms. (I) Schematic and microscopy images depicted the design, assembly, and structural features of rDNPs and tDNPs, including their interaction with the model antigen P-*S. gallolyticus*. (J) Confocal microscopy showed the intracellular distribution of TAMRA-labelled DNPs and fluorescein-labelled P-*S. gallolyticus*, confirming effective co-localization. (K) Macroscopic and histopathological analysis of colon tissue revealed differences in tumor development among treatment groups. (L) A schematic highlights the conversion among PMB, PPMB, and PNP, with PNP exhibiting ROS-triggered drug release behavior. (M) Representative images of bacterial colony count from homogenized lung tissue were used to assess antibacterial efficacy. (N) Giemsa-stained lung sections and fluorescence imaging demonstrated bacterial presence and ROS distribution, respectively, under various treatment conditions. (A) to (D) Reproduced with permission from ref. 98, Copyright 2019, Springer Nature. (E) to (H) Reproduced with permission from ref. 243, Copyright 2020, AAAS. (I) to (K) Reproduced with permission from ref. 245, Copyright 2025, Wiley-VCH GmbH. (L) to (N) Reproduced with permission from ref. 91, Copyright 2025, Elsevier. B.V.

significant challenges to treatment protocols and has led to deteriorated patient prognoses. These pathogens are especially prevalent in hospital-acquired pneumonia and ventilator-associated pneumonia (VAP), with MDR-GNB accounting for 76.1%–95.3% of VAP cases and 49.7%–83.1% of community-acquired pneumonia.[246] Resistance to commonly used anti-

biotics, including ampicillin, tetracyclines, cephalosporins, and even carbapenems, is frequently reported. The urgent need for novel therapies is underscored by the increasing prevalence of MDR strains and hard-to-treat pathogens, which are adept at forming biofilms and resisting conventional antibiotics.

In response to the growing threat posed by MDR-GNB, Dong *et al.* designed a biohybrid platform TPNP combining polymyxin B (PMB) that integrates chemical prodrugs and engineered phages for synergistic antimicrobial therapy.[91] PMB was conjugated with phenylboronic acid pinacol esters (PBAP) to produce a ROS-labile prodrug (PPMB), which was then encapsulated in PLGA-DSPE-PEG NPs (PNP) (Fig. 11L). The PNPs were covalently linked to a phage that targets important MDR-GNB species, including *K. pneumoniae*, *P. aeruginosa*, and *A. baumannii*. *In vitro*, TPNP demonstrated controlled PMB release when exposed to H_2O_2 and O_2^-, whilst maintaining bactericidal efficacy analogous to that of free PMB. In a rat pneumonia model, TPNP improved survival from 20% (PMB group) to 90% (TPNP group), suppressed proinflammatory cytokines, and reduced lung bacterial burdens from 6.41 to 2.93 $\log_{10}$ CFU (Fig. 11M). Bacterial survival and the lowest levels of ROS can be observed in TPNP-treated lung tissue (Fig. 11N).

Whilst Gram-negative pathogens predominate in the context of drug-resistant pneumonia, Gram-positive bacteria, such as MRSA, also pose substantial clinical challenges. In addressing this challenge, Liu *et al.* developed an inhalable phage-based dry powder formulation, meticulously designed for localized, non-invasive treatment of MRSA pneumonia.[23] The platform consists of porous PLGA microspheres encapsulating ICG-conjugated phage (PMPs-PI), which are designed to activate PTT under NIR light. The selected phage (designated as NKU-1) demonstrated high specificity to MRSA and retained infectivity upon ICG modification. In the experimental setting, PMPs-PI demonstrated a noteworthy efficacy in the treatment of MRSA, achieving a 97.1% mortality rate within a 40-minute timeframe following 808 nm laser irradiation. *In vivo*, aerosol delivery enabled targeted lung accumulation, reducing bacterial burden by 2.5 $\log_{10}$ CFU within 48 hours. It is noteworthy that the formulation demonstrated remarkable room-temperature stability, sustaining phage titres for over 12 days, thereby substantiating its capacity as a shelf-stable, light-activated pulmonary therapy. Table 5 summarizes representative phage-nano platforms in different disease models.

Although most studies have demonstrated promising antibacterial and therapeutic effects, these outcomes largely remain confined to simplified laboratory assays, such as Static *in vitro* biofilm models or animal models. The limited clinical translation of phage–nanomaterial platforms may stem from host immune clearance of phages, rapid enzymatic or oxidative degradation *in vivo*, and the heterogeneous, dynamic conditions of infection sites. To address these gaps, researchers should turn to intermediate models that better mimic physiological complexity. Traditional planktonic culture systems allow high-throughput screening but lack the three-dimensional architecture, microbial diversity and host factors that characterize true infection niches. By contrast, *ex vivo* biofilm models, derived from patient-isolated microbial communities or tissue explants, better recapitulate the dense extracellular matrix and species interactions that impede phage penetration and nanocarrier diffusion, though they remain constrained by short viability windows and inter-sample variability. For instance, Besser *et al.* developed the human plasma biofilm model (hpBIOM), which takes into account the effects of cellular and molecular components on biofilms associated with non-healing chronic wounds.[247] Some special microenvironments require the use of dynamic biofilm models for greater accuracy. For example, using a recirculation of nutritious media and bacteria through the flow chamber system simu-

Table 5 Representative phage–nanomaterial platform and delivery forms across disease models

Disease	Representative examples	Bacterial species	Delivery route	Ref.
Infected wounds	QD@Phage	MDR *P. aeruginosa* carbapenem-resistant	Topical Administration	221
	Phage@Pd	*P. aeruginosa* & *E. coli*	Topical administration	223
	Phage-Chlorin e6-MnO_2	*S. aureus*	Topical administration	24
Implant and orthopedic infections	Lip-RIF@Phage	MRSA	Topical administration	231
	ChitoAntibac PDMS released phage K	*S. aureus*	Coating Coating	220
	SNAP-PDMS-Phage	*E. coli*		233
Blood infections	phage-platelet hybrid NP	*E. coli*	Intravenous administration	236
	Gp45–PLGA micelles (VAN/OXA)	*S. aureus*	Intraperitoneal injection	237
Tumor bacterial infections	M13@Ag	*F. nucleatum*	Oral administration	98
	DNPs@P	*S. gallolyticus*	Oral administration	245
Bacterial pneumonia	PNP	MDR-GNB	Intravenous administration	91
	PMPs-PI	MRSA	Nebulized administration	23

Abbreviations: ChitoAntibac, chitosan-based antibacterial coating; DNPs@P, DNA nanopatches@Phage; *E. coli*, *Escherichia coli*; *F. nucleatum*, *Fusobacterium nucleatum*; Gp45–PLGA micelles (VAN/OXA), Gp45 peptide–modified PLGA-PEG micelles co-loaded with vancomycin and oxacillin; MDR, multidrug-resistant; Lip, liposome; *P. aeruginosa*, *Pseudomonas aeruginosa*; PDMS, polydimethylsiloxane; PMPs-PI, porous PLGA microspheres encapsulating ICG-conjugated phage; PNP, prodrug nanoparticle; QD, Quantum dots; RIF; Rifampicin; *S. aureus*, *Staphylococcus aureus*; *S. gallolyticus*, *Streptococcus gallolyticus*.

lates physiological flow conditions in the oral cavity[248] A custom 3D-printed flow system perfuses nutrient medium beneath an agar plate capped with a semipermeable membrane, supporting biofilm growth while mimicking the air–liquid interface and exudate flow of chronic wounds.[249] Organoid systems, on the other hand, recreate key aspects of human tissue microanatomy, including epithelial barriers, multicellular crosstalk and innate immune components, providing a more realistic context for evaluating phage trafficking, immune modulation and off-target cytotoxicity. By integrating these intermediate platforms with targeted animal studies, which uniquely inform on systemic distribution, pharmacokinetics and immunogenicity, researchers can triangulate efficacy and safety data under progressively more physiologically relevant conditions. Such a tiered approach, moving from *in vitro* screens through *ex vivo* and organoid assays to *in vivo* validation, will be essential to deconvolute the mechanism of action, identify failure modes, and accelerate the rational design of clinically translatable phage–nanomaterial therapeutics.

5. Challenges and future perspectives

Phage–nanomaterial platforms have made significant strides in development, but a number of significant obstacles still stand in the way of their long-term use and clinical translation. These include worries about immunogenicity and biosafety, the possibility that NPs could promote HGT, and the requirement for intelligent, customized, and multipurpose therapeutic platforms. This section offers a critical summary of these problems, identifies existing constraints, and talks about potential future paths to direct the safe and efficient application of next-generation phage-based nanotherapies.

5.1 Evaluation of the safety and immunogenicity of phage therapy

A systematic review and meta-analysis indicated that phage therapy significantly improved survival rates and effectively reduced bacterial burdens in animal models of systemic infection, skin infection, and pneumonia.[250] Uyttebroek *et al.* reviewed 52 clinical trials conducted between 2000 and 2021 and concluded that phage therapy generally exhibits a favorable safety profile. Compared to the control group (15%), the incidence of adverse events in the phage-treated group was lower (only 7%), with most reactions being mild and reversible. Among the 59 studies evaluating therapeutic efficacy, approximately 79% of patients showed clinical improvement, and 87% achieved bacterial clearance.[251] Even in severe infections such as infective endocarditis and septic shock, phage therapy as an adjunct treatment demonstrated good tolerability with no significant emergence of phage resistance.[252]

However, immunogenicity remains a critical barrier to the long-term clinical application of phage therapy. Repeated administration often induces the production of anti-phage antibodies, which can neutralize phage activity and compromise subsequent therapeutic efficacy. A recent 14-year retrospective study found that 38.5% (5 out of 13) of screened patients developed phage-neutralizing responses.[253] Another clinical study involving cystic fibrosis patients also reported that neutralizing antibodies could be detected in serum within 10 to 42 days following inhaled phage therapy.[254] To address these challenges, future directions point toward the development of phage–nanomaterial hybrid platforms. These platforms can enhance local targeting, reduce phage exposure time *in vivo*, and synergies with the antimicrobial mechanisms of nanomaterials to maximize antibacterial efficacy within the early therapeutic window, thereby minimizing immune recognition. Moreover, nanoplatforms can be engineered to modulate the release kinetics of phages or incorporate low-immunogenic materials as protective barriers, which may delay the initiation of immune responses and provide a broader time window for effective clinical intervention.

Notably, nanodelivery platforms such as liposomes or polymeric particles can shield phage to some extent and delay immune clearance, but they also introduce a new safety concern: endotoxin residues in phage lysates are often highly immunogenic and can induce severe inflammatory reactions if not completely removed. In addition, some cationic polymers or inorganic nanomaterials used as delivery vehicles may also be cytotoxic or irritating. Therefore, the immunogenicity and biosafety of phage nanoplatforms, in particular endotoxin residues and host immune responses, need to be systematically evaluated prior to clinical translation.

5.2 Clinical translation challenges of phage and phage nanomaterial platforms

From a regulatory standpoint, the clinical translation of phage therapy presents several challenges that must be carefully addressed to enable its widespread adoption. In the United States, for example, the FDA classifies phages as biological medicinal products. As a result, phage therapies require an Investigational New Drug (IND) application and adherence to strict Good Manufacturing Practice (GMP) standards to guarantee the safety, efficacy, and quality of the product.[255] Conversely, in Europe, the European Medicines Agency regulates phages primarily as conventional medicinal products under existing drug directives, although no specific phage-based medicine has yet received formal approval.[256] Notably, the regulatory frameworks differ: the US system emphasizes centralized phage banks and adaptive IND pathways, while the EU relies more on national magistral preparations and evolving regulatory guidance. These differences create fragmented approval pathways and complicate the global harmonization of phage-based therapeutics.[257] Currently, phage therapy is being used to treat hard-to-treat infections in the United States, Australia, Israel and several European countries. In the UK, phage therapy is only being used on an *ad hoc* basis, with limited availability due to procurement difficulties and a lack of sustainable access to phages manufactured.[258]

Despite these regulatory complexities, several phage therapies have advanced into clinical evaluation, illustrating growing translational momentum. For instance, a Phase 1b/2a clinical trial investigated an inhaled cocktail of three phages targeting *P. aeruginosa* in cystic fibrosis patients. This study demonstrated favorable safety and tolerability profiles, alongside encouraging preliminary evidence of reduced bacterial load in the lungs.[60] These advances in phage monotherapy lay a critical foundation for the further development of more complex delivery systems. In particular, preclinical work has examined combinations of phages and nanomaterials to improve targeting and therapeutic outcomes. One notable example involved coupling a *Pseudomonas aeruginosa*-specific phage cocktail with apoptotic-mimicking liposomes, which significantly improved bacterial clearance compared to the individual components.[259] Such findings highlight the potential of hybrid platforms to overcome limitations of conventional phage therapy.

However, transitioning these hybrid systems into clinical-grade products remains significantly more challenging. Manufacturing processes must effectively remove bacterial endotoxins and contaminants while preserving the viability and activity of the phages. Furthermore, achieving consistent phage titers and purities across batches is essential for reproducibility and regulatory compliance. This complexity is magnified in multi-phage cocktails, where each phage strain requires independent characterization and potency testing.[257] For example, the PhagoBurn clinical trial revealed the considerable difficulty of maintaining quality control in a 12-phage cocktail, underscoring the urgent need for advanced analytical methods and standardized protocols.[257]

Phage–nanomaterial hybrid systems introduce additional translational hurdles due to ambiguous regulatory classification. Nanocarriers that transmit phages are usually regarded as combination products, subject to overlapping regulatory regimes that oversee both biologics and devices, because viruses do not fit within the category of medical devices. This dual classification can greatly extend approval timelines and require coordinated review methods across regulatory jurisdictions. Furthermore, strict quality control is necessary for both hybrid components, confirming the phage's infectivity as well as the nanocarrier's physicochemical characteristics, including size, charge, release kinetics, and *in vivo* stability. Importantly, nanomaterials may pose biosafety risks specific to their composition, such as dose-dependent cytotoxicity, immunogenicity, or lack of biodegradability; these risks should be mitigated through well-defined dose thresholds, *in vivo* toxicity data, and degradability assessments during formulation development. The effective clinical translation of phage–nanomaterial therapies is significantly hampered by these complex requirements taken together. Unlocking the full therapeutic potential of phage–nanomaterial platforms in precision antimicrobial therapy will require addressing these manufacturing, regulatory, and quality control issues. In addition to technical innovation, regulatory alignment and scalable, standardized production paths that guarantee safety, efficacy, and reproducibility are necessary to close the gap between bench and bedside.

5.3 Potential risks of nanomaterials promoting resistance gene transfer

HGT plays a central role in the rapid dissemination of antibiotic resistance genes (ARGs) across bacterial species, allowing resistance traits to spread independently of clonal expansion. Key mechanisms include plasmid-mediated conjugation, phage-mediated transduction, and natural transformation. While conjugation is well-characterized, transduction and transformation are harder to detect using routine diagnostics, leading to underestimation of their clinical relevance. Given that many high-priority resistant pathogens are naturally transformable, and that ARGs can spread across unrelated strains *via* phage vectors, understanding and controlling HGT is critical in preventing the emergence and persistence of multidrug-resistant infections.[260] A current widely overlooked but extremely critical biosafety issue is the potential for nanomaterials to promote phage-mediated horizontal transmission of ARGs. It has been shown that certain NPs can significantly enhance phage HGT. Photoexcitation of TiO_2 NPs was found to significantly promote the formation of transducers with a much higher transduction efficiency than the sum of TiO_2 NPs or UV light alone.[261] Nano-TiO_2 concentration, particle size, mating time and the ratio of phage/bacteria could influence the transductive transfer of ARGs.[262] Similarly, Ag^+ or AgNPs and Cu^{2+} or CuO NPs accelerated phage-mediated transmission of ARGs in *planktic* and its biofilm.[132,263,264] The mechanism is related to NP-induced oxidative stress and cell membrane damage as well as intracellular ROS induction, which favor phage infection and DNA entry. This suggests that the combination of phage and nanomaterials for infection therapy may inadvertently facilitate the spread of ARGs in pathogenic bacterial populations, thereby posing a potential threat to disease treatment. Whilst enhancing phage infection efficiency, nanomaterials may also enhance the frequency of phage-mediated horizontal gene transfer by inducing ROS to generate a stress response in activated bacteria, leading to the acquisition of resistance in strains that are otherwise sensitive to antibiotics or phages. This dissemination of genetic material has the potential to not only diminish the efficacy of subsequent therapeutic interventions but also to precipitate the reemergence and chronicity of the infection or even to contribute to the ecological predominance of opportunistic pathogenic bacteria, thereby inducing secondary infections. Furthermore, the emergence of drug-resistant strains during antimicrobial therapy will significantly restrict the clinical application of such platforms, particularly in immunocompromised or critically ill patients.

Given the widespread application of nanoparticle–phage combinations, special attention should be paid to the biosafety concerns associated with nanoparticle-mediated HGT. To mitigate such risks, design strategies should include avoiding sublethal nanoparticle concentrations when selecting ROS-inducing materials and incorporating standardized HGT assays or

forecasting the dissemination of ARGs across bacterial genomes during the early-stage evaluation of therapeutic platforms. However, detecting phage-mediated or transformation-based HGT in clinical settings is inherently difficult due to their low frequency and the challenge of distinguishing transferred DNA from conserved chromosomal regions.[260] Unlike plasmids, these events often lack clear molecular signatures, making them hard to track without long-term metagenomic studies.[265] Currently, multiple machine learning methods, such as logistic regression, random forest, and graph convolutional networks, can forecast the horizontal transfer of ARGs or quantify the influence of these factors on the horizontal transfer of ARGs.[266,267] Integrating these biosafety measures into nanoparticle–phage engineering is essential to ensure translational feasibility while limiting ecological and clinical risks.

5.4 Development of smart, personalized, multifunctional phage–nanomaterial platform

The subsequent phase of phage–nanomaterial integration will extend beyond the enhancement of delivery and stability. Future research will focus on developing intelligent systems that are capable of responding to complex infection environments, accommodating individual patient needs, and interacting with host immunity or the microbiome. Whilst current research focuses primarily on commonly used inorganic nanomaterials, such as AgNPs, AuNPs, iron oxides, PSs and several polymeric carriers, a wide range of potentially phage-compatible antimicrobial materials and functionalities remains underexplored.

Some candidates, including two-dimensional structures such as black phosphorus, MXenes and graphdiyne, offer unique opportunities for engineering responsive phage delivery systems.[268–270] The materials in question have been demonstrated to exhibit tunable photothermal or photodynamic properties, as well as redox activity and selective affinity for bacterial membranes. Nanozymes, such as noble metals and metal oxides, enhance ROS production at infection sites *via* peroxidase-, oxidase-, or glucose oxidase-like activities, thereby facilitating phage penetration and antibacterial efficacy.[271,272] Conversely, anti-inflammatory nanozymes such as cerium oxide and Prussian blue help modulate immune responses and scavenge excess ROS, reducing collateral damage.[273,274] Porous materials such as metal–organic frameworks, covalent organic frameworks, porous organic polymers, and polymer–metal coordination networks offer distinct advantages for phage-based delivery systems.[275–277] Their highly tunable pore structures and large surface areas allow efficient phage or drug loading, while their chemical versatility supports stimuli-responsive release and integration with catalytic antimicrobial functions. These features make them strong candidates for next-generation phage–nano therapeutic platforms, especially in scenarios requiring co-delivery or controlled spatiotemporal release. Adaptive polymers and dynamic covalent materials that alter reversibly in response to physiological cues like pH, redox state, or enzyme activity represent another new avenue.[278–280] While incorporated logic-gate mechanisms, such as AND or OR circuits, would allow therapeutic activation only under specified infection-specific conditions, modular surface-switching designs could allow for on-demand reprogramming of phage mixtures. By preventing early activation, this improved selectivity helps to guarantee treatment precision. Additionally, micro- and nanorobotic systems provide active phage delivery to deep or biofilm-associated infections. Powered by magnetic, acoustic, or optical fields, these devices enable directional navigation and site-specific accumulation. When loaded with phages, they can penetrate biological barriers and release cargo *via* stimuli-responsive triggers, offering precision delivery beyond passive diffusion limits.[165,281]

From a therapeutic perspective, smart phage–nanomaterial platforms have the potential to not only eliminate pathogens but also to regulate the infection microenvironment. A combination of phages with quorum-sensing inhibitors, biofilm-disrupting agents, or immune checkpoint modulators has been posited as a means of targeting both microbial and host regulatory pathways.[282–284] It is hypothesized that future multifunctional platforms will involve the co-delivery of CRISPR-Cas systems.[67,285] The purpose of this co-delivery would be to selectively eliminate resistance genes while preserving beneficial microbiota. The field of personalization is of considerable importance, albeit in its infancy. While synergistic phage-antibiotic combinations and strain-specific matching are under investigation, few studies have integrated real-time diagnostics, microbiome profiling, or host immune biomarkers into therapeutic design.

In the future, the use of artificial intelligence (AI) in the modeling of phage–bacteria–host interactions has the potential to support the development of personalized therapeutic constructs. A major current bottleneck is the slow and labor-intensive manual screening of suitable phages, yet advances in sequencing and AI algorithms now allow rapid whole-genome-based matching. For instance, recent studies have demonstrated that machine learning algorithms can reliably predict infectious phages from bacterial genomic features, enabling high-precision host matching at the strain level and the design of phage cocktails effective against previously untested strains.[286,287] Beyond host–phage matching, AI can be applied to gene function mining, for example by predicting phage protein roles or host interaction domains from sequence data. Additionally, it can streamline the design and assembly of large-scale phage libraries, prioritizing candidates for experimental validation and accelerating the discovery of novel therapeutic phages. By efficiently navigating massive genomic datasets, AI can accelerate the discovery and optimization of therapeutic candidates, thus streamlining the development of personalized phage-based treatments. Another promising application is AI-guided formulation, which could address limitations in phage storage stability and cold-chain dependence. Machine learning models trained on genomic, structural, and stability data could predict strains with inherent tolerance to ambient storage or identify excipient combinations

that improve storage stability. Such *in silico* screening would enable rapid assessment of formulation parameters and the forecasting of optimal conditions to preserve phage infectivity for months, facilitating long-term storage without refrigeration.

Furthermore, programmable phage–nanomaterial constructs can be engineered to display bespoke binding peptides, catalytic domains, or stimulus-responsive linkers such as pH-sensitive or enzyme-cleavable motifs. These modifications enable site-specific cargo loading, environment-triggered release, and ordered self-assembly into bioinspired architectures. When integrated with nanomaterials, these programmable scaffolds enhance targeting selectivity, reduce off-target toxicity, and dynamically adapt to complex pathological microenvironments such as hypoxic, inflammatory, or biofilm-associated niches. The inherent programmability of the phage scaffold enables the deliberate design, high-throughput screening, and directed evolution of target-binding moieties, providing a versatile basis for fully customizable theranostic platforms. Advances in sensing and programmable delivery could converge to create integrated therapeutic–diagnostic systems capable of real-time infection monitoring and precision intervention. Such systems may take the form of wearable or implantable devices equipped with miniaturized sensing modules to detect infection-specific biochemical cues, such as wound acidification or pathogen-secreted proteases. Upon detection, these modules could trigger the targeted release of encapsulated phage–nanomaterial formulations from an on-board reservoir. This closed-loop control would allow precise spatial and temporal dosing, minimizing off-target exposure and adapting release profiles to the evolving infection. Coupled with wireless data transmission, such devices could support remote monitoring and enable clinician-guided adjustments, reducing reliance on systemic antibiotics.

In addition to the above concerns, despite technical progress in personalized phage therapy, large-scale implementation remains constrained by limited production capacity in clinical settings and low industry engagement. Public funding may provide partial support, but high treatment costs persist, highlighting the need for interventions of national healthcare systems.[288] Compared with phage therapy, alternative targeting ligands such as aptamers offer lower production costs.[289,290] However, their therapeutic translation may be constrained by the high costs of screening, optimization, and functional validation, and they lack the intrinsic bactericidal activity of phages.[291] As regulatory frameworks become more defined, safety evaluation systems more standardized, and nanobiotechnologies increasingly mature, phage nanomaterial platforms are expected to advance towards clinical translation for precision antibacterial therapy.

Conflicts of interest

The authors declare no conflict of interest.

Data availability

No primary research results, software or code have been included and no new data were generated or analysed as part of this review.

Acknowledgements

This work was supported by the China Scholarship Council (CSC, 202406170238 to M. Q.). The graphical abstract, Fig. 1–3, and Fig. 7(C)–(E) were created with **BioRender.com**.

References

1 M. Naghavi, S. E. Vollset, K. S. Ikuta, L. R. Swetschinski, A. P. Gray, E. E. Wool, G. R. Aguilar, T. Mestrovic, G. Smith and C. Han, *Lancet*, 2024, **404**, 1199–1226.
2 B. Aslam, R. Asghar, S. Muzammil, M. Shafique, A. B. Siddique, M. Khurshid, M. Ijaz, M. H. Rasool, T. H. Chaudhry and A. Aamir, *Global. Health*, 2024, **20**, 73.
3 H.-C. Flemming, E. D. van Hullebusch, B. J. Little, T. R. Neu, P. H. Nielsen, T. Seviour, P. Stoodley, J. Wingender and S. Wuertz, *Nat. Rev. Microbiol.*, 2025, **23**, 87–105.
4 H. Jan, S. Ghayas, D. Higazy, N. M. Ahmad, A. Yaghmur and O. Ciofu, *J. Colloid Interface Sci.*, 2024, **669**, 537–551.
5 S. Barman, L. B. Kurnaz, R. Leighton, M. W. Hossain, A. W. Decho and C. Tang, *Biomaterials*, 2024, **311**, 122690.
6 M. Siopi, D. Skliros, P. Paranos, N. Koumasi, E. Flemetakis, S. Pournaras and J. Meletiadis, *Clin. Microbiol. Rev.*, 2024, **37**, e00044–e00024.
7 B. K. Chan, G. L. Stanley, K. E. Kortright, A. C. Vill, M. Modak, I. M. Ott, Y. Sun, S. Würstle, C. N. Grun and B. I. Kazmierczak, *Nat. Med.*, 2025, **31**, 1494–1501.
8 S. Rao, M. Betancourt-Garcia, Y. O. Kare-Opaneye, B. E. Swierczewski, J. W. Bennett, B. A. Horne, J. Fackler, L. P. Suazo Hernandez and M. J. Brownstein, *Antimicrob. Agents Chemother.*, 2022, **66**, e00824–e00821.
9 M. K. Kim, G. A. Suh, G. D. Cullen, S. P. Rodriguez, T. Dharmaraj, T. H. W. Chang, Z. Li, Q. Chen, S. I. Green and R. Lavigne, *J. Clin. Invest.*, 2025, **135**, e187996.
10 A. Khosravi, Q. Chen, A. Echterhof, J. L. Koff and P. L. Bollyky, *Lung*, 2024, **202**, 223–232.
11 C. Liu, T. Tian, Y. Shi, M. Li, L. Hong, J. Zhou, J. Liu, Y. Zhong, X. Wang and Z. Wang, *Aggregate*, 2025, **6**, e666.
12 M. Qi, X. Li, X. Sun, C. Li, F. R. Tay, M. D. Weir, B. Dong, Y. Zhou, L. Wang and H. H. Xu, *Dent. Mater.*, 2019, **35**, 1665–1681.
13 J. Dong, G. Liu, Y. V. Petrov, Y. Feng, D. Jia, V. E. Baulin, A. Yu Tsivadze, Y. Zhou and B. Li, *Adv. Healthcare Mater.*, 2024, **13**, 2402568.
14 S. Shabani, S. Hadjigol, W. Li, Z. Si, D. Pranantyo, M. B. Chan-Park, N. M. O'Brien-Simpson and G. G. Qiao, *Nat. Rev. Bioeng.*, 2024, **2**, 343–361.

15 A. N. Juaim, J. Sun, R. Nie, W. Li, L. Ding, K. Wang, J. Zhou, M. Li, M. Chi and B. Dong, *Small*, 2025, 2500382.
16 W. Sun, J. Sun, Q. Ding, M. Qi, J. Zhou, Y. Shi, J. Liu, M. Won, X. Sun and X. Bai, *Angew. Chem.*, 2024, **136**, e202319690.
17 S. K. Mondal, S. Chakraborty, S. Manna and S. M. Mandal, *RSC Pharm.*, 2024, **1**, 388–402.
18 M. J. Mitchell, M. M. Billingsley, R. M. Haley, M. E. Wechsler, N. A. Peppas and R. Langer, *Nat. Rev. Drug Discovery*, 2021, **20**, 101–124.
19 J. Ma, K. Li and S. Gu, *RSC Adv.*, 2022, **12**, 4852–4864.
20 R. He, Y. Gu, J. Jia, F. Yang, P. Wu, P. Feng and C. Shuai, *Nanoscale Horiz.*, 2025, **10**, 681–698.
21 C.-Y. Hsu, S. Mansouri, J. Rizaev, G. Sanghvi, D. O. Bokov, I. Sharma, P. Rajput, Y. F. Mustafa and L. Hussein, *Nanoscale*, 2025, **17**, 8401–8414.
22 A. Petrosino, R. Saporetti, F. Starinieri, E. Sarti, L. Ulfo, L. Boselli, A. Cantelli, A. Morini, S. K. Zadran and G. Zuccheri, *IScience*, 2023, **26**, 108032.
23 M.-Y. Liu, X. Liu, C.-Y. Wang, Q.-Q. Wan, Y.-F. Tian, S.-L. Liu, D.-W. Pang and Z.-G. Wang, *Nano Lett.*, 2024, **24**, 8752–8762.
24 J. Wang, S. Zhao, J. Chen, X. Liu, H. Chen, T. Lu, M. Xu, X. Guo, X. Shen and C. Liu, *ACS Appl. Mater. Interfaces*, 2023, **15**, 21904–21916.
25 M. Qi, S. Shan, B. Dong and L. Wang, in *Photofunctional Nanomaterials for Biomedical Applications*, 2025, pp. 449–476.
26 A. Bassam, M. Du, Y. Li and X. He, *Responsive Mater.*, 2025, **3**, e20240031.
27 S. T. Abedon, S. J. Kuhl, B. G. Blasdel and E. M. Kutter, *Bacteriophage*, 2011, **1**, 66–85.
28 S. A. Ranveer, V. Dasriya, M. F. Ahmad, H. S. Dhillon, M. Samtiya, E. Shama, T. Anand, T. Dhewa, V. Chaudhary and P. Chaudhary, *npj Sci. Food*, 2024, **8**, 1.
29 D. Turner, A. N. Shkoporov, C. Lood, A. D. Millard, B. E. Dutilh, P. Alfenas-Zerbini, L. J. Van Zyl, R. K. Aziz, H. M. Oksanen and M. M. Poranen, *Arch. Virol.*, 2023, **168**, 74.
30 H. M. Nguyen, S. Watanabe, S. Sharmin, T. Kawaguchi, X.-E. Tan, D. L. Wannigama and L. Cui, *Int. J. Mol. Sci.*, 2023, **24**, 17029.
31 M. Sanz-Gaitero, M. Seoane-Blanco and M. J. van Raaij, *Bacteriophages: Biology, technology, therapy*, 2021, pp. 19–91.
32 J. Böhning, M. Graham, S. C. Letham, L. K. Davis, U. Schulze, P. J. Stansfeld, R. A. Corey, P. Pearce, A. K. Tarafder and T. A. Bharat, *Nat. Commun.*, 2023, **14**, 8429.
33 V. B. Rao and J. Zhu, *Curr. Opin. Virol.*, 2022, **55**, 101255.
34 V. B. Rao and L. W. Black, *Virol. J.*, 2010, **7**, 1–14.
35 M. L. Yap and M. G. Rossmann, *Future Microbiol.*, 2014, **9**, 1319–1327.
36 F. L. Nobrega, M. Vlot, P. A. De Jonge, L. L. Dreesens, H. J. Beaumont, R. Lavigne, B. E. Dutilh and S. J. Brouns, *Nat. Rev. Microbiol.*, 2018, **16**, 760–773.
37 N. M. Taylor, N. S. Prokhorov, R. C. Guerrero-Ferreira, M. M. Shneider, C. Browning, K. N. Goldie, H. Stahlberg and P. G. Leiman, *Nature*, 2016, **533**, 346–352.
38 M. Dunne, N. S. Prokhorov, M. J. Loessner and P. G. Leiman, *Curr. Opin. Biotechnol.*, 2021, **68**, 272–281.
39 S. B. Santos, A. Oliveira, L. D. Melo and J. Azeredo, *Sci. Rep.*, 2019, **9**, 2568.
40 T. Ahmed, X. Xu, M. Noman, Q. Wang and B. Li, *Trends Biotechnol.*, 2024, **43**, 494–497.
41 D. Holtappels, P. Alfenas-Zerbini and B. Koskella, *FEMS Microbiol. Rev.*, 2023, **47**, fuad038.
42 X. Zhao, X. Zhong, S. Yang, J. Deng, K. Deng, Z. Huang, Y. Li, Z. Yin, Y. Liu and J. H. Viel, *Nat. Commun.*, 2024, **15**, 5287.
43 S. Dokuz, I. Coksu, S. Acar and T. Ozbek, *Biotechnol. J.*, 2025, **20**, 2300520.
44 J. Yan, X. Lyu, Y. Jiang, K. R. Ng, R. Yang, F. Zhang and W. Zhao, *ACS Appl. Mater. Interfaces*, 2023, **15**, 6514–6525.
45 S. P. Costa, C. L. Nogueira, A. P. Cunha, A. Lisac and C. M. Carvalho, *Crit. Rev. Biotechnol.*, 2023, **43**, 787–804.
46 G. F. Hatfull, R. M. Dedrick and R. T. Schooley, *Annu. Rev. Med.*, 2022, **73**, 197–211.
47 X. Chen, L. Lei, J. Yan, X. Wang, L. Li, Q. Liu, Y. Wang, T. Chen, J. Shao and L. Yu, *ACS Nano*, 2025, **19**, 6955–6976.
48 T. Briot, C. Kolenda, T. Ferry, M. Medina, F. Laurent, G. Leboucher, F. Pirot and P. S. Group, *J. Controlled Release*, 2022, **347**, 414–424.
49 X. T. Li, S. Y. Peng, S. M. Feng, T. Y. Bao, S. Z. Li and S. Y. Li, *Small*, 2024, **20**, 2307111.
50 L. Ngiam, M. A. Schembri, K. Weynberg and J. Guo, *Environ. Microbiol.*, 2021, **23**, 5569–5586.
51 D. Chae, *Transl. Clin. Pharmacol.*, 2023, **31**, 167.
52 C. L. Schneider, *Bacteriophages: Biology, technology, therapy*, 2017, pp. 1–42.
53 D. P. Pires, A. R. Costa, G. Pinto, L. Meneses and J. Azeredo, *FEMS Microbiol. Rev.*, 2020, **44**, 684–700.
54 T. Marks and R. Sharp, *J. Chem. Technol. Biotechnol.*, 2000, **75**, 6–17.
55 M. K. Kim, Q. Chen, A. Echterhof, N. Pennetzdorfer, R. C. McBride, N. Banaei, E. B. Burgener, C. E. Milla and P. L. Bollyky, *Nat. Commun.*, 2024, **15**, 9987.
56 F. Kunisch, C. Campobasso, J. Wagemans, S. Yildirim, B. K. Chan, C. Schaudinn, R. Lavigne, P. E. Turner, M. J. Raschke and A. Trampuz, *Nat. Commun.*, 2024, **15**, 8572.
57 C. Lood, P.-J. Haas, V. van Noort and R. Lavigne, *Curr. Opin. Virol.*, 2022, **52**, 236–243.
58 P. Jault, T. Leclerc, S. Jennes, J. P. Pirnay, Y.-A. Que, G. Resch, A. F. Rousseau, F. Ravat, H. Carsin and R. Le Floch, *Lancet Infect. Dis.*, 2019, **19**, 35–45.
59 L. Leitner, A. Ujmajuridze, N. Chanishvili, M. Goderdzishvili, I. Chkonia, S. Rigvava, A. Chkhotua, G. Changashvili, S. McCallin and M. P. Schneider, *Lancet Infect. Dis.*, 2021, **21**, 427–436.
60 I. Weiner, M. Kahan-Hanum, N. Buchstab, L. Zelcbuch, S. Navok, I. Sherman, J. Nicenboim, T. Axelrod, D. Berko-Ashur and M. Olshina, *Nat. Commun.*, 2025, **16**, 5579.

61 R. Nir-Paz, H. Onallah, M. Dekel, Y. N. Gellman, A. Haze, R. Ben-Ami, R. Braunstein, R. Hazan, D. Dror and Y. Oster, *Med*, 2025, **6**, 100565.
62 M. Mahler, A. R. Costa, S. P. van Beljouw, P. C. Fineran and S. J. Brouns, *Trends Biotechnol.*, 2023, **41**, 669–685.
63 H. Peng, I. A. Chen and U. Qimron, *Chem. Rev.*, 2024, **125**, 933–971.
64 K. Yehl, S. Lemire, A. C. Yang, H. Ando, M. Mimee, M. D. T. Torres, C. de la Fuente-Nunez and T. K. Lu, *Cell*, 2019, **179**, 459–469.
65 A. Eskenazi, C. Lood, J. Wubbolts, M. Hites, N. Balarjishvili, L. Leshkasheli, L. Askilashvili, L. Kvachadze, V. van Noort and J. Wagemans, *Nat. Commun.*, 2022, **13**, 302.
66 R. M. Dedrick, C. A. Guerrero-Bustamante, R. A. Garlena, D. A. Russell, K. Ford, K. Harris, K. C. Gilmour, J. Soothill, D. Jacobs-Sera and R. T. Schooley, *Nat. Med.*, 2019, **25**, 730–733.
67 Y. E. Gencay, D. Jasinskytė, C. Robert, S. Semsey, V. Martínez, A. Ø. Petersen, K. Brunner, A. de Santiago Torio, A. Salazar and I. C. Turcu, *Nat. Biotechnol.*, 2024, **42**, 265–274.
68 K. Kiga, X.-E. Tan, R. Ibarra-Chávez, S. Watanabe, Y. Aiba, Y. Sato'o, F.-Y. Li, T. Sasahara, B. Cui and M. Kawauchi, *Nat. Commun.*, 2020, **11**, 2934.
69 S. Meile, A. Sarbach, J. Du, M. Schuppler, C. Saez, M. J. Loessner and S. Kilcher, *Appl. Environ. Microbiol.*, 2020, **86**, e00442–e00420.
70 P. Kim, A. M. Sanchez, T. J. Penke, H. H. Tuson, J. C. Kime, R. W. McKee, W. L. Slone, N. R. Conley, L. J. McMillan and C. J. Prybol, *Lancet Infect. Dis.*, 2024, **24**, 1319–1332.
71 M. Gordon and P. Ramirez, *Antibiotics*, 2024, **13**, 125.
72 C. Ferriol-González and P. Domingo-Calap, *Antibiotics*, 2020, **9**, 268.
73 L. Khalifa, D. Gelman, M. Shlezinger, A. L. Dessal, S. Coppenhagen-Glazer, N. Beyth and R. Hazan, *Front. Microbiol.*, 2018, **9**, 326.
74 D. P. Pires, L. Meneses, A. C. Brandao and J. Azeredo, *Curr. Opin. Virol.*, 2022, **53**, 101209.
75 C. Pouget, C. Dunyach-Remy, A. Pantel, S. Schuldiner, A. Sotto and J.-P. Lavigne, *Microorganisms*, 2020, **8**, 1580.
76 N. M. Maurice, B. Bedi and R. T. Sadikot, *Am. J. Respir. Cell Mol. Biol.*, 2018, **58**, 428–439.
77 J. Onsea, P. Soentjens, S. Djebara, M. Merabishvili, M. Depypere, I. Spriet, P. De Munter, Y. Debaveye, S. Nijs and P. Vanderschot, *Viruses*, 2019, **11**, 891.
78 M. Popescu, J. D. Van Belleghem, A. Khosravi and P. L. Bollyky, *Annu. Rev. Virol.*, 2021, **8**, 415–435.
79 A. M. Pinto, M. D. Silva, L. M. Pastrana, M. Bañobre-López and S. Sillankorva, *FEMS Microbiol. Rev.*, 2021, **45**, fuab019.
80 O. Krut and I. Bekeredjian-Ding, *J. Immunol.*, 2018, **200**, 3037–3044.
81 H. Shuwen and D. Kefeng, *Gut Microbes*, 2022, **14**, 2113717.
82 D. J. Malik, H. Goncalves-Ribeiro, D. GoldSchmitt, J. Collin, A. Belkhiri, D. Fernandes, H. Weichert and A. Kirpichnikova, *Clin. Infect. Dis.*, 2023, **77**, S370–S383.
83 K. Li, Y. Chen, S. Li, H. G. Nguyen, Z. Niu, S. You, C. M. Mello, X. Lu and Q. Wang, *Bioconjugate Chem.*, 2010, **21**, 1369–1377.
84 X.-L. Hou, X.-T. Xie, L.-F. Tan, F. Zhang, J.-X. Fan, W. Chen, Y.-G. Hu, Y.-D. Zhao, B. Liu and Q.-R. Xu, *ACS Mater. Lett.*, 2023, **5**, 2270–2281.
85 J. Yang, F. Lin, T. Ma, L. Gao, B. Wang, S. Tan, X. Xu and Z.-q. Yang, *Microchim. Acta*, 2024, **191**, 566.
86 F. Wang, S. Chen, Y. Xia, C. Liu, Z. Xu, R. Song, W. Liu, T. Liu, G. Chen and Q. Liu, *ACS Appl. Mater. Interfaces*, 2024, **17**, 419–429.
87 C. Huang, J. Zhao, R. Lu, J. Wang, S. R. Nugen, Y. Chen and X. Wang, *Food Chem.*, 2023, **400**, 134035.
88 J. H. Shin, T. J. Park, M. S. Hyun and J. P. Park, *Food Chem.*, 2022, **378**, 132061.
89 B. Ran, Y. Yuan, W. Xia, M. Li, Q. Yao, Z. Wang, L. Wang, X. Li, Y. Xu and X. Peng, *Chem. Sci.*, 2021, **12**, 1054–1061.
90 L.-L. Li, P. Yu, X. Wang, S.-S. Yu, J. Mathieu, H.-Q. Yu and P. J. Alvarez, *Environ. Sci.: Nano*, 2017, **4**, 1817–1826.
91 L. Dong, B. Zhao, Y. Lu, L. Li, C. Huang, X. Zhou, T. You, W. Qian, J. Zhang and G. Luo, *J. Controlled Release*, 2025, **382**, 113708.
92 H. Peng, R. E. Borg, L. P. Dow, B. L. Pruitt and I. A. Chen, *Proc. Natl. Acad. Sci. U. S. A.*, 2020, **117**, 1951–1961.
93 H. Peng, D. Rossetto, S. S. Mansy, M. C. Jordan, K. P. Roos and I. A. Chen, *ACS Nano*, 2022, **16**, 4756–4774.
94 H. Peng, R. E. Borg, A. B. Nguyen and I. A. Chen, *ACS Sens.*, 2020, **5**, 1491–1499.
95 L. Bi, H. Zhang, W. Hu, J. Chen, Y. Wu, H. Chen, B. Li, Z. Zhang, J. Choo and L. Chen, *Biosens. Bioelectron.*, 2023, **237**, 115519.
96 H. Fang, S. Zhan, L. Feng, X. Chen, Q. Guo, Y. Guo, Q. He and Y. Xiong, *Sens. Actuators, B*, 2021, **346**, 130368.
97 Z. Wei, X. Wei, C. Zhao, H. Zhang and Z. Zhang, *ACS Omega*, 2022, **7**, 9951–9957.
98 D.-W. Zheng, X. Dong, P. Pan, K.-W. Chen, J.-X. Fan, S.-X. Cheng and X.-Z. Zhang, *Nat. Biomed. Eng.*, 2019, **3**, 717–728.
99 H. S. Zurier, M. M. Duong, J. M. Goddard and S. R. Nugen, *ACS Appl. Bio Mater.*, 2020, **3**, 5824–5831.
100 H. Ahmed, H. Lopez, F. Boselli, G. Tarricone, S. Vercellino, P. E. Costantini, V. Castagnola, M. Veronesi, F. Benfenati and A. Danielli, *ACS Nano*, 2024, **18**, 21302–21315.
101 X. Meng, Z. Xu, C. Wang, J. Patitz, A. R. Boccaccini, A. Burkovski and K. Zheng, *Colloids Surf., B*, 2024, **234**, 113714.
102 A. B. Zavala-Martínez and E. Grelet, *ACS Nano*, 2023, **18**, 281–287.
103 S. Lin, G. Xie, J. He, L. Meng, Y. Pang and J. Liu, *Nat. Biomed. Eng.*, 2025, **9**, 1155–1171.
104 A. Sati, T. N. Ranade, S. N. Mali, H. K. Ahmad Yasin and A. Pratap, *ACS Omega*, 2025, **10**, 7549–7582.

105 J. M. Carvalho-Silva, I. Ferreira, L. M. Uehara and A. C. dos Reis, *Future Virol.*, 2025, **20**, 19–26.
106 Y. Jian, X. Chen, T. Ahmed, Q. Shang, S. Zhang, Z. Ma and Y. Yin, *J. Adv. Res.*, 2022, **38**, 1–12.
107 S. A. Alobaid, S. Shrestha, M. Tasseff, B. Wang, M. L. van Hoek and P. K. Dutta, *Discover Nano*, 2025, **20**, 26.
108 K. Vadakkan, N. P. Rumjit, A. K. Ngangbam, S. Vijayanand and N. K. Nedumpillil, *Coord. Chem. Rev.*, 2024, **499**, 215528.
109 H. Zhao, Y. Wang, L. Bao and C. Chen, *Acc. Mater. Res.*, 2022, **3**, 812–829.
110 K. Skrzyniarz, J. Sanchez-Nieves, F. J. de la Mata, M. Łysek-Gładysińska, K. Lach and K. Ciepluch, *Int. J. Biol. Macromol.*, 2023, **237**, 124239.
111 Z.-y. Zhao, P.-j. Li, R.-s. Xie, X.-y. Cao, D.-l. Su and Y. Shan, *Int. J. Biol. Macromol.*, 2022, **214**, 220–229.
112 T. Parandhaman, P. Choudhary, B. Ramalingam, M. Schmidt, S. Janardhanam and S. K. Das, *ACS Biomater. Sci. Eng.*, 2021, **7**, 5899–5917.
113 D. Rutherford, K. Kolářová, J. Čech, P. Haušild, J. Kuličeк, E. Ukraintsev, Š. Stehlík, R. Dao, J. Neuman and B. Rezek, *Ultramicroscopy*, 2024, **258**, 113909.
114 S. Tang and J. Zheng, *Adv. Healthcare Mater.*, 2018, **7**, 1701503.
115 M. Arribas Perez, O. H. Moriones, N. G. Bastús, V. Puntes, A. Nelson and P. A. Beales, *Biochemistry*, 2019, **58**, 4761–4773.
116 B.-H. Mao, J.-C. Tsai, C.-W. Chen, S.-J. Yan and Y.-J. Wang, *Nanotoxicology*, 2016, **10**, 1021–1040.
117 J. Liu, H. Zhang, L. Yan, P. G. Kerr, S. Zhang and Y. Wu, *J. Hazard. Mater.*, 2021, **401**, 123809.
118 D. He, C. J. Miller and T. D. Waite, *J. Catal.*, 2014, **317**, 198–205.
119 D. He, S. Garg and T. D. Waite, *Langmuir*, 2012, **28**, 10266–10275.
120 A. Roy, O. Bulut, S. Some, A. K. Mandal and M. D. Yilmaz, *RSC Adv.*, 2019, **9**, 2673–2702.
121 S. Mukherji, J. Ruparelia and S. Agnihotri, in *Nano-antimicrobials: Progress and prospects*, Springer, 2011, pp. 225–251.
122 T. Dairaku, R. Kawai, T. Kanaba, T. Ono, K. Yoshida, H. Sato, K. Nozawa-Kumada, Y. Kondo, J. Kondo and A. Ono, *Dalton Trans.*, 2021, **50**, 7633–7639.
123 C. Arrault, Y. R. Monneau, M. Martin, F.-X. Cantrelle, E. Boll, F. Chirot, C. C. Zerbino, O. Walker and M. Hologne, *J. Biol. Chem.*, 2023, **299**, 105004.
124 F. Kang, P. J. Alvarez and D. Zhu, *Environ. Sci. Technol.*, 2014, **48**, 316–322.
125 L. M. Stabryla, K. A. Johnston, N. A. Diemler, V. S. Cooper, J. E. Millstone, S.-J. Haig and L. M. Gilbertson, *Nat. Nanotechnol.*, 2021, **16**, 996–1003.
126 G. Tortella, O. Rubilar, N. Durán, M. Diez, M. Martínez, J. Parada and A. Seabra, *J. Hazard. Mater.*, 2020, **390**, 121974.
127 Y. Bian, K. Kim, T. Ngo, I. Kim, O.-N. Bae, K.-M. Lim and J.-H. Chung, *Part. Fibre Toxicol.*, 2019, **16**, 1–14.
128 S. Manoharadas, M. Altaf, A. F. Alrefaei, R. M. Devasia, A. Y. M. Badjah Hadj and M. S. A. Abuhasil, *RSC Adv.*, 2021, **11**, 1420–1429.
129 A. S. Abdelsattar, R. Nofal, S. Makky, A. Safwat, A. Taha and A. El-Shibiny, *Antibiotics*, 2021, **10**, 678.
130 M. Szymczak and P. Golec, *Int. J. Nanomed.*, 2024, **19**, 10097–10105.
131 B. Ahmed, F. Ameen, A. Rizvi, K. Ali, H. Sonbol, A. Zaidi, M. S. Khan and J. Musarrat, *ACS Omega*, 2020, **5**, 7861–7876.
132 Q. Zhang, H. Zhou, P. Jiang, L. Wu and X. Xiao, *J. Hazard. Mater.*, 2024, **469**, 133942.
133 E. Gilcrease, R. Williams and R. Goel, *Water Res.*, 2020, **181**, 115900.
134 M. Szymczak, J. A. Pankowski, A. Kwiatek, B. Grygorcewicz, J. Karczewska-Golec, K. Sadowska and P. Golec, *Sci. Rep.*, 2024, **14**, 9088.
135 A. S. Abdelsattar, T. A. Hakim, N. Rezk, W. M. Farouk, Y. Y. Hassan, S. M. Gouda and A. El-Shibiny, *J. Inorg. Organomet. Polym. Mater.*, 2022, **32**, 1951–1965.
136 M. M. Elsayed, R. M. Elkenany, A. I. Zakari and B. M. Badawy, *BMC Microbiol.*, 2023, **23**, 146.
137 T. Yang, N. Li, X. Wang, J. Zhai, B. Hu, M. Chen and J. Wang, *Chin. Chem. Lett.*, 2020, **31**, 145–149.
138 J. Gong, Q. Ding, Y. Shi, M. Li, C. Liu, W. Zeng, J. Kim, S. Shan, W. Zhang and M. Qi, *Coord. Chem. Rev.*, 2025, **526**, 216348.
139 Y. Hang, A. Wang and N. Wu, *Chem. Soc. Rev.*, 2024, **53**, 2932–2971.
140 W. Zheng, Y. Jia, Y. Zhao, J. Zhang, Y. Xie, L. Wang, X. Zhao, X. Liu, R. Tang, W. Chen and X. Jiang, *Nano Lett.*, 2021, **21**, 1992–2000.
141 Y. Gong, D. Wu, X. Yan, Q. Zhang, W. Zheng, B. Li, H. Chen and L. Wang, *Anal. Chem.*, 2024, **96**, 18865–18872.
142 H. Lee and D. G. Lee, *Colloids Surf., B*, 2018, **167**, 1–7.
143 K. Zheng, M. I. Setyawati, D. T. Leong and J. Xie, *Bioact. Mater.*, 2021, **6**, 941–950.
144 A. Gopal, L. Yan, S. Kashif, T. Munshi, V. A. Roy, N. H. Voelcker and X. Chen, *Adv. Healthcare Mater.*, 2022, **11**, 2101546.
145 J. Du, Z. Yu, Z. Hu, J. Chen, J. Zhao and Y. Bai, *J. Microbiol. Methods*, 2021, **180**, 106110.
146 P. Ge, J. Zhang, T. Ding and Y. Xianyu, *ACS Mater. Lett.*, 2023, **5**, 638–655.
147 L. Liu, T. Zhang, Z. Wu, F. Zhang, Y. Wang, X. Wang, Z. Zhang, C. Li, X. Lv and D. Chen, *Anal. Chem.*, 2023, **95**, 4050–4058.
148 X. Zhao, H. Tang and X. Jiang, *ACS Nano*, 2022, **16**, 10066–10087.
149 C. M. Silvero, D. M. Rocca, E. A. de la Villarmois, K. Fournier, A. E. Lanterna, M. F. Perez, M. C. Becerra and J. C. Scaiano, *ACS Omega*, 2018, **3**, 1220–1230.
150 Y. Chen, Y. Xianyu and X. Jiang, *Acc. Chem. Res.*, 2017, **50**, 310–319.
151 A. Timoszyk and R. Grochowalska, *Pharmaceutics*, 2022, **14**, 2599.

152 K. U. Suganya, K. Govindaraju, V. G. Kumar, T. S. Dhas, V. Karthick, G. Singaravelu and M. Elanchezhiyan, *Mater. Sci. Eng., C*, 2015, **47**, 351–356.
153 W. Q. Chen, W. J. Wu, Y. Q. Yu, Y. Liu and F. L. Jiang, *Langmuir*, 2023, **39**, 9595–9603.
154 A. Chahardoli, N. Karimi, F. Sadeghi and A. Fattahi, *Artif. Cells, Nanomed., Biotechnol.*, 2018, **46**, 579–588.
155 Y. Cui, Y. Zhao, Y. Tian, W. Zhang, X. Lü and X. Jiang, *Biomaterials*, 2012, **33**, 2327–2333.
156 A. Biswas, N. Lemcoff and Y. Weizmann, *Acc. Chem. Res.*, 2025, 8054–8057.
157 J. Huo, Q. Jia, H. Huang, J. Zhang, P. Li, X. Dong and W. Huang, *Chem. Soc. Rev.*, 2021, **50**, 8762–8789.
158 S. Huang, M. Qi and Y. Chen, *Front. Microbiol.*, 2023, **14**, 948092.
159 B. Zhou, B. Dong, S. Hu, W. Liu, L. Sun, L. Xu, X. Bai, L. Wang, M. Qi and H. Song, *Small*, 2024, **20**, e2310706.
160 M. Qi, X. Ren, W. Li, Y. Sun, X. Sun, C. Li, S. Yu, L. Xu, Y. Zhou and S. Song, *Nano Today*, 2022, **43**, 101447.
161 T. T. Ngo-Duc, Z. Alibay, J. M. Plank, J. E. Cheeney and E. D. Haberer, *ACS Appl. Mater. Interfaces*, 2020, **12**, 126–134.
162 D. Yadav, S. Sankaranarayanan, A. Thanekar and A. Rengan, *Mater. Today Nano*, 2023, **23**, 100348.
163 Z. Zeng, Z. Hu, R. Zhao, J. Rao, M. R. Mestre, Y. Liu, S. Liu, H. Feng, Y. Chen and H. He, *Science*, 2025, **388**, eads6055.
164 L. Richter, K. Paszkowska, U. Cendrowska, F. Olgiati, P. J. Silva, M. Gasbarri, Z. P. Guven, J. Paczesny and F. Stellacci, *Nanoscale*, 2021, **13**, 18684–18694.
165 X. Wang, T. Yang and Q. Li, *Responsive Mater.*, 2024, **2**, e20240027.
166 Z. Yang and L. Zhang, *Adv. Intell. Syst.*, 2020, **2**, 2000082.
167 X. Ma, L. Wang, P. Wang, Z. Liu, J. Hao, J. Wu, G. Chu, M. Huang, L. O. Mair and C. Huang, *Chem. Eng. J.*, 2022, **431**, 133971.
168 L. Lu, Y. Liu, X. Chen, F. Xu, Q. Zhang, Z. Yin and L. Yuwen, *Nanomaterials*, 2024, **14**, 1830.
169 Z. Li, J. Ma, J. Ruan and X. Zhuang, *Nanoscale Res. Lett.*, 2019, **14**, 1–8.
170 F. Chen, S. Xie, X. Huang and X. Qiu, *J. Hazard. Mater.*, 2017, **322**, 152–162.
171 S. Kaushik, J. Thomas, V. Panwar, P. Murugesan, V. Chopra, N. Salaria, R. Singh, H. S. Roy, R. Kumar and V. Gautam, *Nanoscale*, 2022, **14**, 1713–1722.
172 A. Basu, M. R. Clary, J. B. Tracy, C. K. Hall and O. D. Velev, *ACS Nano*, 2024, **18**, 19814–19827.
173 K. Quan, G. Jiang, J. Liu, Z. Zhang, Y. Ren, H. J. Busscher, H. C. Van Der Mei and B. W. Peterson, *Nanoscale*, 2021, **13**, 4644–4653.
174 P. Zhang, H. Yang, M. T. Ahmad, Q. Zheng, G. Nie, A. Ahmad, M. Raza and S. Raza, *Curr. Microbiol.*, 2025, **82**, 1–10.
175 P. Yu, Z. Wang, M. Marcos-Hernandez, P. Zuo, D. Zhang, C. Powell, A. Y. Pan, D. Villagrán, M. S. Wong and P. J. Alvarez, *Environ. Sci.: Nano*, 2019, **6**, 3539–3550.
176 B.-H. Mao, Y.-K. Luo, B.-J. Wang, C.-W. Chen, F.-Y. Cheng, Y.-H. Lee, S.-J. Yan and Y.-J. Wang, *Part. Fibre Toxicol.*, 2022, **19**, 6.
177 Y. Pan, A. Leifert, D. Ruau, S. Neuss, J. Bornemann, G. Schmid, W. Brandau, U. Simon and W. Jahnen-Dechent, *Small*, 2009, **5**, 2067–2076.
178 Y.-P. Jia, B.-Y. Ma, X.-W. Wei and Z.-Y. Qian, *Chin. Chem. Lett.*, 2017, **28**, 691–702.
179 A. Sani, C. Cao and D. Cui, *Biochem. Biophys. Rep.*, 2021, **26**, 100991.
180 G. Liu, J. Gao, H. Ai and X. Chen, *Small*, 2013, **9**, 1533–1545.
181 B. Shahare, M. Yashpal and Gajendra, *Toxicol. Mech. Methods*, 2013, **23**, 161–167.
182 E.-J. Park, E. Bae, J. Yi, Y. Kim, K. Choi, S. H. Lee, J. Yoon, B. C. Lee and K. Park, *Environ. Toxicol. Pharmacol.*, 2010, **30**, 162–168.
183 Y. S. Kim, J. S. Kim, H. S. Cho, D. S. Rha, J. M. Kim, J. D. Park, B. S. Choi, R. Lim, H. K. Chang and Y. H. Chung, *Inhalation Toxicol.*, 2008, **20**, 575–583.
184 R. Peterson, L. Jensen and P. Harrison, *Avian Dis.*, 1973, 802–806.
185 R. R. R. Sardari, S. R. Zarchi, A. Talebi, S. Nasri, S. Imani, A. Khoradmehr and S. A. R. Sheshde, *Afr. J. Microbiol. Res.*, 2012, **6**, 5587–5593.
186 N. Hadrup, K. Loeschner, A. Mortensen, A. K. Sharma, K. Qvortrup, E. H. Larsen and H. R. Lam, *Neurotoxicology*, 2012, **33**, 416–423.
187 S. O. Tamimi, S. M. Zmeili, M. N. Gharaibeh, M. S. Shubair and A. S. Salhab, *J. Toxicol. Environ. Health, Part A*, 1998, **53**, 47–60.
188 C. Greulich, D. Braun, A. Peetsch, J. Diendorf, B. Siebers, M. Epple and M. Köller, *RSC Adv.*, 2012, **2**, 6981–6987.
189 S. Hackenberg, A. Scherzed, M. Kessler, S. Hummel, A. Technau, K. Froelich, C. Ginzkey, C. Koehler, R. Hagen and N. Kleinsasser, *Toxicol. Lett.*, 2011, **201**, 27–33.
190 A. R. Gliga, S. Skoglund, I. Odnevall Wallinder, B. Fadeel and H. L. Karlsson, *Part. Fibre Toxicol.*, 2014, **11**, 11.
191 J. Sengupta, P. Datta, H. Patra, A. K. Dasgupta and A. Gomes, *J. Nanosci. Nanotechnol.*, 2013, **13**, 1660–1670.
192 C. Yang, A. Tian and Z. Li, *Sci. Rep.*, 2016, **6**, 20203.
193 H. A. Khan, M. A. K. Abdelhalim, M. S. Al-Ayed and A. S. Alhomida, *Saudi J. Biol. Sci.*, 2012, **19**, 461–464.
194 Y.-S. Chen, Y.-C. Hung, I. Liau and G. S. Huang, *Nanoscale Res. Lett.*, 2009, **4**, 858.
195 M. C. Senut, Y. Zhang, F. Liu, A. Sen, D. M. Ruden and G. Mao, *Small*, 2016, **12**, 631–646.
196 M. Yao, L. He, D. J. McClements and H. Xiao, *J. Agric. Food Chem.*, 2015, **63**, 8044–8049.
197 M. Enea, E. Pereira, M. Peixoto de Almeida, A. M. Araújo, M. d. L. Bastos and H. Carmo, *Nanomaterials*, 2020, **10**, 995.
198 S. Zhao, X. Lin, L. Zhang, L. Sun, J. Li, W. Yang and Z. Sun, *Biomed. Eng.: Appl., Basis Commun.*, 2012, **24**, 229–235.
199 L. Gu, R. H. Fang, M. J. Sailor and J.-H. Park, *ACS Nano*, 2012, **6**, 4947–4954.

200 L. Sadeghi and H. Espanani, *Bratisl. Lek. Listy*, 2015, **116**, 373–378.
201 Q. Ran, Y. Xiang, Y. Liu, L. Xiang, F. Li, X. Deng, Y. Xiao, L. Chen, L. Chen and Z. Li, *Sci. Rep.*, 2015, **5**, 16209.
202 C. C. Berry, S. Wells, S. Charles and A. S. Curtis, *Biomaterials*, 2003, **24**, 4551–4557.
203 E. Pawelczyk, A. S. Arbab, A. Chaudhry, A. Balakumaran, P. G. Robey and J. A. Frank, *Stem Cells*, 2008, **26**, 1366–1375.
204 S. Correia Carreira, L. Walker, K. Paul and M. Saunders, *Nanotoxicology*, 2015, **9**, 66–78.
205 M. Mahmoudi, S. Laurent, M. A. Shokrgozar and M. Hosseinkhani, *ACS Nano*, 2011, **5**, 7263–7276.
206 S. A. Sankaranarayanan, D. N. Yadav, S. Yadav, A. Srivastava, S. R. Pramatha, V. R. Kotagiri, H. Joshi and A. K. Rengan, *Langmuir*, 2024, **40**, 16743–16756.
207 L. Chen, M. Y. Wu, S. L. Chen, R. Hu, Y. Wang, W. Zeng, S. Feng, M. Ke, L. Wang and S. Chen, *Adv. Mater.*, 2024, **36**, 2407268.
208 X. He, Y. Yang, Y. Guo, S. Lu, Y. Du, J.-J. Li, X. Zhang, N. L. Leung, Z. Zhao and G. Niu, *J. Am. Chem. Soc.*, 2020, **142**, 3959–3969.
209 J. Zhang, X. He and B. Z. Tang, *ACS Nano*, 2024, **18**, 3199–3213.
210 M. Y. Wu, L. Chen, Q. Chen, R. Hu, X. Xu, Y. Wang, J. Li, S. Feng, C. Dong and X. L. Zhang, *Adv. Mater.*, 2023, **35**, 2208578.
211 B. Hong, T. Qin, W. Wang, Y. Li, Y. Ma and J. Wang, *Talanta*, 2024, **276**, 126268.
212 H. Peng and I. A. Chen, *ACS Nano*, 2019, **13**, 1244–1252.
213 T. Z. Mehrizi, M. Mirzaei and M. S. Ardestani, *Curr. Pharm. Biotechnol.*, 2024, **25**, 247–267.
214 K. P. Kim, J. D. Cha, E. H. Jang, J. Klumpp, S. Hagens, W. D. Hardt, K. Y. Lee and M. J. Loessner, *Microb. Biotechnol.*, 2008, **1**, 247–257.
215 H. R. Temsaah, K. Abdelkader, A. E. Ahmed, N. Elgiddawy, Z. E. Eldin, H. A. Elshebrawy, N. G. Kasem, F. A. El-Gohary and A. F. Azmy, *BMC Biotechnol.*, 2025, **25**, 3.
216 R. Jamaledin, R. Sartorius, C. Di Natale, R. Vecchione, P. De Berardinis and P. A. Netti, *Microorganisms*, 2020, **8**, 650.
217 S. Chhibber, J. Kaur and S. Kaur, *Front. Microbiol.*, 2018, **9**, 561.
218 H. Bai, Q. Borjihan, Z. Li, P. Qin, J. Cheng, D. Xiao and A. Dong, *Eur. J. Pharm. Biopharm.*, 2024, 114258.
219 G. Francius, M. Cervulle, E. Clément, X. Bellanger, S. Ekrami, C. Gantzer and J. F. Duval, *ACS Appl. Bio Mater.*, 2021, **4**, 2614–2627.
220 K. Z. Wu, Z. Le, B. Myint, B. Chan, L. Liu, H. Huang, S. L. Sing and A. Tay, *Mater. Today Bio*, 2024, 101022.
221 L. Wang, X. Fan, M. Gonzalez Moreno, T. Tkhilaishvili, W. Du, X. Zhang, C. Nie, A. Trampuz and R. Haag, *Adv. Sci.*, 2022, **9**, 2105668.
222 H. Li, B. Li, D. Lv, W. Li, Y. Lu and G. Luo, *Adv. Drug Delivery Rev.*, 2023, **196**, 114778.
223 L. Jin, F. Cao, Y. Gao, C. Zhang, Z. Qian, J. Zhang and Z. Mao, *Adv. Mater.*, 2023, **35**, 2301349.
224 L. Wang, Y. Mai, J. Zhang, C. Ruan, J. Hu, K. Ye, Y. He, D. Wang, L. Jin and Z. Mao, *Chem. Eng. J.*, 2025, **505**, 159666.
225 H.-Y. Shen, Z.-H. Liu, J.-S. Hong, M.-S. Wu, S.-J. Shiue and H.-Y. Lin, *J. Controlled Release*, 2021, **331**, 154–163.
226 J. Park, M. A. Hassan, A. Nabawy, C. H. Li, M. Jiang, K. Parmar, A. Reddivari, R. Goswami, T. Jeon and R. Patel, *ACS Nano*, 2024, **18**, 26928–26936.
227 H. Y. Kim, R. Y. K. Chang, S. Morales and H.-K. Chan, *Antibiotics*, 2021, **10**, 130.
228 W. Sun, J. Xu, B. Liu, Y.-D. Zhao, L. Yu and W. Chen, *Nanotechnology*, 2022, **33**, 165102.
229 Z. Wu, B. Chan, J. Low, J. J. H. Chu, H. W. D. Hey and A. Tay, *Bioact. Mater.*, 2022, **16**, 249–270.
230 C. R. Arciola, D. Campoccia and L. Montanaro, *Nat. Rev. Microbiol.*, 2018, **16**, 397–409.
231 L. Wang, T. Tkhilaishvili, Z. Jiang, R. F. Pirlar, Y. Ning, A. M. Laleona, J. Wang, J. Tang, Q. Wang and A. Trampuz, *J. Controlled Release*, 2024, **376**, 949–960.
232 J. A. R. Barros, L. D. R. de Melo, R. A. R. da Silva, M. P. Ferraz, J. C. V. de Rodrigues Azeredo, V. M. de Carvalho Pinheiro, B. J. A. Colaço, M. H. R. Fernandes, P. de Sousa Gomes and F. J. Monteiro, *Nanomedicine*, 2020, **24**, 102145.
233 V. S. Gondil, M. Ashcraft, S. Ghalei, A. Kumar, S. N. Wilson, R. Devine, H. Handa and E. J. Brisbois, *ACS Appl. Bio Mater.*, 2025, **8**, 1362–1376.
234 C. Cao, M. Yu and Y. Chai, *Cell Death Dis.*, 2019, **10**, 782.
235 C. Fleischmann-Struzek, L. Mellhammar, N. Rose, A. Cassini, K. Rudd, P. Schlattmann, B. Allegranzi and K. Reinhart, *Intensive Care Med.*, 2020, **46**, 1552–1562.
236 P. Jin, L. Wang, R. Sha, L. Liu, J. Qian, N. Ishimwe, W. Zhang, J. Qian, Y. Zhang and L. Wen, *Theranostics*, 2021, **11**, 2278.
237 T. Ozbek, H. Demir, S. Dokuz, S. Tasdurmazli, U. Ozbey, M. Ozbil, M. Topuzogullari, I. Cinar, M. Karamese and S. A. Karamese, *J. Controlled Release*, 2025, **380**, 773–786.
238 N. Wang and J.-Y. Fang, *Trends Microbiol.*, 2023, **31**, 159–172.
239 H. Zhu, M. Li, D. Bi, H. Yang, Y. Gao, F. Song, J. Zheng, R. Xie, Y. Zhang and H. Liu, *Nat. Commun.*, 2024, **15**, 1688.
240 B. Roje, B. Zhang, E. Mastrorilli, A. Kovačić, L. Sušak, I. Ljubenkov, E. Ćosić, K. Vilović, A. Meštrović and E. L. Vukovac, *Nature*, 2024, **632**, 1137–1144.
241 J.-W. Zhang, D. Zhang, H.-S. Yin, H. Zhang, K.-Q. Hong, J.-P. Yuan and B.-P. Yu, *Gut Microbes*, 2023, **15**, 2197836.
242 J. Lu, W. Wei and D. Zheng, *Research*, 2025, **8**, 0640.
243 X. Dong, P. Pan, D.-W. Zheng, P. Bao, X. Zeng and X.-Z. Zhang, *Sci. Adv.*, 2020, **6**, eaba1590.
244 D. M. Warner and A. H. Mehta, *Gut Microbiome*, 2024, **5**, e9.
245 Y. Zhao, M. Zhu, Y. Ling, Y. Zhao, X. Lu, B. Chu, Y. He and H. Wang, *Adv. Mater.*, 2025, **37**, 2417334.
246 M. Assefa, *Pneumonia*, 2022, **14**, 4.
247 M. Besser, J. Terberger, L. Weber, B. Ghebremedhin, E. Naumova, W. Arnold and E. Stuermer, *J. Transl. Med.*, 2019, **17**, 243.

248 H. Rath, S. N. Stumpp and M. Stiesch, *PLoS One*, 2017, **12**, e0172095.
249 P. F. Duckworth, R. S. Rowlands, M. E. Barbour and S. E. Maddocks, *Microbiol. Res.*, 2018, **215**, 141–147.
250 S. A. Gomez-Ochoa, M. Pitton, L. G. Valente, C. D. Sosa Vesga, J. Largo, A. C. Quiroga-Centeno, J. A. Hernandez Vargas, S. J. Trujillo-Caceres, T. Muka, D. R. Cameron and Y. A. Que, *Lancet Microbe*, 2022, **3**, e956–e968.
251 S. Uyttebroek, B. Chen, J. Onsea, F. Ruythooren, Y. Debaveye, D. Devolder, I. Spriet, M. Depypere, J. Wagemans, R. Lavigne, J. P. Pirnay, M. Merabishvili, P. De Munter, W. E. Peetermans, L. Dupont, L. Van Gerven and W. J. Metsemakers, *Lancet Infect. Dis.*, 2022, **22**, e208–e220.
252 A. Petrovic Fabijan, R. C. Lin, J. Ho, S. Maddocks, N. L. Ben Zakour, J. R. Iredell and Westmead Bacteriophage Therapy Team, *Nat. Microbiol.*, 2020, **5**, 465–472.
253 J.-P. Pirnay, S. Djebara, G. Steurs, J. Griselain, C. Cochez, S. De Soir, T. Glonti, A. Spiessens, E. Vanden Berghe and S. Green, *Nat. Microbiol.*, 2024, **9**, 1434–1453.
254 M. Bernabéu-Gimeno, M. Pardo-Freire, B. K. Chan, P. E. Turner, A. Gil-Brusola, S. Pérez-Tarazona, L. Carrasco-Hernández, E. Quintana-Gallego and P. Domingo-Calap, *Med*, 2024, **5**, 1096–1111.
255 Q. Yang, S. Le, T. Zhu and N. Wu, *Front. Microbiol.*, 2023, **14**, 1250848.
256 T. Faltus, *Viruses*, 2024, **16**, 443.
257 L. Bretaudeau, K. Tremblais, F. Aubrit, M. Meichenin and I. Arnaud, *Front. Microbiol.*, 2020, **11**, 1161.
258 M. Suleman, J. R. Clark, S. Bull and J. D. Jones, *J. Med. Ethics*, 2025, **51**, 298–302.
259 M. Cafora, N. Poerio, F. Forti, N. Loberto, D. Pin, R. Bassi, M. Aureli, F. Briani, A. Pistocchi and M. Fraziano, *Front. Microbiol.*, 2022, **13**, 979610.
260 N. A. Lerminiaux and A. D. Cameron, *Can. J. Microbiol.*, 2019, **65**, 34–44.
261 X. Xiao, X.-L. Ma, X. Han, L.-J. Wu, C. Liu and H.-Q. Yu, *Sci. Total Environ.*, 2021, **760**, 144040.
262 X. Han, P. Lv, L.-G. Wang, F. Long, X.-L. Ma, C. Liu, Y.-J. Feng, M.-F. Yang and X. Xiao, *Environ. Sci.: Nano*, 2020, **7**, 1214–1224.
263 J. Lu, Y. Wang, M. Jin, Z. Yuan, P. Bond and J. Guo, *Water Res.*, 2020, **169**, 115229.
264 S. Zhang, Y. Wang, H. Song, J. Lu, Z. Yuan and J. Guo, *Environ. Int.*, 2019, **129**, 478–487.
265 D. I. Andersson and D. Hughes, *Microbiol. Spectrum*, 2017, **5**, 1–17.
266 H. Zhou, J. F. Beltrán and I. L. Brito, *Sci. Adv.*, 2021, **7**, eabj5056.
267 D. Lund, M. Parras-Moltó, J. S. Inda-Díaz, S. Ebmeyer, D. J. Larsson, A. Johnning and E. Kristiansson, *Nat. Commun.*, 2025, **16**, 2595.
268 J. Fang, Y. Wan, Y. Sun, X. Sun, M. Qi, S. Cheng, C. Li, Y. Zhou, L. Xu and B. Dong, *Chem. Eng. J.*, 2022, **435**, 134935.
269 X. Zhou, Z. Wang, Y. K. Chan, Y. Yang, Z. Jiao, L. Li, J. Li, K. Liang and Y. Deng, *Adv. Funct. Mater.*, 2022, **32**, 2109469.
270 M. Wang, J. Pu, Y. Hu, Y. Zi, Z. G. Wu and W. Huang, *Adv. Funct. Mater.*, 2024, **34**, 2308601.
271 J. Chen, Q. Ma, M. Li, D. Chao, L. Huang, W. Wu, Y. Fang and S. Dong, *Nat. Commun.*, 2021, **12**, 3375.
272 H. Zhong, C. Jiang and Y. Huang, *RSC Adv.*, 2023, **13**, 1539–1550.
273 H.-Y. Kwon, Y. Jung, H. Jeon and H.-S. Han, *Bioact. Mater.*, 2025, **48**, 71–99.
274 Y. Wang, C. Li, Y. Wan, M. Qi, Q. Chen, Y. Sun, X. Sun, J. Fang, L. Fu and L. Xu, *Small*, 2021, **17**, 2101505.
275 S. Liang, M.-H. Li, M.-L. Qi, H. Hui, H.-P. Zhang, J. Zhou, L. Wang and Y.-W. Yang, *Nano Lett.*, 2024, **24**, 13708–13717.
276 T. D. Doan, N.-N. Vu, T. L. G. Hoang and P. Nguyen-Tri, *Coord. Chem. Rev.*, 2025, **523**, 216298.
277 Y. Zhu, P. Xu, X. Zhang and D. Wu, *Chem. Soc. Rev.*, 2022, **51**, 1377–1414.
278 N. Deirram, C. Zhang, S. S. Kermaniyan, A. P. Johnston and G. K. Such, *Macromol. Rapid Commun.*, 2019, **40**, 1800917.
279 S. Wang, S. Tavakoli, R. P. Parvathaneni, G. N. Nawale, O. P. Oommen, J. Hilborn and O. P. Varghese, *Biomater. Sci.*, 2022, **10**, 6399–6412.
280 S. Ulrich, *Acc. Chem. Res.*, 2019, **52**, 510–519.
281 W. Zhao, Q. Ding, B. Zhou, J. Liu, Y. Shi, C. Liu, C. Li, B. Dong, M. Qi and J. S. Kim, *Adv. Funct. Mater.*, 2024, **34**, 2407626.
282 G. Xuan, H. Lin, L. Tan, G. Zhao and J. Wang, *MBio*, 2022, **13**, e03174–e03121.
283 A. C. Duarte, L. Fernández, A. Jurado, A. B. Campelo, Y. Shen, A. Rodríguez and P. García, *Front. Microbiol.*, 2024, **15**, 1438022.
284 R. C. Simpson, E. R. Shanahan, R. A. Scolyer and G. V. Long, *Nat. Rev. Clin. Oncol.*, 2023, **20**, 697–715.
285 A. Nath, R. Bhattacharjee, A. Nandi, A. Sinha, S. Kar, N. Manoharan, S. Mitra, A. Mojumdar, P. K. Panda and S. Patro, *Biomed. Pharmacother.*, 2022, **151**, 113122.
286 D. Boeckaerts, M. Stock, C. Ferriol-González, J. Oteo-Iglesias, R. Sanjuán, P. Domingo-Calap, B. De Baets and Y. Briers, *Nat. Commun.*, 2024, **15**, 4355.
287 M. Keith, A. Park de la Torriente, A. Chalka, A. Vallejo-Trujillo, S. P. McAteer, G. K. Paterson, A. S. Low and D. L. Gally, *Proc. Natl. Acad. Sci. U. S. A.*, 2024, **121**, e2313574121.
288 S. Djebara, R. Lavigne and J.-P. Pirnay, *Lancet*, 2025, **405**, 1901–1903.
289 O. Alkhamis, J. Canoura, P. T. Ly and Y. Xiao, *Acc. Chem. Res.*, 2023, **56**, 1731–1743.
290 M. C. DeRosa, A. Lin, P. Mallikaratchy, E. M. McConnell, M. McKeague, R. Patel and S. Shigdar, *Nat. Rev. Methods Primers*, 2023, **3**, 54.
291 K. Wen, X. Meng, K. Lara and Q. Lin, *Talanta*, 2024, **275**, 126103.